Study of Advanced Photocathodes for Highly Polarized Electron Source

Thesis · March 2017

1 author:

Wei Liu
Brookhaven National Laboratory

中国科学院大学
University of Chinese Academy of Sciences

Study of Advanced Photocathodes for Highly Polarized Electron Source

By

Wei Liu

A Dissertation Submitted to

University of Chinese Academy of Sciences

In partial fulfillment of the requirement

For the degree of doctor of

Nuclear Technology and Applications

Institute of Modern Physics, Chinese Academy of Sciences

April, 2017

Study of Advanced Photocathodes for Highly Polarized Electron source

Wei Liu (Nuclear Technology and Application)

Directed by:
Dr. Hongwei Zhao, Dr. Huanyu Zhao (IMP)
Dr. Shukui Zhang, Dr. Matthew Poelker (JLab)

Abstract

GaAs-based photocathodes have been widely used in the photogun to produce spin polarized electron beams. These photocathodes in the photogun are required to provide high quantum efficiency (QE), high degree of electron-spin polarization (ESP) and long lifetime to satisfy demanding requirements of today's electron accelerators. Photocathodes that demonstrate improved performance will enable the successful construction of proposed new accelerators that will enable new physics research. This thesis presents several studies of polarization photocathodes aimed to quantifying and further understanding the limitation of today's GaAs-based photocathodes, and then successfully identifies effective methods to improve their performance to meet the requirements of the state-of-the-art and future advanced electron accelerators.

Up to now, the strained superlattice GaAs-based photocathodes is the only material that provide electron beam with high ESP (~90%) for electron accelerators, but its primary drawback is that the QE is low (~1%). These photocathodes have already been successfully used in electron accelerators (such as CEBAF at JLab), but the low QE is very hard to satisfy the urgent demands of some new proposed electron accelerators (such as eRHIC requires the beam current up to 50 mA). Thus, it is extremely urgent to improve greatly the QE of these polarization photocathodes. This thesis reports a high-polarization strained GaAs/GaAsP superlattice photocathode fabricated with Distributed Bragg Reflector (DBR) structure, which successful achieved a breakthrough in the QE (~6%) that is improved several times over the existing QE (~1.2%), while still maintaining high ESP, through stringent parameter design and repeated experimental optimization. This provides important benchmark parameter for several proposed electron accelerators and will significantly shorten the development process for producing mA order of magnitude of electron beam with high polarization.

The photocathode lifetime is one of the main factors of modern DC high voltage photogun, and long lifetime provides a necessary condition for photogun to provide a sustained and stable electron beam. Although it has been realized that the lifetime of photocathodes is primarily limited by ion back-bombardment, until now, no systematic studies of the effects of ion back-bombardment on photocathodes have been performed, of which many physical mechanisms are unclear. In this thesis, the sensitivity of QE decay (or lifetime) to ion back-bombardment is studied and evaluated in detail for the first time, giving the important conclusion that the best choice for a photogun using GaAs-based photocathodes would be surface cleave plane (110). This study provides an important theory for

photogun researchers to understand the ion back-bombardment and helps to prolong the operating lifetime of photogun in future.

The ESP obtained from typical bulk unstrained GaAs photocathodes is usually considerably less than the theoretical maximum value of 50% because of depolarization (or spin relaxation) mechanisms that originate within the photocathode material and at the vacuum surface interface (i.e. activation layer). This thesis provides a comprehensive review of depolarization mechanisms and presents a systematic experimental evaluation of polarization sensitivities to temperature, dopant density, activation layer and crystal orientation. One of the key findings is that the bulk unstrained GaAs photocathode can provide the highest polarization ~50%, consistent with the maximum theoretical value, when the photocathode sample had relatively low dopant concentration and was cooled to 77 K. This study helps to better understand the mechanisms of polarization loss of electrons in the GaAs photocathode, and benefits to produce electron beam with higher ESP from GaAs photocathode.

A novel strained superlattice structure, GaAsSb/AlGaAs photocathode, is also proposed and studied in this thesis, and some experiments for it have been performed. Although the experimental results are not as good as our expectation, it provides a strong research foundation for future development of high polarization photocathodes.

Finally, a brief summary of the work under preparation for generation of mA record-level high-current polarized electron beam from the Upgraded Injector Test Facility (UITF) at JLab is presented.

Key words: GaAs photocathode, high polarization photocathode, strained superlattice, Distributed Bragg Reflector, ion bombardment, spin relaxation mechanism

Contents

Chapter 1 Introduction

Electron accelerators always play a critical role in the nuclear and high energy physics research, since they have been developed at the beginning of the last century [1]. Electron accelerators are widely used in large scientific facilities, like the electron-positron collider (EPC), electron-ion collider and Free electron laser (FEL). Recently, higher quality electron accelerators are demanded by many proposed accelerator facilities, such as JLab electron-Ion collider (JLEIC) [2], electron Relativistic Heavy Ion Collider (eRHIC) [3], EIC facility in China (EicC) [4] and international Linear collider (ILC) [5].

As the core component of electron accelerator, electron source is responsible for providing high quality electron beam. According to the process of electron generation, electron source can be divided to three main types: thermionic emission source, field emission source and photoemission source (or photocathode). The traditional thermionic and field emission source technologies have been relatively mature, but they cannot meet the requirements of some electron accelerators in terms of the beam emittance and ultrashort pulse beam. [6] The photoemission source can be excited by ultrafast pulse laser and emit ultrashort pulse beam with repetition frequency up to GHz on the premise of maintaining high duty ratio. [7] Moreover, the electron beam structure can be easily controlled by controlling the time and space structure of the driven laser. In addition, GaAs-based photocathodes can produce spin-polarized electrons, which provides a powerful means for many experiment researches and is also a research hotspot in the field of today's electron accelerator. [8]

Spin-polarized electron is an important means to detect the properties of mater, which can help to obtain many unique physical information, such as the nuclear structure, the dynamics of strong interactions, electro-weak nuclear physics, parity-violation, and physics beyond the standard model. [9] Spin-polarized electron can also be used in the field of asymmetric chiral molecules [10] and the study of spin-orbit coupling [11]. The exploration of polarized electron source began in the 1970s, and the early methods of generating polarized electron, such as Fano effect of rubidium atom [12], photoionization of 6Li atom [13] and chemical ionization of metastable helium atom [14], were not successfully developed to be polarized electron source for accelerators because of their own drawbacks. In 1975, the ETH Zurich reported the use of GaAs photocathode to generate polarized electron beam with advantage of high current, low energy dispersion and high brightness. [15] Subsequently, GaAs-based photocathodes were successfully applied in many accelerator facilities for high-energy and nuclear physics research, including SLAC [16], Mainz Microtron [17], BATES laboratory [18], NIKHEF [19], Bonn university [20] and CEBAF [21].

With the development of electron accelerator, the polarized electron source with better performance is required to provide higher quality electron beam. Three common parameters used to measure the properties of photoemission source are quantum efficiency (QE), spin polarization and operating

lifetime. In which, high QE is the key factor to provide high current beam, high polarization (>80%) is the prerequisite to ensure the accuracy of physical experiments, and long operating lifetime is the basis condition to provide a stable and continuous beam. The most common photocathodes, used to generating high polarization electron beam, are GaAs-based strained superlattice (SSL) materials, which can produce a maximum polarization of 92% and can meet the requirements of modern electron accelerators. However, the QE of these photocathodes in experiments is only ~1%, and the corresponding average beam intensity is basically below milliamps, which cannot satisfy the demands of some proposed accelerator facilities. For example, the eRHIC requires a polarized electron beam of up to 50 mA. A laser with power of up to 8 W (780 nm of wavelength) is needed to drive a photocathode to produce such high current beam if the QE of the photocathode is ~1%, which is beyond the power range of this type laser commonly used in modern accelerators. Moreover, due to the low QE, most of the incident light converts into heat energy inside the cathode and heats the cathode material, which accelerates the attenuation of the QE. If the laser power is increased, the cooling system for photocathode will have to be used, which make the problem more complicated. It is very difficult to setup the cooling system in the photogun with high voltage (100 kV – 300 kV), so it is urgent to increase the QE of photocathode. Increasing QE benefits to obtain high current electron beam and reduces the laser power required for producing the electron beam of same current intensity, which simplifies the laser system and cooling system for the photogun, helps to prolong the operating lifetime of photogun, and ultimately is beneficial to the production of high-quality polarized electron beam and the maintenance of stable operation of the accelerator facilities. Therefore, how to increase the QE on the premise of high degree of polarization is a key problem to be solved.

The fundamental reason for the limitation to increase QE of the SSL photocathode is that its working region (SSL region) is very thin, which greatly reduces the absorption of incident light. Limited by the degeneracy of light and heavy hole bands, typical bulk GaAs can only produce polarized electrons with theoretical limit of 50%. The strain generated by GaAs growing on crystals with different lattice constant can eliminate the degeneracy of light and heavy hole bands, thus obtaining polarized electrons with polarization of 100%. In the strained structure, the energy generated by the strain will accumulate as the thickness of the film increases and release in the form of defects, reducing the material's ability to eliminate degeneracy and leading to a decrease in polarization. Therefore, in the SSL, it is necessary to ensure that each periodic layer is thin enough to maintain the strained level of the material, thus ensuring that the photocathode has a high enough polarization. At present, the mature superlattice structure is generally 20-30 cycles, with a total thickness of 100-200 nm. Therefore, the methods to improve the QE of the SSL photocathodes can be started from two aspects: 1) further increase the thickness of the superlattice region; 2) enhance the absorption of incident light in the superlattice region. Recently, the university of Nagoya in Japan has developed a 90-cycle GaAs/GaAsP SSL structure with a total thickness of 700 nm through the strain compensation method. However, its

QE does not increase with the thickness linearly, and its maximum QE is 1.6%. The second method is to add Distributed Bragg Reflector (DBR) structure into the photocathode to improve the absorption of the SSL structure to incident light and reach the purpose of improving the QE of photocathode, which is also one of the research topics of this thesis.

As mentioned above, long operating lifetime is the basis condition for the photogun to provide a stable and continuous beam. How to prolong the operating lifetime of polarization photocathode gun has been a worldwide problem. In recent decades, photogun researchers have prolonged the operating lifetime by increasing the vacuum in the chamber, increasing the operating voltage and developing special photogun structure (such as "reverse" cone insulator structure). For example, through the continuously upgrading and updating the photogun in the past 20 years, CEBAF has its fifth generation photogun, which can produce the charge lifetime up to 200 C. The primary mechanism that affects the operating lifetime of modern DC high voltage photogun is ion back-bombardment effect [22,23]. At present, photogun researchers reduce the effect of ion back-bombardment on the operating lifetime by improving the vacuum and operating voltage of the photogun. However, up to now, no systematic studies have been carried out on the effect of ion back-bombardment on photocathodes, of which many physical mechanisms are still unclear. Therefore, systematic studies on ion back-bombardment effect are imperative.

The CEBAF at JLab uses GaAs-based photocathodes to produce electron beams, in which electrons are accelerated to 12 GeV for high-energy nuclear physics experiments that explore the fundamental properties of matter. In order to meet the requirements of different physical experiments in CEBAF, the photocathode in the photogun needs to provide high current, high polarization and high stability (or long lifetime) electron beam. The Center for Injectors and Sources (CIS) at JLab is responsible for producing such high-quality electron beam. Over the years, a series of researches to improve the performance of electron source have been ongoing in CIS.

In this thesis, methods for improving the lifetime, QE and spin polarization of photocathodes in the photogun will be presented. The main research contents and objectives are as follows:

1. By adding a distributed Bragg reflector (DBR) structure into the photocathode, a Fabry-Perot resonance cavity is formed by the vacuum/photocathode interface and the DBR structure. Laser is basically single transmission and absorption in the traditional photocathode, while the laser is reflected back and forth in the photocathode with the Fabry-Perot resonance cavity, and multiple absorption occurs, that is optical absorption enhancement, resulting in the increase of QE. DBR photocathode technology was proposed to enhance the QE of photocathode as early as 1993 [24]. However, before the work of this thesis, the technology has not succeeded in significantly improving the QE of GaAs-based SSL photocathodes. In the previous research work [25], the highest QE obtained from the SSL photocathode with DBR structure is 1.2%, which is not substantially different from the QE of

photocathode without DBR structure. In this thesis, a DBR photocathode with higher performance will be presented, which obtained by optimizing the design and preparation process and repeated experimental tests.

2. The photocathode lifetime is affected by many factors, in which the ion back-bombardment is the primary mechanism limiting the lifetime of modern DC high voltage photogun. The residual gas between cathode and anode in photogun is easy to be ionized into positive ions by electron beam. Under the action of negative bias voltage on the cathode, the positive ions are accelerated and then reach to the cathode surface with certain energy. This process is called ion back-bombardment. These ions will destroy the activation layer (Cs/O or Cs/NF3 layer) on the photocathode surface, thus destroying the negative electron affinity (NEA) that dominate the photocathode QE. Then, these ions will implant into the photocathode and stay between the atoms, forming interstitial defects that reduce the electron diffusion length. In addition, high-energy ions will knock out atoms from the crystal structure, resulting in altering the energy band structure of the crystal. All these possibilities would lead to the same result: a decrease in QE, which means a decrease in the lifetime of photogun. This thesis will explore the sensitivity of GaAs photocathodes on different cleave plane to the back-bombardment effect of ions with different energy (100eV and 10,000ev), and evaluate whether the ion channeling can reduce the effect of ion back-bombardment on photocathode, thus prolonging the operating lifetime of photogun.

3. Most experiments on CEBAF require polarized electron beam. GaAs is a good choice to be as the polarization photocathode, which can produce polarized electrons illuminated by circularly polarized light. Due to the depolarization process of electrons within the photocathode and activation layer, the polarization of electrons generated by the non-strained GaAs photocathode is usually less than the theoretical limit of 50%. In this thesis, we will comprehensively overview the depolarization mechanism in photocathodes, and evaluate the dependence of polarization on cathode temperature, doping concentration, activation layer thickness and crystal orientation by systematic experiments. Finally, we obtain polarized electrons with polarization up to the theoretical limit of 50% in experiments.

4. As mentioned above, the maximum polarization of electrons produced by SSL photocathode to date is 92%, but photocathode researchers have never given up on higher goals. During the development of SSL photocathodes over the past 20 years, many GaAs-based SSL photocathodes have been proposed in order to improve the performance polarized photocathodes. So far, the SSL structures reported in the literatures are: AlGaAs/GaAs [26], InGaAs/GaAs [27], GaAs/GaAsP [28], AlInGaAs/GaAsP [29], InGaAs/AlGaAs [30] and AlInGaAs/AlGaAs [31]. In this Thesis, a novel SSL structure, GaAsSb/AlGaAs, will be explored aimed to obtain better performance.

This thesis consists of five chapters, which are arranged as follows:

Chapter 2: Firstly, the characteristics of various common electron sources are reviewed, especially the characteristics, development and current situation of photoemission source (photocathode) used in

electron accelerators. Then, the characteristics of GaAs material, including crystal structure and band structure, are introduced. Thirdly, the formation principle of NEA on the photocathode surface and the theoretical model of three-step emission are introduced. Finally, the principle of producing polarized electrons from GaAs-based photocathodes, the depolarization process in photocathodes and the principle of measuring polarized electrons are discussed.

Chapter 3: The researches on GaAs photocathode are described. Firstly, the experimental equipment and techniques used in this thesis are introduced, including the ultra-high vacuum (UHV) system, photocathode activation methods and photocathode polarization measurement. Then, the studies on ion back-bombardment effect are introduced. Finally, the research about polarization dependence of GaAs are presented.

Chapter 4: The exploration of high polarization photocathode is discussed. Two GaAs-based SSL photocathodes are presented: GaAs/GaAsP SSL photocathode with DBR structure and GaAsSb/AlGaAs SSL photocathodes. Finally, a brief introduction of the preparation work for generating high-energy high-current polarized electron beam using the Upgraded Injector Test Facility (UITF) at JLab is presented.

Chapter 5: The author summarizes the research results and gives the suggestion for the future development of high-current and high-polarization photocathode.

Chapter 2 Electron source and GaAs photocathodes

2.1 Electron source

Electron source is a critical component of the modern accelerators and determines the ultimate achievable performance of the machine. There are three processes to be used to generate electrons: thermionic emission, field emission, and photoemission. This section will review the three type electron sources based on these processes.

2.1.1 Thermionic emission source

Thermionic emission source has been widely used in electron accelerators for the past decades and remains in use at many laboratories. [32,33,34,35,36]

Heating thermionic cathode will increase the energy of electrons in the cathode. When the cathode was heated to a critical temperature, electrons in the cathode can obtain enough energy (bigger than the vacuum energy level, E_∞) to overcome the work function ϕ (the difference between Fermi energy level and vacuum energy level) and emit into the vacuum, which is so called thermionic emission (TE, as known as thermionic electron emission and the Edison effect).

Figure 2-1 shows the process of thermionic emission. Electrons stayed down the Fermi energy level (E_F) at room temperature obtain energy while heating cathode then transport to the surface and emit into vacuum.

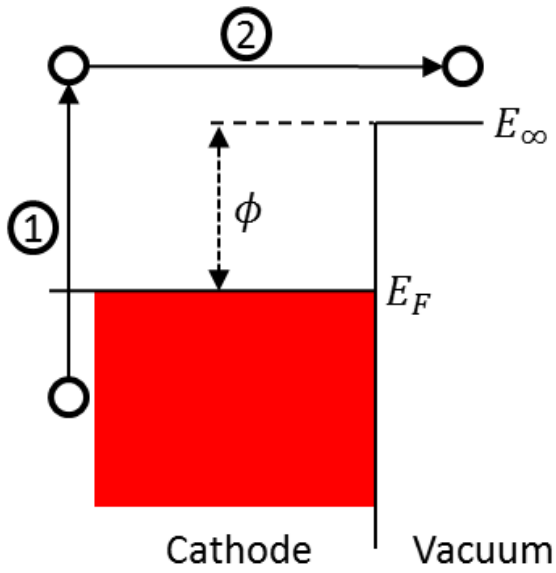

Figure 2-1: The process of thermionic emission: electrons obtained energy while heating cathode and then emitted into vacuum

Figure 2-2 shows a schematic diagram of thermionic emission electron source. [36] In thermionic emission electron source, electrons emitted from a heated cathode with a low energy, then focused and accelerated by the electric field of anode. The emission current density from a heated cathode is given by the Richardson-Dushman equation: [37]

$$J_{TE} = A_G T^2 e^{-\frac{\phi}{kT}} \qquad 2\text{-}1$$

where J_{TE} is the thermionic emission current density ($A \cdot mm^{-2}$). T is the temperature of cathode (K), ϕ is the work function (eV), k is the Boltzmann constant, and A_G is the Dushman's constant that is written by: $A_G = \lambda_R A_0$. In which λ_R is a material-specific correction factor that is typically of order 0.5, and A_0 is a universal constant given by $A_0 = \frac{4\pi m k^2 e}{h^3} = 1.20173 \times 10^6 A \cdot m^{-2} \cdot K^{-2}$. From this equation, one can see that the emission current depends on both the temperature and the size of emission area of the cathode. A high temperature and large emission area help to produce a high emission current. However, there is a saturated current emitted from a heated cathode. When the temperature of cathode goes up to a very high value, the current saturates. This temperature is usually used as the operating temperature to keep the cathode has a good lifetime (higher temperature reduces the lifetime of cathode).

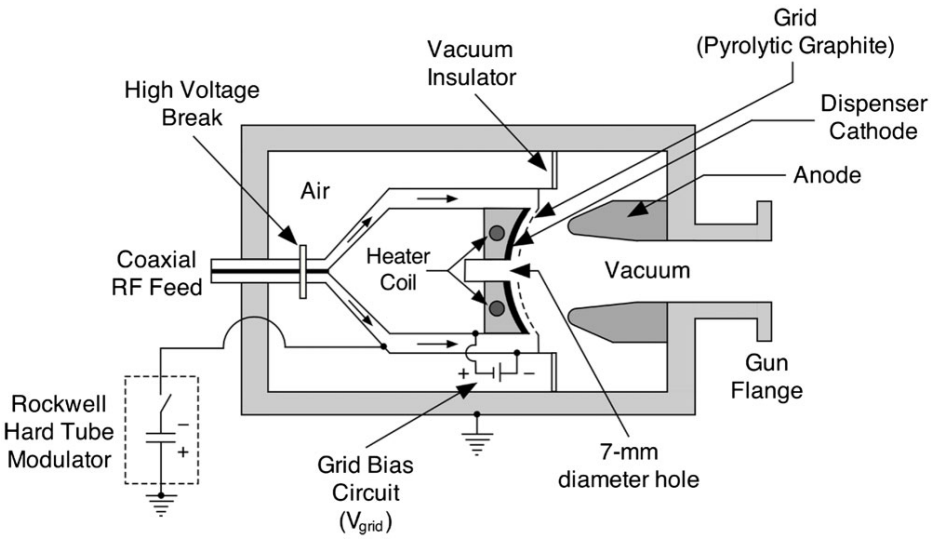

Figure 2-2: Schematic diagram of thermionic emission electron source

The commonly-used cathode materials for thermionic emission sources are LaB6 and dispenser cathodes (a tungsten mixed with other materials, such as Cs, to lower its work function). LaB6, possessed work function of 2.4 eV, can provide the highest current density of 200A $\cdot cm^{-2}$ at a typical operating temperature of 1600 °C. The W (dispenser cathode), possessed work function of 4.5 eV, can provide the highest current density of 140 A $\cdot cm^{-2}$ at a typical operating temperature of 950 °C. Although they can provide so high current density, but the typical current density in experiment provided by them ranges from 10 to 30 A $\cdot cm^{-2}$. [38] It is noted that a single-crystal CeB6 was also

used as thermionic cathode, because of the CeB6 own a high resistance against contamination, uniform emission density, smooth surface, and high emission current density (~50 $A \cdot cm^{-2}$).[34]

Thermionic emission source is a simple and robust electron source (gun). It requires more simple work condition than other type electron sources. Such as, it avoids using the complex and sensitive driven laser used in photoemission source, it works at lower vacuum (for thermionic emission source: $\sim 10^{-7}\ Torr$, for photoemission source: $\sim 10^{-11}\ Torr$) and can provide higher current than photoemission source. Besides, thermionic emission source not only operate at CW mode, but also operate at RF mode. [35] However, the main problem for a thermionic source is that electrons are continuously emitted throughout the accelerating phase of the RF mode. It is difficult to produce the short bunch length current beam with flexible bunch/macro bunch structure required for several modern accelerators.

2.1.2 Field emission source

Under the influence of a strong electric field, electrons in cathode have a probability to tunnel through the surface potential barrier into vacuum, which is so called field emission (FE, also known as field electron emission and electron field emission). The difference to thermionic emission is that electrons emit into vacuum by tunnel effect for field emission, but electrons need obtain enough energy to overcome work function then emit into vacuum for thermionic emission. Under the influence of a strong electric field, the surface potential barrier of a material will change, called Schottky effect. The changed surface potential barrier is deformed along the line AB shown in

Figure 2-3. Stronger electric field leads to bigger slope of the line AB, causing to shorter tunnel distance (d), therefore the probability of electrons tunnel through the surface potential barrier into vacuum is higher (i.e., higher electron current beam can be achieved). [39] Electrons with higher energy pass through shorter tunnel distance, leading to higher emission probability. So heating cathode can help to improve the emission probability for field emission. In addition, applying the sharp point as the emission area also contributes to improve the emission probability for field emission.

The current density for field emission is given by Fowler-Nordheim equation: [40]

$$J_{FE} = aE^2 exp(-\frac{B\phi^{3/2}}{E}) \qquad 2\text{-}2$$

where J_{FE} is the field emission current density, a is a function of ϕ ($a = 3.5 \times 10^{-5}\ A \cdot V^{-2}$ for tungstem with $\phi = 4.5\ eV$), E is the electric field at the emission area ($\mathrm{V \cdot cm^{-1}}$), B is a constant (6.12×10^8), ϕ is the work function of the cathode material (eV). From Eq. (2-2), one can see that the field emission current density depends on the cathode material, the size of emission area and the electric field. The commonly-used cathode material for field emission source is tungsten (mixed with ZrO_2 to lower its work function).[40] Admittedly, some other materials are also used as field emission cathode, such as the carbon nanotube (CNT) [39,41] and ZrC [42,43].

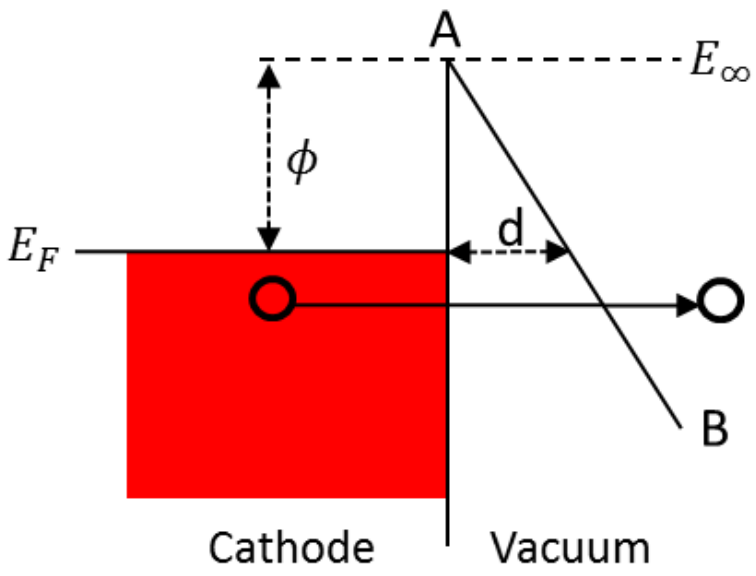

Figure 2-3: The process of field emission: electrons tunnel through the surface potential barrier changed under the influence of a strong electric field into vacuum.

Field emission source, same to thermionic emission source, is also a simple and robust electron source (gun) and requires a simple work condition. It can work at room temperature, lower than the temperature for thermionic emission source, and avoid using complex and sensitive driven laser required for photoemission source. The vacuum pressure for field emission source work is usually $\sim 10^{-10}$ Torr. It is noted that using a low power femtosecond laser illuminate the cathode can also produce field emission, called optical field emission. 44 In optical field emission, the laser field instantaneously wiggles the surface potential barrier. If the barrier is sufficiently thin, electrons tunnel into vacuum. The main characteristics of field emission source are the small size of emission area, high current density, high brightness, low energy spread and long operating lifetime. The characteristics of the field emission source compared with two thermionic emission sources are shown in Table 2-1. [45] One can see that these characteristics of the field emission source listed in Table 2-1 are superior to that of two thermionic emission sources. However, the small size of emission area also leads to small size of current beam, high divergence and therefore high loss of current beam. To overcome this issue, field emitter arrays (FEAs) [42,43] were developed which can effectively enlarge the size of current beam, lower the divergence and thus reduce the loss of current beam. Finally, it is also difficult for field emission source to produce the short bunch length current beam with flexible bunch/macro bunch structure required for several modern accelerators.

Table 2-1: Characteristics of the field emission source compared with two thermionic emission sources

	Units	Tungsten	LaB_6	Field Emission
Work function, ϕ	eV	4.5	2.4	4.5
Richardson's constant	A/m2K2	6×10^5	4×10^5	
Operating temperature	K	2700	1700	300
Current density	A/m2	5×10^4	10^6	10^{10}
Crossover size	μm	50	10	<0.01
Brightness	A/m2sr	10^9	5×10^{10}	10^{13}
Energy spread	eV	3	1.5	0.3
Emission current stability	%/hr	<1	<1	5
Vacuum	Pa	10^{-2}	10^{-4}	10^{-8}
Lifetime	hr	100	500	>1000

2.1.3 Photoemission source

The photoemission source (photocathode) was developed based on the quantum theory of photoemission (or photoelectric effect) given by Einstein in 1903. [46] According to the phase of cathode materials, photocathodes can be divided into three types: solid, liquid, gas phase photocathodes, and the process of photoemission for three type photocathodes are different. [47] For gas phase, when the incident photon has energy larger than the ionization potential I_P of the molecule, it can give a free electron. The photoemission process for solid and liquid photocathodes both can be given by Spicer's Three-Step Model: the absorption of photons by a photocathode, the transmission of the electrons from inside of photocathode to the photocathode-vacuum interface, and the emission of electrons into the vacuum. Photocathodes used in accelerators are almost solid materials, [48] so only solid photocathode will be discussed here.

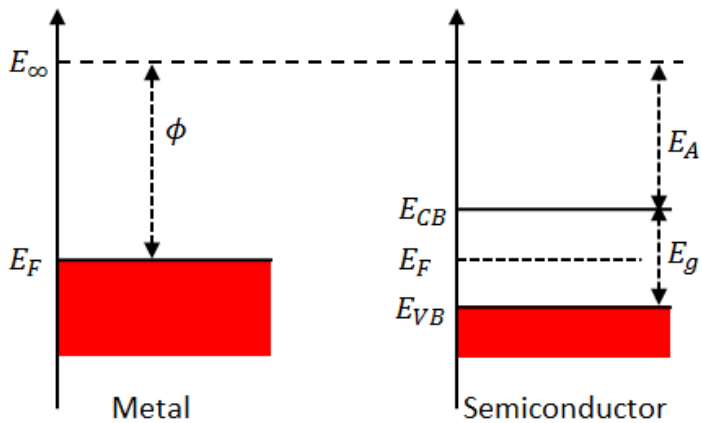

Figure 2-4: Energy band structures of metal and semiconductor. Also, definition of the Fermi energy level E_F, the work function ϕ, the energy band gap E_g and the electron affinity E_A.

The energy band structures of metal and semiconductor are different, shown in

Figure 2-4. [47] Metals are characterized by the absence of a forbidden energy gap. Electrons in conduction band of metals, filled up to Fermi energy level E_F, only need overcome the work function ϕ of metals to emit into vacuum, i.e., the threshold energy for photoemission E_{th} of metals is equal to the work function ϕ of metals ($E_{th} = \phi$). In semiconductor the valence band is separated from the conduction band by forbidden energy gap, the Fermi energy level lies between the valence band and the conduction band. Electrons in semiconductors are almost filled in valence band. Even at high temperature, the occupancy of the conduction band is much too low to induce an appreciable photoemission. Thus electrons firstly jump from valence band to conduction by absorption of photon energy then overcome the electron affinity E_A (the energy difference between the bottom of the conduction band and the vacuum energy level) to emit into vacuum, i.e., the threshold energy for photoemission E_{th} of semiconductors is equal to energy band gap E_g plus the electron affinity E_A ($E_{th} = E_g + E_A$).

In the first step of Three-Step Model, the absorption of photons, a large number of quasi-free electrons exist in metals, which have low probability to absorb photons, leading to the optical absorption is usually low (the optical reflectivity is usually high of order of 80% for metals). This is a first reason why metals have low QE. In the second step, the transmission of electrons, excited electrons loss overriding energy by scattering with quasi-free electrons in conduction band, leaving electrons with low energy reached on the surface. Due to metals have a high work function, these low energy electrons couldn't overcome surface potential barrier and be emitted into vacuum, i.e., the third step, emission of electrons, will not happen. The escape length - represented the maximum length that excited electrons can diffuse before losing their excess energy - is of the order of a few atomic layers. It means that only these photoelectrons created within a few atomic layers to the surface can keep their excess energy and be emitted into vacuum. This is a second reason why metals have low QE.

Conversely, semiconductors possess generally low optical reflectivity and can efficiently absorb the incident light. In the transmission of electrons, the dominant process is lattice-scattering which leads to much smaller energy loss per interaction, thus the escape length can reach to several ten nanometers. For these materials whose absorption length is shorter than this escape length, photoelectrons reached on the surface still have excess energy to overcome surface potential barrier and be emitted into vacuum, so that they can be good photocathodes due to their high photoemission efficiency. In semitransparent photocathodes, there must be a compromise between maximizing the light absorption and maximizing the photoemission efficiency. However, opaque reflective photocathodes don't have this inconvenience and their thickness is only limited by the resistivity of the material. [47]

Many semiconductor photocathodes (III-V semiconductor) possess the ability to achieve negative electron affinity (NEA) surface that can help to more low energy electrons (even if these "hot" electrons in the bottom of conduction band) emit into vacuum. Doping in the semiconductors makes the band structure bending at the surface. The band bending is downwards with width of W_{BB} in p-type semiconductor, and it is upwards with width of W_{BB} in n-type semiconductor (shown in Figure 2-5). [46] The upwards band bending in n-type semiconductor increase the effective electron affinity of V_{BB}, which make electrons more difficult to emit into vacuum. However, the downwards band bending in p-type semiconductor give an inverse effect. What's more, the downwards band bending makes it possible to form NEA surface for some III-V semiconductors (such as GaAs, GaP) by applying alkali metals (usually Cs) and oxidant (oxygen (O) or fluorine (F)) layer on the surface (More details about NEA photocathodes will be discussed later in section 2.2.1). So, most photocathodes apply p-type materials.

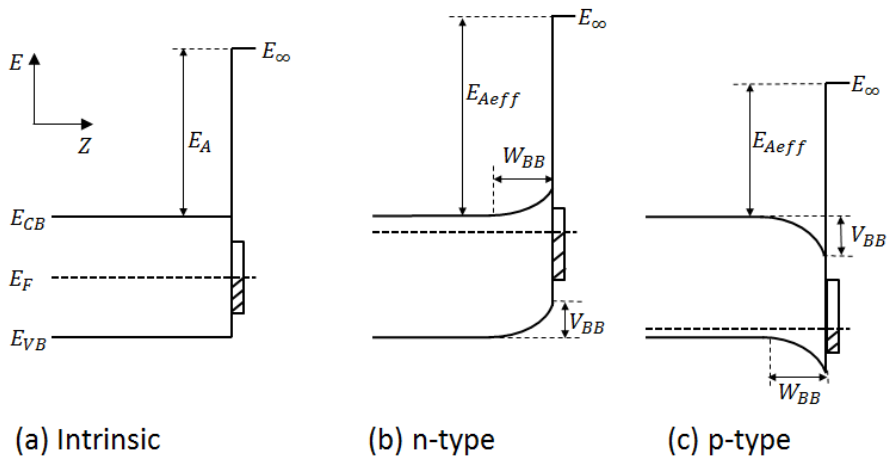

Figure 2-5: Energy band structure of three type semiconductors: (a) Intrinsic semiconductor, band isn't bent; (b) n-type semiconductor, band is bent upwards with width of $\boldsymbol{W_{BB}}$, so the vacuum energy level increase amount of $\boldsymbol{V_{BB}}$; (c) p-type semiconductor, band is bent downwards, so the vacuum energy level decrease.

The commonly-used photocathode materials are GaAs [49], Cs3Sb [50], CsK2Sb [49], Na2KSb [51], and Cu (or Ag) [52,53] which have been reported to generate average current of at least 52 mA, 20 mA, 65 mA, 65 mA, and <1 mA (or QE <1%), respectively. Compared with other two type electron sources, photoemission source needs more complex instrument-driven laser and high requirement for the vacuum pressure of chamber ($\sim 10^{-11}$ Torr). However, it's easier to control current beam structure by just controlling the driven laser structure. Such as, using pulse laser produces pulse electron current beam, and the frequency and width of pulse of laser can be easy to control. Thus, the photoemission source can produce the short bunch length current beam with flexible bunch/macro bunch structure.

2.2 Photocathode characteristics

Some critical characteristics of photocathodes should be analyzed and optimized when selecting photocathodes for electron sources in accelerators. Here, three main characteristics: quantum efficiency (QE), photocathode lifetime and electron-spin polarization (ESP) are summarized.

2.2.1 Quantum efficiency

Quantum efficiency (QE) is defined as the ratio of the number of electrons emitted from photocathodes to the number of incident photons. This definition of QE ignores nonlinear emission mechanisms, such as two-photon effects, which do not play a significant role even at the highest commonly-used photocathodes illumination levels of a few hundred watts per square centimeter. QE is a number ratio of electrons to photons and therefore is unitless. QE depends on photocathode material and driven laser wavelength. In practice, the actual QE achieved is a sensitive function of the cathode fabrication and preparation process (such as activation process).

A widely used relation to estimate QE is given by: [54]

$$QE = \frac{Ihc}{eP\lambda} \times 100\% \qquad 2\text{-}3$$

where I is the measured photocurrent (μA), h is the Plank's constant ($6.626 \times 10^{-34}\ J \cdot s$), c is the speed of light ($2.998 \times 10^{8}\ m \cdot s^{-1}$), e is the electron charge ($1.6 \times 10^{-19}\ C$), P is the driven laser power (mW), and λ is the driven laser wavelength (nm). Thus, the QE can be determined experimentally by measuring the incident laser power and the resulting photocurrent. To be convenient, the QE relation can be expressed as approximately:

$$QE = \frac{124 \cdot I(\mu A)}{P(mW) \cdot \lambda(nm)}\ (\%) \qquad 2\text{-}4$$

QE is an important factor for photocathodes. This value of it gives an indication of photocurrent which can be obtained from the photocathodes driven by a laser with given power and wavelength. A high QE helps to obtain high photocurrent that significant enhance the physics capabilities of electron accelerators.

2.2.2 Photocathode lifetime

Photocathode lifetime, indicates how long the QE lasts, is commonly defined as the time taken for the QE to fall to 1/e of its initial value, which strongly depends on the environmental and operating conditions. Long photocathode lifetime is beneficial to extract more stable electron current and need less interruption to replace or revive depleted photocathodes, which benefits accelerator operations. There are two types of photocathode lifetime often used which respond to different operational condition, called dark lifetime and operational lifetime. In actual, we use the operational lifetime to represent the photocathode lifetime, which also called lifetime or 1/e lifetime. The dark lifetime refers to the lifetime of a photocathode with no exposure to light or be illuminated at very low laser intensity. It depends mainly on the photocathode material, vacuum pressure, partial pressure of any contaminating gases and possible surface coating evaporation. Operational lifetime refers to the lifetime of a photocathode with extracting high current beam. It depends on not only these conditions affected dark lifetime, but also the ion back-bombardment, cathode heating and driven laser.

In the photo-gun, the operational lifetime is significantly shorter than the dark lifetime since several additional factors, such as high-power illumination and high electric field. The lifetime of a photocathode is strongly sensitive to the operating current. Generally, high operating current lead to short lifetime due to the required high-power driven laser will strong heat cathode leading to the surface-active layer (NEA surface) evaporated and therefore QE decreased. In addition, the ion back-bombardment is stronger at high operating current than that at low operating current which also decrease QE. The initial QE strongly affects the lifetime of photocathode. To get same current at higher QE less power of driven laser is need, so that less cathode heating occurs which means longer lifetime will be obtained. To estimate more effectively the operational lifetime, charge lifetime is often quoted. The charge lifetime is defined as the amount of charge that can be extracted from a photocathode before QE falls to 1/e of its initial value.

It is noted that the photocathodes can still run to provide current for accelerators after running it as long as their lifetime. It depends on the requirements for accelerators and the driven laser. For some photocathodes, such as GaAs, a reactivation process is commonly used to restore the QE for a dead photocathode, which can be pulled out from the chamber for the process and later re-insert while remaining the vacuum pressure.

2.2.3 Electron-spin polarization

Spin-polarized electrons are used to study nuclear structure, the dynamics of strong interaction, electro-weak, nuclear physics, including parity-violation, and physics beyond the standard Model. [55] Electrons with a net spin state are called spin-polarized electrons. Electron spin is an intrinsic property of electrons, which can be considered two states: spin-up (↑) and spin down (↓). The electron-spin polarization (ESP or simply written by P) for the spin-polarized electrons is defined as the net spin states to the total spin states, and given by:

$$P = \frac{N\uparrow - N\downarrow}{N\uparrow + N\downarrow} \qquad 2\text{-}5$$

where $N\uparrow$ is the number of electrons with spin-up state and $N\downarrow$ is the number of electrons with spin-down state.

The electron-spin polarization is an important factor for polarization photocathodes. Many accelerators, such as CEBAF, need photocathodes to provide high electron-spin polarization which can significantly enhance the physics capabilities of accelerators. The commonly-used polarization photocathodes are Ⅲ - Ⅴ semiconductor photocathodes, especially GaAs. The structure of photocathodes determines the electron-spin polarization.

2.3 The photocathode in accelerators

Different type of photocathodes exhibits different characteristics required by different accelerators. Thus, the type of photocathodes is a critical factor should be considered when selecting photocathodes

for electron sources in accelerators. In the section, three main types of photocathodes: metal photocathode, alkali antimonide photocathode and III-V semiconductor photocathode are introduced.

2.3.1 Metal photocathode

The commonly-used metal photocathode materials are Cu, Ag, Mg, Pb, Nb, Cr, Mo. [52,53] As mentioned before, there are two reasons why metal photocathodes exhibit low QE. The first reason is that metals possess very low absorption of light. To enhance the absorption of light, plasmon photocathodes were developed. The surface plasmons (SPs) represent an electron density wave on the metal-dielectric boundary [56] which can be treated as a monochromatic wave propagating along the metal-dielectric interface [57]. The surface plasmons have a longer wave vector (k_{sp}) than light waves of the same energy propagating along the surface, thus there needs a special light-plasmon coupler to increase the incident light wave vector (k_x) to match the surface plasmon wave vector, in order to "transform" the photons into SPs to induce resonance absorption of light by surface plasmons. [56] Experiments have proved that when a light illuminate a metal with special surface (grating, nanoparticle, nanohole) at a special incident angle, the absorption of light by the metal will be largely enhanced. [58,59,60,61]

If light ($k = \omega/c$) incident a grating with a grating constant a at an angle θ_0, its component in the surface can have wave vectors $k_x = (\omega/c)sin\theta_0 \pm \nu g$. The dispersion relation for resonance absorption of light by surface plasmons is given by: [56]

$$k_x = \frac{\omega}{c} sin\theta_0 \pm \nu g = \frac{\omega}{c}\sqrt{\frac{\varepsilon}{\varepsilon+1}} = k_{sp} \qquad 2\text{-}6$$

here, ν is an integer, $g = 2\pi/a$, and ε is the real part of dielectric constant of metal ($\varepsilon < -1$). To agree with this equation, the value of grating constant should be choosing carefully, which depends on the dielectric constant. And the dielectric constant depends on the metal material and the wavelength of incident light. For the commonly-used metal photocathode, the grating constant is usually set at order of tens of nanometers responding to the visible light used in most experiments. [58, 59]

A reasonable special surface structure helps to enhance the absorption of light by metal photocathode, which can offset the disadvantage of low absorption of light by metal photocathode. A metal photocathode has been found to reduce the reflectivity to below 1% by use of a subwavelength nanostructure. [59]

The second reason why metal photocathodes exhibit low QE is that electrons on the surface have low escape probability into vacuum due to electrons loss their excess energy during transmission to the surface and metals have high work function. To increase the escape probability, a way to decrease metal's work function has been demonstrated by applying a very thin layer of insulator on the metal surface. The traditional way to decrease the work function of metals was applying Cs/Cs_2O on the metals surface. [62] Recently, more insulators are used to be coated on the metal surface to increase

their QE. Such as, after depositing thin film of KBr and CsBr on Cu, the QE increase by factors of 26 and 77 for KBr/Cu and CsBr/Cu photocathodes, respectively. [63] The QE of Cu is also increased dramatically by coating a CsI film on the surface. [64] The QE of Ag is also found to be markedly enhanced by deposition of a few monolayers of epitaxial MgO on the surface, and the QE of MgO/Ag is a factor of 7 greater than that of clean Ag. [65]

2.3.2 Alkali Antimonide photocathode

Alkali antimonide is a type of compound semiconductor formed by elements of alkali metals and antimony, which has been used as photocathode at the beginning of the development of photocathodes. [47] The alkali antimonide photocathode exhibits high QE in the visible light region and their typical maximum QE is above 10%. [66] The alkali antimonide materials that can be used as photocathodes are Na_3Sb, Rb_3Sb, Cs_3Sb, K_3Sb, CsK_2Sb, Na_2KSb. [67,68] The first four materials are called mono-alkali antimonides, and the last two materials are called multi-alkali antimonides. Cs_3Sb and multi-alkali antimonides exhibit higher QE than others (almost above 10%), and their threshold energy for photoemission is in visible light region ($E_{th} = E_g + E_A \sim 2\text{eV}$), [67] therefore they are commonly used as photocathodes in accelerators.

Cs_3Sb photocathode possesses the highest QE among all the mono-alkali antimonides, and lowest threshold energy for photoemission ($E_{th} = 2.05\text{eV}$). [67] It also exhibits low dark current, fast respond time in the picosecond rage, tolerance of vacuum contaminants below 10-6 Torr, reasonable lifetime, easier of fabrication than multi-alkali antimonides, [69] thus it is the best choice to be as photocathodes in accelerators among the mono-alkali antimonides. The Cs_3Sb photocathodes have been successfully fabricated in CERN and BNL. [70,71]

Multi-alkali antimonides (CsK_2Sb, Na_2KSb) possess a higher QE and lower threshold energy for photoemission ($E_{th} < 2.05\text{eV}$) than mono-alkali antimonides. [67,72] The main advantage of multi-alkali antimonide photocathodes is the long lifetime or high achievable charge. A CsK_2Sb phtocathode developed in Hiroshima university exhibits a 1/e lifetime more than 3000 hours without beam emission and a 1/e lifetime regarding to amount of charge more than 300 C with beam emission. [73] In Cornell University, a successive continuous run with a current of 65 mA for Na_2KSb photocathode exhibits a 1/e lifetime of 66 hours [51], and a successive continuous run with a current of 60 mA for CsK_2Sb photocathodes exhibits a 1/e lifetime of 30 hours [47]. Under single-point illuminance, the total charge can be obtained from these photocathodes more than 2000 C. Compared with mono-alkali antimonide photocathodes, the biggest disadvantage for multi-alkali antimonide photocathodes is the hardness of fabrication. It is difficult to precisely control the fraction of each element during fabrication.

The electron affinity of alkali antimonide photocathodes is positive, so called positive electron affinity (PEA), which prevents electron escape into vacuum. [72] However, their energy band gap is small, and the EA also can be decreased by applying Cs_2O on the photocathode surface, [74] as a result the threshold energy for photoemission is not big and responds in the visible light region. It is noted that there is another alkali compound photocathode Cs_2Te whose properties are like that of alkali antimonides. Cs_2Te photocathode possesses high QE of typical value above 10%, and best value to 18%. [75] The Cs_2Te photocathodes developed at FLASH exhibit QE between 10% and 20% with a total charge of typically 2 C. [76] The Cs_2Te photocathodes developed at HZDR exhibit QE between 8% and 15% with lifetime for months, for example, a sample has fresh QE of 8.5% and provides beam time more than 2100 hours with total charge more than 264 C. [77]

2.3.3 Ⅲ-Ⅴ semiconductor photocathode

The Ⅲ-Ⅴ semiconductor photocathodes with direct-bandgap are good electron sources in accelerator because of their high photon absorption rate, long diffusion length, and their ability to achieve negative-electron affinity (NEA) surface, such as GaN, GaAs, InAsP. [78,79,80] The commonly-used Ⅲ-Ⅴ semiconductor photocathode is GaAs due to it has a large direct bandgap that respond in the visible light region. GaAs photocathodes have high photon absorption that helps GaAs to provide high QE. Its reflectivity coefficient ranges from 0.3 – 0.45, which depends on the wavelength of incident light. The NEA surface formed by applying Cs/Cs_2O (or CsF) on the high doping p-type GaAs surface makes GaAs photocathodes have a very high electron escape probability. Therefore, GaAs can provide the highest QE in all the photocathodes. A typical bulk GaAs photocathode with NEA surface can provide a QE near 20% at 532 nm of the wavelength of incident light. [81]

GaAs photocathode can provide spin polarized electrons for accelerators, which is its biggest advantage over all the other photocathodes mentioned before. When GaAs illuminated by a circularly polarized light with a given wavelength, it can produce spin polarized electrons. The degree of spin polarization from bulk GaAs is limited to values below 50% due to the degeneracy between the heavy-hole and light-hole of the valence state. [82] Reducing the degeneracy between heavy-hole and light-hole allows higher spin polarization values than 50% and the strain formed by growing GaAs on a crystal structure with a different lattice constant can attain the goal. [83,84] However, the single-strain GaAs photocathode can only provide very low QE. [85] The strained superlattice GaAs photocathode which maintained the required degree of strain to produce high spin polarization and provide sufficient active layer thickness to obtain high QE was then developed to replace the single-strain photocathode and can provide high electron-spin polarization (ESP) up to 92% and high QE up to 1.6%. [28,31,86]

GaAs photocathodes exhibit high QE and high ESP, low dark current, fast respond time in picosecond range, and reasonable lifetime. They are widely used in accelerator facilities at many laboratories, such as JLab [87], BNL [88], KEK [89] and MAMI [90]. The GaAs photocathode in

Cornell University can produce an unpolarized electron beam with average current of 32 mA and can provide the electron beam up to 52 mA for a short time. [47] A GaAs/GaAsP SSL photocathode in CEBAF 200 kV inverted photogun can produce a polarized electron beam with average current of 150 μA and charge lifetime of 200 C. [87]

2.4 GaAs properties

The main advantage of GaAs over other Ⅲ-Ⅴ semiconductors is that it possesses the large direct bandgap that responds to the laser wavelength in the region of visible light and it can be achieved large band bending (i.e. large NEA level), leading to high quantum efficiency. [91] This section will review the GaAs crystal structure and energy band structure.

2.4.1 Crystal structure

GaAs is a type Ⅲ-Ⅴ compound semiconductor of elements gallium and arsenic. It was first created by Goldschmidt in 1929. [92] Table 2-2 shows some reference properties for GaAs. The GaAs has a zinc blende crystal lattice structure in which each atom is surrounded by four equidistant neighbor different atoms that lie at the corners of a tetrahedron. Such as Ga (As) atom is at (0, 0, 0) and the As (Ga) atoms is at (a/4, a/4, a/4). This structure contains four units of GaAs in a volume a^3. The bond between two nearest neighbors is composed of two electrons with opposite spins. The zinc blende lattice structure consists of two interpenetrating face-centered cubic (FCC) lattices.

Table 2-2: Material reference properties for bulk GaAs

Property	Parameter
Molecular weight	144.645 amu
Lattice constant (a)	5.65330 Å
Nearest neighbor distance (d)	2.44795 Å
Angle between bonds	109.47Å
Crystal density (dc)	5.32 g/cm3
Melting point (Tm)	1513±2 K
Specific heat capacity	0.327 J/g·K

The GaAs crystal lattice structure with the three main symmetry planes (100), (110) and (111) that defined by the Miller indices (hkl) is shown in Figure 2-6.`The effective atomic number densities for the GaAs (100), (110) and (111) cleave planes were calculated to be $8/a^2$, $4\sqrt{2}/a^2$, and $4\sqrt{3}/a^2$, respectively, where a is the GaAs lattice constant (5.6535 Å). The (100) and (110) planes possess equal amounts of Ga and As atoms at the surface, the (111A) plane comprise of only Ga atoms at the surface,

and the (111B) plane comprise of only As atoms at the surface. The most readily-cleave plane is the (110) plane, while the most commonly used cleave plane in the photocathode application is the (100) because this orientation provides the best cosmetic quality of the epitaxial layers and multilayer heterostructures. [93]

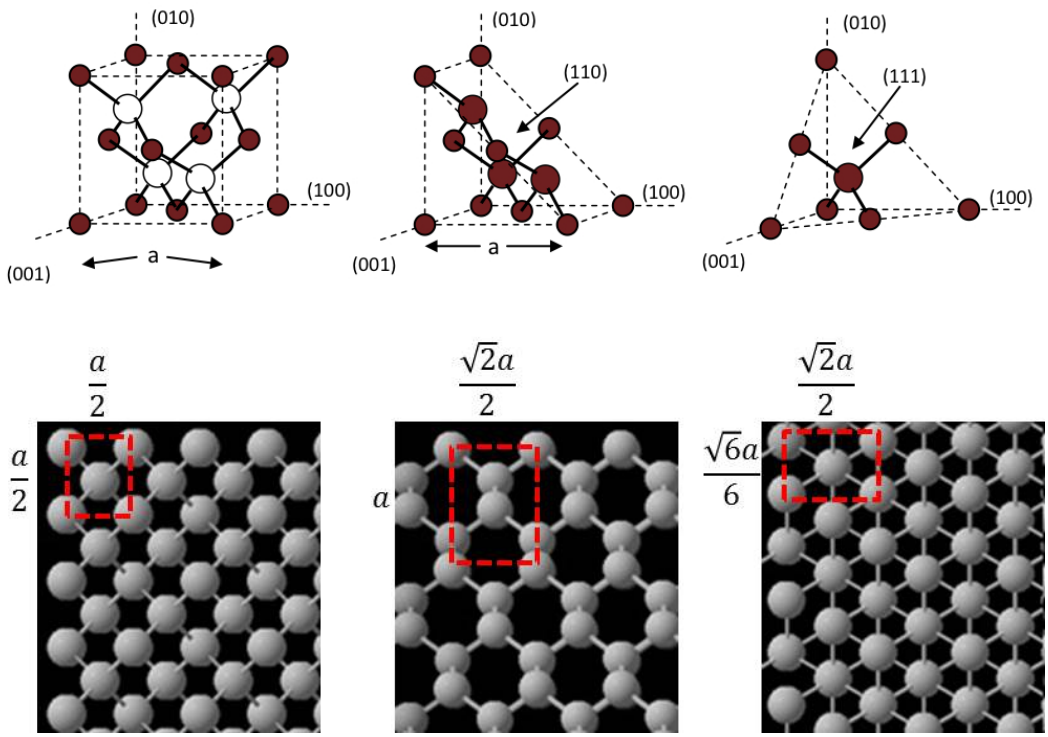

Figure 2-6: GaAs crystal lattice structure: (Up) showing the main symmetry planes: (100), (110) and (111) and (down) looking normal to the three cleave planes: (100), (110) and (111). The red box denotes the recurring geometric cell used for calculating the atomic number density for each cleave plane and $\boldsymbol{a}$ is the GaAs lattice constant

2.4.2 Energy band structure

According to the Pauli exclusion principle, the electrons occupy a set of discrete energy levels in a single, isolated atom. When as more atoms join to form into molecule, the energy levels come to so close to be considered to form a continuum: energy band. However, there are some leftover ranges of energy that aren't covered by any band, called band gaps. As a semiconductor, GaAs includes a set of upper energy bands, known as conduction band, and a set of lower energy bands, known as valence band. The separation between the top of the valence band and the bottom of the conduction band is called the bandgap. The energy band diagram of GaAs for room temperature is shown in Figure 2-7 [92]. The top of the valence band corresponds to the bottom of the conduction band at $\vec{k} = 0$ (Γ point), called direct bandgap. That means a photon with energy E_g is enough to pump an electron across the gap, and there is no need for a change in the momentum of the electron. Compared to the momentum of the electron, the momentum of the photon can be neglected, so there is almost no change in the momentum of the electron when the electron is excited from valence band to conduction after absorbing the energy of photon. As a result of, most of the electrons are excited in Γ valley.

The dispersion relation for the conduction band is given by [94]

$$E(\boldsymbol{k}) = E_{c0} + \frac{\hbar^2|\boldsymbol{k}-\boldsymbol{k}_{0c}|^2}{2m_e^*} \qquad 2\text{-}7$$

In which E is the energy, $\boldsymbol{k}$ is the wave vector of the electron, $E_{c0} = E_c(\boldsymbol{k}_{0c})$, m_e^* is the effective mass of the conduction band electron, $\boldsymbol{k}_{0c}$ is the $\boldsymbol{k}$ at the minimum energy.

The dispersion relation for the valence band is given by [94]

$$E(\boldsymbol{k}) = E_{v0} - \frac{\hbar^2|\boldsymbol{k}-\boldsymbol{k}_{0v}|^2}{2m_h^*} \qquad 2\text{-}8$$

In which $\boldsymbol{k}$ is the wave vector of the hole, $E_{v0} = E_v(\boldsymbol{k}_{0v})$, m_h^* is the effective mass of the hole in valence band, $\boldsymbol{k}_{0v}$ is the $\boldsymbol{k}$ at the maximum energy.

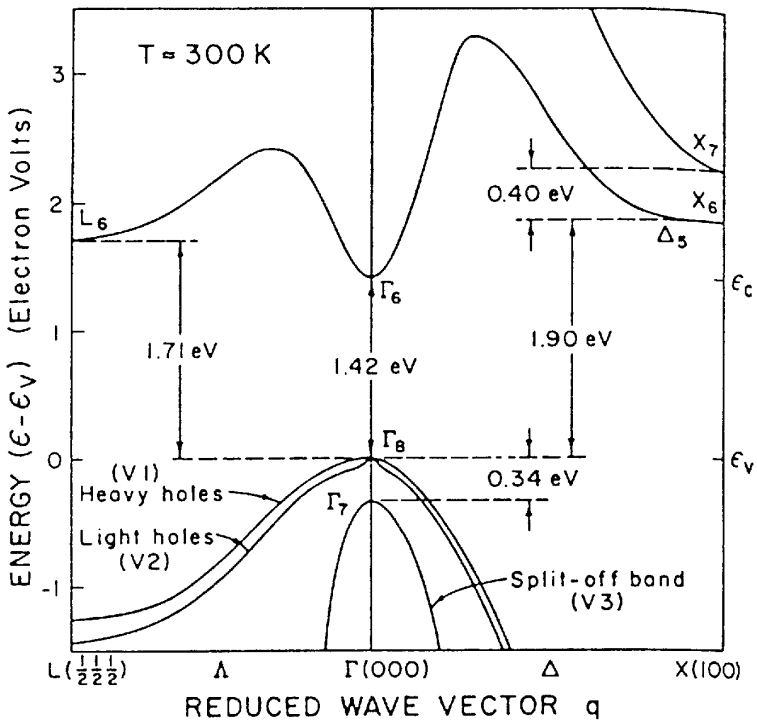

Figure 2-7: GaAs Energy bands diagram at room temperature.

The effective mass is given by

$$\frac{1}{m^*} = -\frac{1}{\hbar^2}\frac{\partial^2 E(k)}{\partial k^2} \qquad 2\text{-}9$$

Table 2-3 shows the parameters used to calculate the energy of the first conduction band (three valleys: Γ valley, L valley, and X valley) and the top 3 valence bands (heavy hole, light hole, and split-off band) of GaAs at room temperature.

The bandgap energy of semiconductors has strong temperature dependence, which tend to decrease as the temperature is increased. The bandgap energy (E_g) as a function of the temperature (T) is given by [95]

$$E_g(T) = E_g(0) - \frac{\alpha T^2}{T+\beta} \qquad 2\text{-}10$$

In which,α,β and $E_g(0)$are the fitting parameters. For the GaAs, the values are: $\alpha = 0.54\ meV/K$, $\beta = 204K$, $E_g(0) = 1.519eV$.

Table 2-3: The parameters used to energy band calculation for GaAs at room temperature

Symbol	Description	Value
Mass (kg)		
m_e	Mass of the electron in vacuum	9.109×10-31
m_Γ	Effective mass in Γ valley [92,96]	$0.063m_e$
m_L	Effective mass in L valley [96]	$0.555m_e$
m_X	Effective mass in X valley [96]	$0.851m_e$
m_{hh}	Effective mass in the heavy hole valence band [92]	$0.500m_e$
m_{lh}	Effective mass in the light hole valence band [92]	$0.076m_e$
m_{so}	Effective mass in the split-off valence band [92]	$0.145m_e$
Wave vector [92]		
$k_{0\Gamma}$	Wave vector at minimum energy of Γ valley	(0,0,0,)
$k_{0\mathrm{L}}$	Wave vector at minimum energy of L valley	(0.5,0.5,0.5)
$k_{0\mathrm{X}}$	Wave vector at minimum energy of X valley	(1,0,0)
$k_{0\mathrm{v}}$	Wave vector at maximum energy of valence band	(0,0,0)
Energy at room temperature (eV) [92]		
E_h	Energy at the top of the heavy and light hole valence band	0
E_{so}	Energy at the top of the split-off valence band	-0.34
E_Γ	Energy at the bottom of the Γ valley	1.42
E_L	Energy at the bottom of the L valley	1.71
E_X	Energy at the bottom of the X valley	1.90

High doping concentration also tends to decrease the bandgap energy of semiconductors. Figure 2-8 shows a curve of the change in the bandgap energy with the doping concentration. [95] One can see that the energy change can be ignored for doping less than $10^{18}\ cm^{-3}$. For a typically doping density $10^{19}\ cm^{-3}$ of most GaAs photocathode, the energy change is about $-60\ meV$. [95]

Different from metals whose Fermi level typically lies above the conduction band (i.e. electrons fill in the conduction band), GaAs has a mostly empty conduction band, therefore excited electrons in the conduction band of GaAs undergo little electron-electron scattering. This means the energy loss of electrons in the conduction is little, leading to the QE loss is little. Furthermore, GaAs has bandgaps large enough that thermionic excitation from the valence band to the conduction band is practically nonexistent at room temperature. This means there is almost no dark current occurring on the GaAs photocathode.

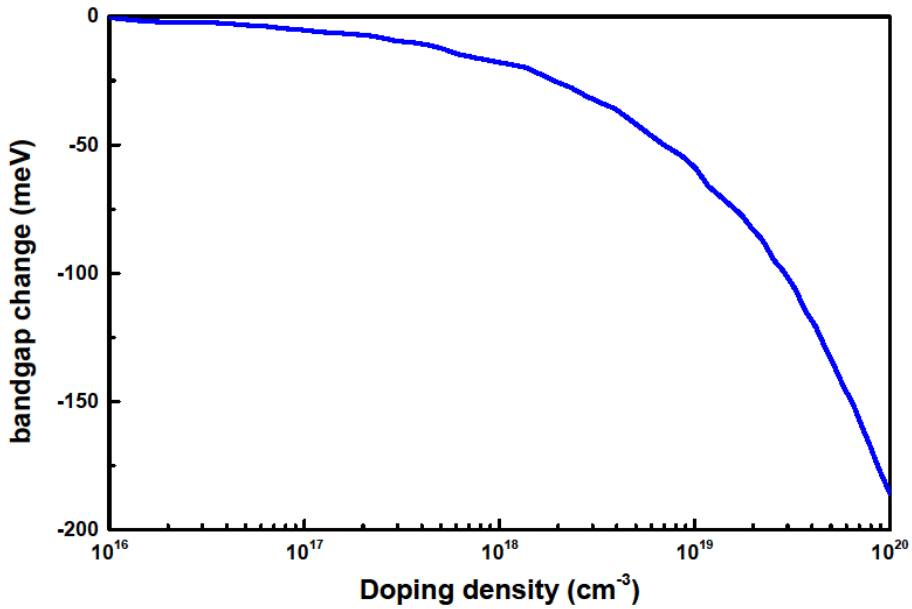

Figure 2-8: Doping concentration dependence of the bandgap energy for three common semiconductors

2.5 Photoemission process

The photoemission process from semiconductor photocathodes was first successfully explained by the Three-Step Model by William Spicer [67]. A breakthrough in the photocathode occurred with the advent of NEA photocathode. These photocathodes improved the photoemission yield (or quantum efficiency) by two orders of magnitude. This section will review the properties of NEA photocathode and the mechanism of forming NEA surface, then discuss the Spicer's Three-Step Model: the absorption of photons by a photocathode and the following photoexcitation, the transmission of the photoexcited electrons from inside of photocathode to the photocathode-vacuum interface, and the emission of electrons into the vacuum.

2.5.1 NEA photocathode

The Ⅲ-Ⅴ semiconductor photocathodes possess the great advantage to easy obtain NEA surface. GaAs is currently one of the most efficient photocathodes to form NEA surface. GaAs was first used as a photocathode in the 1960s. [97,98] J. J. Scheer and J. Van Laar firstly grew cesium (Cs) on the surface of p-type GaAs to reduce the electron affinity, which improved the probability of electron escape, and thus increased the QE of photocathode. Subsequently, J. J. Uebbing and L. W. James [62] found that the activation layer of Cs_2O can reduce the electron affinity more effectively than the Cs layer, thus achieving higher QE. By activating GaAs with Cs/Cs_2O layer, the vacuum energy level can be reduced to below the bottom of conduction band in GaAs, that is, the effective electron affinity is negative, or called negative electron affinity (NEA).

The energy band diagram for the formation of the NEA surface on GaAs is illustrated in Figure 2-9. [99] The diagram illustrates the energy (E) in vertical axis and the space coordinate (z) that is

perpendicular to the GaAs surface in the horizontal axis. At absolute zero temperature, all the electrons completely fill in the valence band. As the temperature increase, some electrons in the valence band are promoted into conduction band, leaving holes in the valence band. Electrons in the conduction band are prevented from escaping from the surface into vacuum by the surface potential called vacuum energy level, E_∞. The difference of energy between vacuum energy level and conduction band minimum (E_{CB}) is so called electron affinity (EA).

For intrinsic GaAs (as shown in Figure 2-9(a)), the vacuum level lies above the bottom of conduction, i.e. the EA is positive, this is so called PEA that prevent the escape of excited electrons in the conduction band from the surface into vacuum. To make the excited electrons escape from the surface into vacuum, the GaAs was fabricated to be NEA state whereby the vacuum level lies below the conduction band minimum. The NEA state can be formed by applying alkali metals (usually Cs) and oxidant (oxygen (O) or fluorine (F)) layer onto highly-doped p-type GaAs surface. [91]

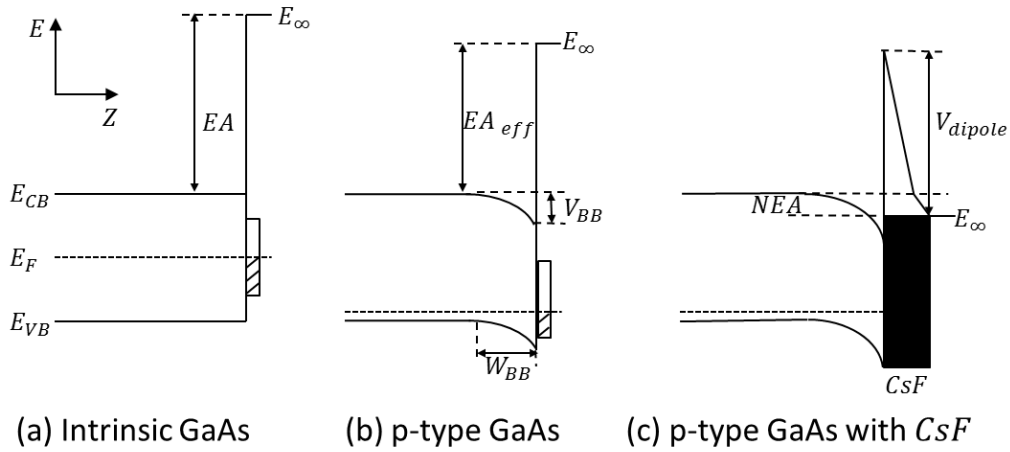

Figure 2-9: Energy band diagram for the formation of the NEA surface on GaAs. The diagram illustrates the energy (E) in vertical axis and the space coordinate (z) that is perpendicular to the GaAs surface in the horizontal axis. (a) Intrinsic GaAs: its large electron affinity makes it impossible for electrons in the bottom of the conduction band to escape. (b) p-type GaAs: acceptor impurities lead to lower the Fermi level and lead to band bend at the surface. (c) p-type GaAs with $\boldsymbol{CsF}$ (or $\boldsymbol{Cs_2O}$): the $\boldsymbol{CsF}$ (or $\boldsymbol{Cs_2O}$) layer tend to lower the potential barrier and lead to further bend of the energy band at the surface.

In the p-type GaAs, the acceptor impurity leads to additional energy levels in the band gap. The most commonly-used acceptor impurity for GaAs photocathode is zinc (Zn) with a typical concentration level in the range of $10^{18} - 10^{19}\ cm^{-3}$. At room temperature, most of the Zn atoms are ionized, having captured electrons from the valence band. Thus, holes are created in the valence band of which the concentration is approximately equal to the concentration of acceptors. Therefore the Fermi level will adjust itself by moving to the nearby of the valence band maximum (E_{VB}), as shown in Figure 2-9(b), to keep the number of holes equal to the number of electrons. [100] The Fermi level of p-type GaAs dependence on the acceptor concentration (N_A) is given by [101]

$$E_F = E_{VB} - kT\ ln\frac{N_A}{N_V} \qquad 2\text{-}11$$

where k is the Boltzmann constant, T is the absolute temperature of the material, N_V is the effective density of states in the valence band.

At the region of nearby the surface of p-type GaAs, the energy bands are bent downward by the amount V_{BB} as show in Figure 2-9(b) which makes it possible to form NEA surface. Large V_{BB} decreases the large EA that is reduced by amount of V_{BB} and makes it easier to form NEA surface, i.e. improve the escape probability of electrons. It is worth mentioning that the energy bands of n-type GaAs would be bent upward at the region of nearby the surface which makes it impossible to form NEA surface, because even if the vacuum level is zero at the surface, the EA is still positive. The width of band bending region W_{BB} is given by [102]

$$W_{BB} = \left(\frac{2\varepsilon V_{BB}}{eN_A}\right)^{1/2} \qquad 2\text{-}12$$

where ε is the dielectric constant (F/cm),V_{BB} is the amount of band bending (V), e is the electron charge (C), and N_A is the acceptor doping concentration (cm^{-3}).

When electrons pass through the band bending region, they will loss energy by scattering or recombination which is one of the mechanisms responsible for reducing the escape probability of electrons. To ensure a small energy loss of electrons in the band bending region, W_{BB} should be small, not more than a few times the hot electron scattering length. W_{BB} can be made small by using a high doping concentration. Unfortunately, high doping concentration cause a short diffusion length which reduce the quantum efficiency (QE) of photocathode [102,103], and cause high spin relaxation [104]. For thick photocathodes, increasing doping concentration will have the net effect of reducing the QE. However, for thin photocathodes (i.e. those whose active regions are less than the diffusion length of $\sim 1\mu m$), increasing doping concentration will improve the QE. [99] Thus the optimum doping concentration is a compromise between diffusion length and escape probability for thick photocathodes. A typical doping concentration level is the order of $10^{19}\ cm^{-3}$ that responds to the width of band bending region of 10 nm with V_{BB} of $0.3 - 0.5\ eV$. [105] Another method used to reduce the width of band bending region is to select the appropriate crystal plane at the surface. The (100) and (110) surface, possess equal amount of Ga and As atoms, have similar band bending potential V_{BB} and similar QE. The (111A) surface, comprised only of Ga atoms, has the largest V_{BB} and the lowest QE. The (111B) surface, comprised only of As atoms, has the smallest V_{BB} and highest QE. [81,102]

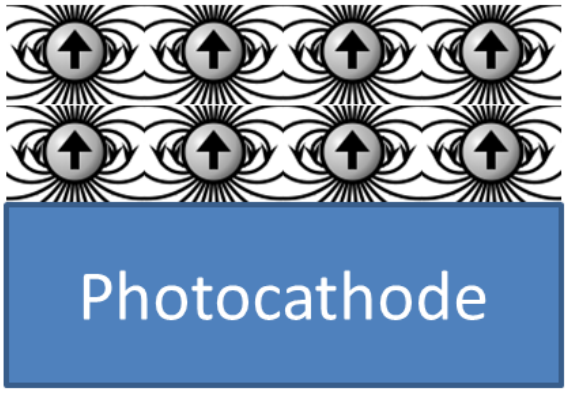

Figure 2-10: The electric dipole model on the surface (activation layer) of photocathode. The resulting electric filed help to electron escapes from photocathode into vacuum.

After applying Cs onto the high-doped p-type GaAs surface, the Cs atoms contribute their electrons to the GaAs, forming an electric dipole layer on the surface. The direction of resulting electric field is toward to the surface of GaAs (as shown in Figure 2-10), which help to electrons escape into vacuum. i.e., the electric field decreases the vacuum level and therefore reduces the EA. Co-deposition of oxidant (O or F) layers on the surface will enhance the electric, leading to enlarge the decrease of vacuum level (V_{dipole}) and reduction of EA. Application of enough Cs and oxidant layers causes to form the NEA state on the surface (as shown in Figure 2-9(c)). The Cs and oxidant layer gives the main contribution to the most important parameters of NEA GaAs photocathode, such as QE, operating lifetime, longitudinal and transverse energy spreads of emitted photoelectrons, the photocathode dark current, and the maximum value of emitted photocurrent, etc. [100]

Fluorine was first proposed in the 1980s [106] to replace oxygen as an oxidant to activate photocathodes. NF_3 is widely used as an oxidant material at present. [107,108] Nitrogen was also used as an oxidant to activate GaAs photocathode in order to study the effect of nitrogen on photocathode activation. [109,110] As mentioned in Ref. 109, GaAs photocathode can also be activated by yo-yo activation technology with Cs and N_2, but the QE is lower than that obtained by activation with Cs and NF_3. However, it was mentioned in Ref. 110 that nitrogen was useless for activating GaAs photocathode, and the reason why the QE increased during the activation was that nitrogen contained other oxidant components (such as oxygen). The activation layer of GaAs photocathode surface (Cs/NF3 activation) was also measured by XPS [100] and SR-PES (Synchrotron Radiation Photoelectron Spectroscopy) [108]. In Ref. 100, no nitrogen was detected in the activation layer, but only fluorine and cesium were detected. This indicates that nitrogen is useless in the activation process, and only fluorine binds cesium to form the activation layer. In Ref. 108, nitrogen was detected in the activation layer. However, nitrogen atoms combine with fluorine atoms to form N-F molecules (NF_x), but do not bond with cesium atoms, and do not affect the binding of fluorine atoms to cesium atoms. Therefore, it is reasonable to

believe that nitrogen in NF_3 has no effect on GaAs photocathode activation, and only fluorine has effect on the activation process.

A comparative study of the maximum QE obtained by Cs/NF_3 activation and Cs/O_2 activation shows that the maximum QE obtained by Cs/NF_3 activation is slightly higher than that obtained by Cs/O_2 activation. [100, 107] The explanation is that fluorine is more electronegative than oxygen. The electronegativity of fluorine is 3.98, whereas the electronegativity of oxygen is 3.44. The Cs-F electric dipole binds more tightly than the Cs-O electric dipole, resulting in a lower electron affinity, so the maximum QE obtained by Cs/NF_3 activation is higher.

In recent years, a new method has been proposed to activate GaAs photocathode by depositing a CsTe thin layer on the surface of GaAs. [111,112] When CsTe-GaAs photocathode irradiated by light with photon energy higher than 3.5 eV, it acts as CsTe photocathode. When the light with photon energy lower than 2.5 eV irradiated the CsTe-GaAs photocathode, it acts as NEA GaAs photocathode. The performance of CsTe-GaAs photocathode is strongly dependent on the thickness of CsTe and the activation process.

2.5.2 Three-Step Model

The photoemission in semiconductor photocathode was first successfully explained by William Spicer's Three-Step Model. This model indicates that the photoemission process consists of three steps: 1) the absorption of photons by electrons in the valence band of the photocathode and the following photoexcitation of electrons from the valence band into the conduction band; 2) the transportation of the photoexcited electrons from the inside to the surface of photocathode; 3) the emission of electrons into the vacuum. Figure 2-11 shows the photoemission process for the NEA GaAs photocathode.

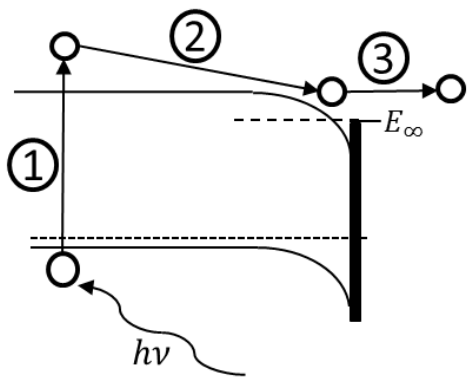

Figure 2-11: Spicer's Three-Step photoemission process for NEA GaAs photocathode: (1) the valence electrons absorb photons then excite into the conduction band; (2) excited electrons transport to the surface; (3) electrons emit into the vacuum.

The absorption of photons by electrons, first step, plays a critical role of determining the QE of photocathode. If the photocathode is illuminated by an incident light perpendicular to its surface, the

light intensity $I(z, h\nu)$ after it transverses a thickness z of the photocathode is given by the Buger's Law: [113]

$$I(z, h\nu) = (1 - R(h\nu))e^{-a(h\nu)z} \qquad 2\text{-}13$$

where $R(h\nu)$ is the reflectivity coefficient of the surface, and $a(h\nu)$ is the absorption coefficient for photocathode. It shows the intensity of the incident light decrease exponentially with thickness of the photocathode, z, which, in turn, implies the probability for a photon to be absorbed at the distance z from the photocathode surface. Both absorption and reflection coefficient for GaAs depend on photon energy (light wavelength). Figure 2-12 shows the spectrum of absorption coefficient for GaAs measured at a normal incident angle to the surface. [114,115] One can see that the absorption coefficient dramatically increase with photon energy, reaching to approximately $10^4\ cm^{-1}$ when the incident photon energy is close to the bandgap energy of GaAs (E_g~$1.4\ eV$), and then it strongly increase with photon energy. Figure 2-13 shows the spectrum of reflection coefficient for GaAs measured at a normal incident angle to the surface. [114,116] It is clearly seen that the reflection coefficient strongly depends on the incident photon energy.

Electrons absorb photons with energy ($h\nu$) exceeding the bandgap energy (E_g) of the photocathode and then be excited into the conduction band, leaving holes in the valence band. Due to the photon energy and negligible photon momentum, only those electrons in the heavy-hole (hh), light-hole (lh) and split-off (so) sub-bands with a specific set of $\vec{k}$-vectors matching the energy and momentum conservation condition can be excited to the conduction band. Therefore, the final energetic position of excited electrons is determined by the excitation energy (photon energy) and the band structure of photocathode. [117] According to energy and momentum conservation condition, the excited electron and hole both have initial energy that can be given by: [113]

$$E_{ie} = \frac{(h\nu - E_g)m_h^*}{m_e^* + m_h^*} \qquad 2\text{-}14$$

$$E_{ih} = \frac{(h\nu - E_g)m_e^*}{m_e^* + m_h^*} \qquad 2\text{-}15$$

where E_{ie} is the initial energy of electron, E_{ih} is the initial energy of hole, and m_e^*, $m_h^*$are the effective masses of electron and hole, respectively. It is noted that the initial energy of electron is calculated with reference to the conduction band minimum (E_{CB}).

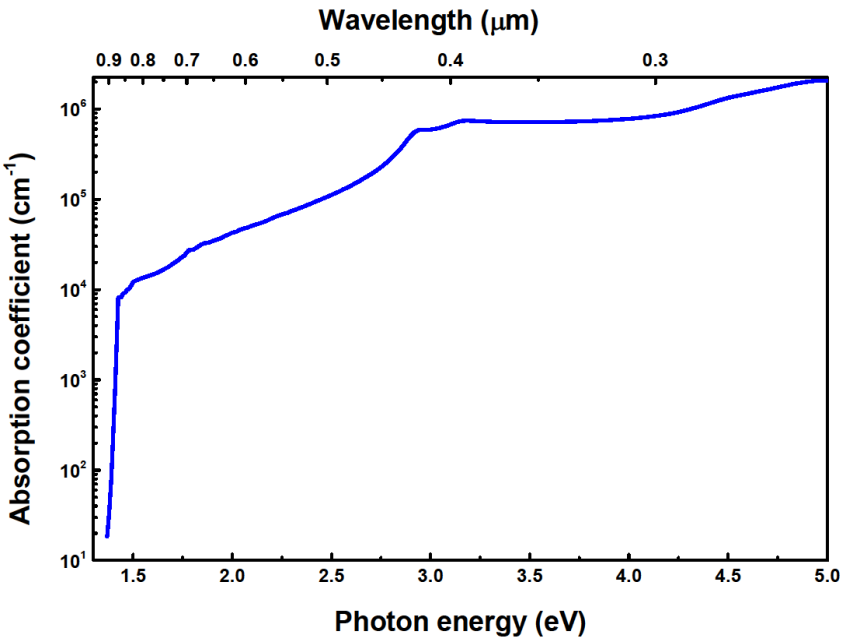

Figure 2-12: Spectrum of absorption coefficient for GaAs

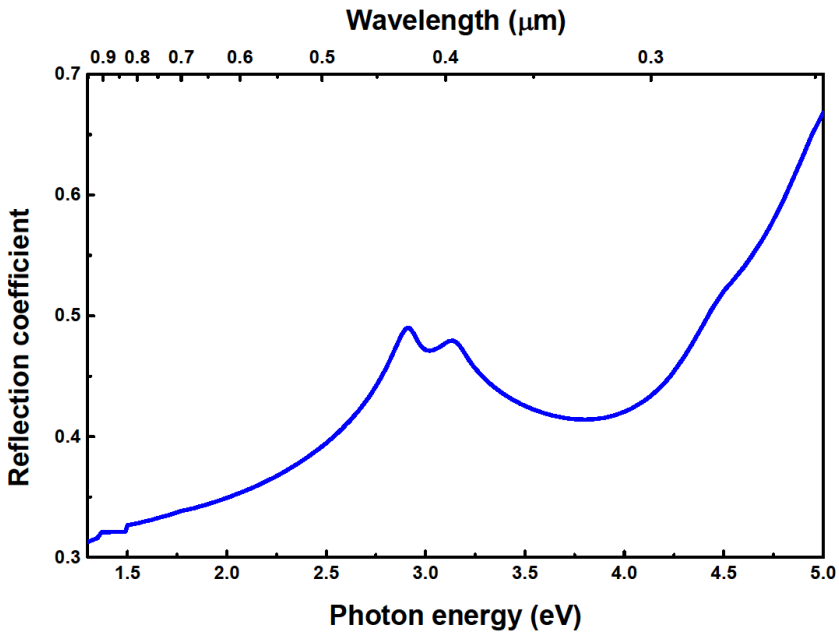

Figure 2-13: Spectrum of reflection coefficient for GaAs

During the second step, excited electrons, so called "hot" photoelectrons with "high" velocity ($v_e = \sqrt{2E_{ie}/m_e^*}$), will undergo scattering from the excited electrons, holes and phonons, and thus exchanging energy. The distance that the excited electrons can travel before its first scattering is called the momentum relaxation length,L_p, which can be estimated by:[113]

$$L_p = v_e \cdot \tau_p \qquad 2\text{-}16$$

where τ_p is the photoelectron momentum relaxation time which depend on the photoelectron energy and the electron scattering process presenting in the conduction band. For a highly-doped p-type GaAs with a typical hole concentration of $1 \times 10^{19}\ cm^{-3}$, the electron-hole collision is dominant in the scattering process and the τ_p is $\sim 10^{-13}\ s$ at room temperature [118]. Assuming that the excited electron with an effective mass $m_e^* = 0.063 m_e$ has an initial energy $E_{ie} \sim 0.17\ eV$ (780 nm laser illuminate), electron velocity v_e can be estimated to be of $\sim 10^6\ m/s$, and therefore the momentum relaxation length L_p can be calculated to be $\sim 100\ nm$. This means only those electrons which are excited within 100 nm from the photocathode surface and are diffuse toward the surface can be emitted directly into vacuum without losing their initial energy. However, the mount of electrons like this is very low and can be neglected in most cases due to the momentum relaxation length in the activation layer (Cs-O/Cs-F layer) is as small as $\sim 1\ nm$. [113]

Most excited electrons undergo further scattering and loss most energy before emitting into vacuum, leaving the energy same to the bottom of the conduction band minimum. This process is so called "thermalization" of hot electrons. The distance that the excited electrons can travel before thermalizing to the bottom of the conduction band minimum is called thermalization length, L_ϵ, which is roughly estimated to be $\sim 300\ nm$ for a heavily-doped p-type GaAs. The energy of thermalized electrons is concentrated within $\sim kT$ energy interval above the conduction band minimum, so that they can live typically for nanoseconds before they recombine with holes in the valence band, corresponding to the diffusion length, L, amounts to 4-5 μm for GaAs. [117] The diffusion length of thermalized electrons is much longer than the momentum relaxation length and the thermalization length, so the thermalized electrons are the main contribution to the photoemission from the NEA GaAs photocathodes in most cases, especially a thick active layer photocathode.

It is noted that the thermalized electrons also change their spin state during the transportation to the surface of photocathode. This process is so called spin relaxation (or depolarization) which is a predominant factor reducing the electron spin polarization of photocathode.

Excepting for a few parts of electrons recombining to the valence band, most electrons will reach the photocathode surface. These electrons can either escape into vacuum or get trapped at the surface, and these trapped electrons (or surface charge) will recombine to the valence band (called surface recombination). When the photocurrent is low, i.e., the photoemission is in linear mode, the rate at which the electrons gets trapped at the surface is the same as the rate at which the surface charge recombines to the valence band, and the emitted electrons is proportional to the excited electrons density. When the photocurrent is increased to high, i.e., the photoemission is in saturation mode, the rate at which the electrons gets trapped at the surface is bigger than the rate at which the surface charge recombines to the valence band, leading to charge accumulates at the surface which in turn raises the surface potential barrier. The rise of in the surface potential barrier reduces the probability of escape of

electrons and thus reduces the emitted electron current. [99] The rate of surface recombination is larger in high-doped semiconductors than low-doped semiconductors, so it takes a higher rate of trapped electrons to reach saturation. For this reason, high-doped photocathodes can achieve larger photocurrent before reaching saturation than low-doped photocathodes.

The most common method to quantify the effectiveness of a photocathode is measuring its QE that is defined as the number of electrons emitted per incident photon. The basic QE equation for a semi-infinite slab semiconductor was derived by Spicer based on Three-Step Model and given by: [46]

$$QE = (1 - R)\frac{\frac{\alpha_{PE}}{\alpha}P_E}{1+\frac{l_\alpha}{L}} \qquad 2\text{-}17$$

where R is reflection coefficient for the surface of photocathode, α_{PE} is the absorption coefficient for electrons excited above the vacuum level, α is the absorption coefficient for the photocathode, P_E is the probability of escape of surface electrons, $l_\alpha = 1/\alpha$ is the photon absorption length, and L is the electron diffusion length. All the variables depend on the wavelength of incident light, the temperature of photocathode, and the doping concentration.

The QE equation says that the number of emitted electrons is proportional to each of the following: the absorbed light, the fraction of electrons excited above the vacuum level, and the probability of escape of surface electrons. And the QE is also inversely proportional to the factor $1 + l_\alpha/L$, which indicates that the electron emission is small for a very small diffusion length or for a very large absorption length relative to diffusion length (i.e. electrons excited deep in the photocathode will likely not be able to reach the surface and be emitted). As mentioned before, the main contribution to the photoemission for GaAs is thermalized electrons whose diffusion length L corresponding to 4-5 μm, and the photo absorption length l_α is 0.1-1 μm (visible light) in GaAs. The absorption length is smaller than the diffusion length, thus the GaAs photocathode can achieve a good QE in the visible light region (respond to the bandgap energy of GaAs).

2.6 Spin-polarized electrons

Electrons with a net spin state are called spin-polarized electrons which play a critical role in nuclear and high energy physics research. GaAs can produce electrons with a theoretical electron-spin polarization (ESP) of 50% by illuminating with circularly polarized light. And a completely strained GaAs can provide electrons with ESP close to 100%. However, the ESP observed in the laboratory is less than 50% for unstrained GaAs photocathodes and less than 100% for strained GaAs photocathodes, which mainly caused by the depolarization process in the photocathodes.

2.6.1 Unstrained GaAs

The energy band structure of unstrained GaAs shows the spin-orbit coupling splits the valence band into $P_{3/2}$ and $P_{1/2}$ with a residing band $\Delta = 0.341$ eV at the Γ point, and electrons in each band are

polarized. If the GaAs is illuminated with circularly polarized light of energy between E_g and $E_g + \Delta$, the polarized electrons will be produced. Figure 2-14 shows the energy band diagram of GaAs and the optical transitions between sublevels for circularly polarized light. The selection rules for right and left circularly polarized light absorbed by electrons are $\Delta m_j = +1$ and -1, respectively. The relative transition probabilities for the $m_j = \pm 3/2$ and $m_j = \pm 1/2$ states of P3/2 band to conduction band ($\pm 1/2$ and $\mp 1/2$) are 3 and 1, respectively. Thus, the ideal spin polarization of electrons excited to the conduction band is $P = \frac{3-1}{3+1} = 50\%$ when incident circularly polarized light has energy of $E_g < h\nu < E_g + \Delta$. Obviously, if the photon energy $h\nu > E_g + \Delta$, the spin polarization of excited electrons is zero.

At the early development of polarized electron sources, unstrained GaAs was used to provide polarized electrons. However, as the development of strained GaAs and strained superlattice GaAs photocathode which can provide ESP higher than 50%, unstrained GaAs preferred to be used to provide unpolarized electrons because of its high QE. [119]

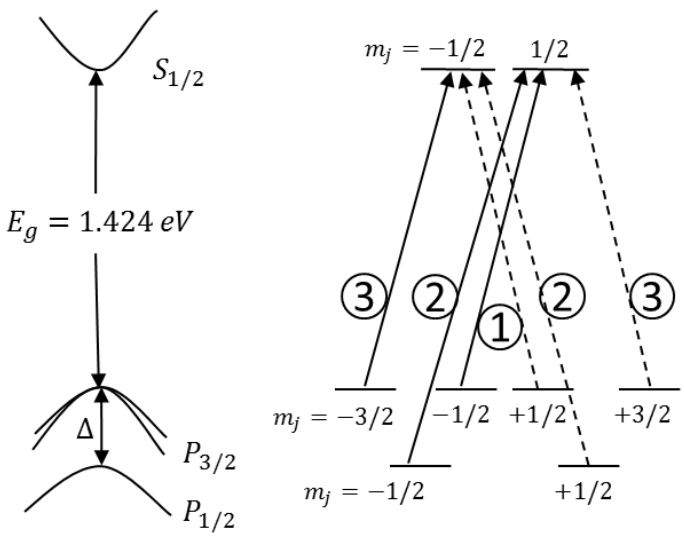

Figure 2-14: The energy bands diagram of unstrained GaAs at the center of Brillouin zone and the optical transitions between sublevels for circularly polarized light, right circularly polarized light (solid lines) and left circularly polarized light (dashed lines), with the relative transition probabilities given by circled numbers.

2.6.2 Strained GaAs

Growing GaAs on a crystal structure (such as GaAsP) with a different lattice constant can induce uniaxial strain that eliminates the degeneracy of the valence band. Figure 2-15 shows the energy band diagram of strained GaAs and the optical transitions between sublevels for circularly polarized light. The energy band diagram shows the strain eliminates the degeneracy between heavy-hole and light-hole of the valence band and makes it split of energy level of δ. When the strained GaAs is illuminated with a circularly polarized light of energy between E_g and $E_g + \delta$, electrons with an ideal ESP of 100% will be excited to conduction band.

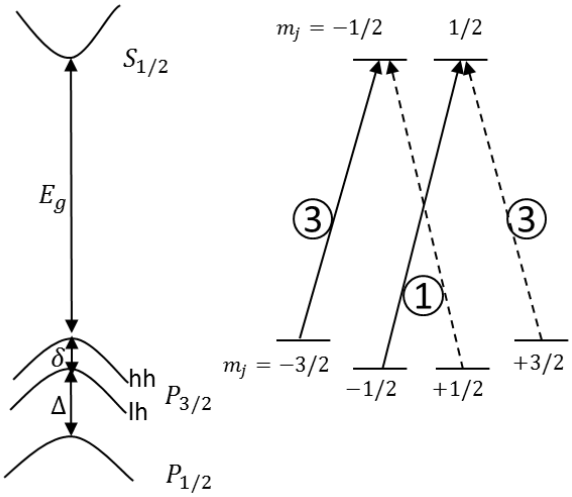

Figure 2-15: The energy band diagram of strained GaAs at the center of Brillouin zone and the optical transitions between sublevels for circularly polarized light, right circularly polarized light (solid lines) and left circularly polarized light (dashed lines), with the relative transition probabilities given by circled numbers.

The level of splitting energy δ between heavy-hole and light-hole determines the ESP of photocathodes and the bandwidth of the maximum ESP. Enlarging the splitting energy δ leads to better ESP. The splitting energy for GaAs grown on another crystal structure (barrier layer) is given by: [83]

$$\delta = -2b\left(\frac{C_{11}+2C_{12}}{C_{11}}\right)\epsilon \qquad 2\text{-}18$$

where parameter b is the uniaxial deformation potential for tetragonal strain ($b = -1.76\ eV$ for GaAs), C_{ij} represent the elastic-stiffness constants ($C_{11} = 11.88 \times 10^{11} dyn/cm^2$, $C_{12} = 5.32 \times 10^{11} dyn/cm^2$ for GaAs) 120, and ϵ is the lattice-mismatch and given by:

$$\epsilon = \frac{a_0 - a}{a} \qquad 2\text{-}19$$

where $a_0$and a are the lattice constants of the unstrained GaAs and crystal of barrier layer, respectively. For typical strained GaAs/GaAsP$_x$ photocathode, the lattice-mismatch $\epsilon = 0.126$ for $x = 0.35$, leading to the splitting energy $\delta = 81\ meV$. If $\epsilon > 0$, the strain is compression strain and the heavy-hole band shifts above the light-hole band; If $\epsilon < 0$, the strain is tension strain and the light-hole band shifts above the heavy-hole band.

When the thickness of the strained GaAs layer is beyond a critical thickness (d_c), the strain will relax by forming misfit dislocations, leading to the decrease of degree of strain and therefore decrease of ESP. For the strained GaAs/GaAsP photocathode, the critical thickness $d_c = 6.8\ nm$, and such a thin GaAs layer can only provide very low QE. Thus, there is a delicate competing balance for single-strained-layer photocathodes between maintaining the required degree of strain and growing a layer thicker enough to provide enough QE.

To obtain higher QE and maintaining the high ESP, SSL structures consisting of very thin quantum-well active layers and alternating lattice mismatched barrier layers were developed. The superlattice structure maintains the required degree of strain to produce high ESP and provides enough active layer thickness to obtain higher QE. More details about strained superlattice photocathodes will be discussed in chapter 4.

2.6.3 Depolarization process

The spin relaxation (or depolarization) of thermalized conduction electrons is the predominant factor reducing the electron spin polarization of photocathode. The investigation of spin relaxation has a long history dating back to the 1950s. There are three main spin relaxation mechanisms for III-V semiconductor: 1) The spin-orbit interaction, called Elliot-Yafet (EY) mechanism. [121, 122] 2) The lack of inversion symmetry in III-V semiconductor leads to a spin splitting of the conduction band, called D'yakonov-Perel (DP) mechanism. [123] 3) The exchange interaction mechanism between electrons and holes, called Bir-Aronov-Pikus (BAP) mechanism. [124] For p-type GaAs (used for photocathode), the BAP mechanism is dominant at low temperature and high dopant concentration, and the DP mechanism is dominant at high temperature and low dopant concentration. [125,126]

The GaAs material is lack of inversion symmetry that is broken by the presence of two distinct atoms in the Bravais lattice, which induce the momentum states because of the spin-up and spin-down electrons are not degenerate: $E_{\boldsymbol{k}\uparrow} \neq E_{\boldsymbol{k}\downarrow}$. The resulting energy difference plays the role of effective magnetic field and results in spin precession during the time between collisions, which contribute to spin relaxation due to the magnitude and direction of $\boldsymbol{k}$ changes in an uncontrolled way. This is so called DP mechanism. The DP mechanism depends on the temperature, and the temperature dependence of spin relaxation rate for DP mechanism is $1/\tau_s^{DP} \sim T^3 \tau_p \sim T^{9/2}$. [127]

In p-type GaAs, the spin relaxation can also result from the spin exchange interaction between electrons and holes. This is so called BAP mechanism. The BAP mechanism depends on the temperature and doping concentration because of it depends on the exchange interaction between electrons and holes. There are two situations: nondegenerate holes and degenerate holes. The dependence on the acceptor density is essentially $1/\tau_s^{BAP} \sim N_A$ for nondegenerate holes and $1/\tau_s^{BAP} \sim N_A^{1/3}$ for degenerate holes. In between, $1/\tau_s^{BAP}$ is only weakly dependent on N_A. The temperature dependence for degenerate holes is $1/\tau_s^{BAP} \sim T^{3/2}$. [127]

From the spin relaxation mechanism, we know that the doping concentration and temperature is the main factors affected the ESP of photocathodes. It is also noted that there are some other factors that also affect the ESP of photocathodes, such as the NEA surface layer (Cs-F layer). Chapter 3 will discuss the factors affected the ESP of photocathodes in detail.

2.6.4 Theory of measuring Polarization

The spin polarization of electron can be measured by Mott polarimeter, which is based on the Mott scattering that describes the spin-orbit interaction between the beam electrons and atomic nuclei. [128] The motion of electron around the nucleus results in a magnetic field $\boldsymbol{B}$ given by

$$\boldsymbol{B} = \frac{Ze}{cr^3}\boldsymbol{r} \times \boldsymbol{v} = \frac{Ze}{mcr^3}\boldsymbol{L} \qquad 2\text{-}20$$

where Z is the atomic number of the nucleus, e and m are the charge and mass of the electrons, respectively, c is the speed of light, r is the distance between the electron and the nucleus, $\boldsymbol{L}$ is the electron orbital angular momentum. The interaction of this magnetic field with the electron spin magnetic moment ($\boldsymbol{\mu_s} = -\frac{ge}{2mc}\boldsymbol{S}$, $\boldsymbol{S}$ is the electron spin) introduces a term (Hamiltonian) $\boldsymbol{H} = \boldsymbol{V} = -\boldsymbol{\mu_s} \cdot \boldsymbol{B}$ in the scattering potential, which is so called spin-orbit interaction potential given by

$$\boldsymbol{H} = \frac{Ze^2}{2m^2c^2r^3}\boldsymbol{L} \cdot \boldsymbol{S} \qquad 2\text{-}21$$

The spin-orbit interaction will introduce the spin dependence in the scattering cross section $\sigma(\theta)$ between the electron and nucleus, which is given by

$$\sigma(\theta) = I(\theta)[1 + S(\theta)\boldsymbol{P} \cdot \boldsymbol{n}] \qquad 2\text{-}22$$

where $I(\theta)$ is the differential cross section for unpolarized electrons scattered through the angle θ, $S(\theta)$ is the asymmetry (or Sherman) function of the target, $\boldsymbol{P}$ is the incident electron spin polarization, $\boldsymbol{n}$ is the unit vector for normal incident to the scattering plane which is parallel to $\boldsymbol{L}$. [129] The term $S(\theta)\boldsymbol{P} \cdot \boldsymbol{n}$ is largest when the polarization vector is perpendicular to the scattering plane.

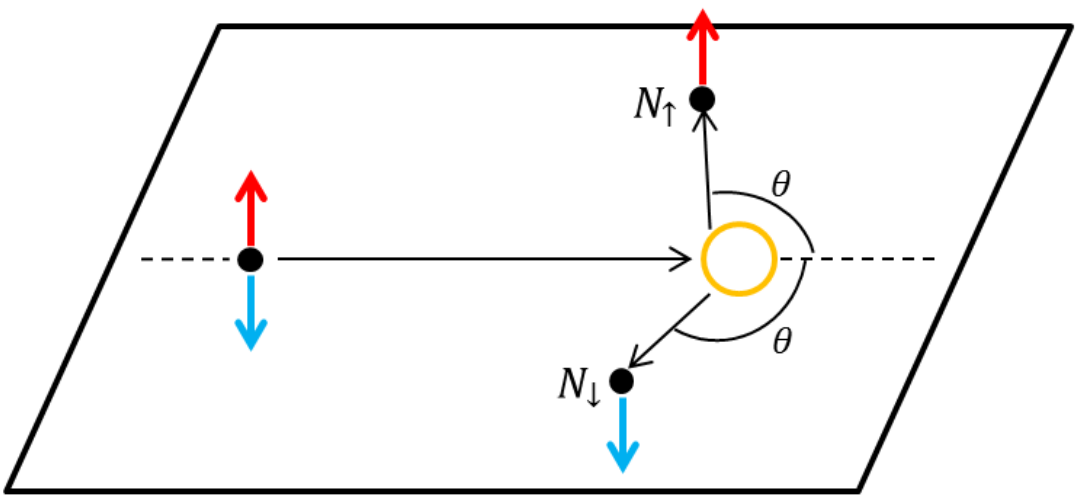

Figure 2-16: Spin-polarized electrons incident to the target and scatter with target nuclei. Spin-up electrons tend to (red arrows) scatter toward left, and spin-down electrons tend to (blue arrows) scatter toward right

Figure 2-16 shows the process of electrons with polarization incident to the target and scatter with target nuclei. The scattering plane is defined by the incident electron beam and their scattering direction.

When a beam of electrons with a polarization $\boldsymbol{P}$ that is perpendicular to the scattering plane transverse on the scattering plane to the target, the spin-up electrons tend to scatter toward left, and the spin-down electrons tend to scatter toward right. So, the number of $N_\uparrow$ is proportional to $1 + PS(\theta)$, and the number of $N_\downarrow$ is proportional to $1 - PS(\theta)$. These scattering polarized electrons result in a scattering asymmetry defined as

$$A(\theta) = \frac{N_\uparrow - N_\downarrow}{N_\uparrow + N_\downarrow} = PS(\theta) \qquad 2\text{-}23$$

From this equation, the polarization can already be obtained by measuring the left (spin-up) and right (spin-down) scattered electron number. However, the detectors used to measure the electrons numbers, in practical, usually present instrumental asymmetries (like misalignments, unequal detector responses), which results in the erroneous value for electron number and therefore the erroneous value of polarization. To eliminate the effects of the instrumental asymmetry, the scattered electron number are detected repeated after changing the electron-spin orientation by optically flipping the polarization of photons (for instance, change from left-handed circularly polarized light to right-handed circularly polarized light). And the polarization can be given by

$$P = \frac{1}{S_{eff}} A \qquad 2\text{-}24$$

with

$$A = \frac{\Delta - 1}{\Delta + 1}, \Delta = \sqrt{\frac{L_\uparrow R_\downarrow}{L_\downarrow R_\uparrow}} \qquad 2\text{-}25$$

where $L_\uparrow$ ($R_\uparrow$), $L_\downarrow$ ($R_\downarrow$) represent the electron number on the left (right) detector before and after changing the electron-spin orientation, respectively. [130,131] $L_\uparrow$, $R_\downarrow$ are proportional to $1 + PS$, and $L_\downarrow$, $R_\uparrow$ are proportional to $1 - PS$.

The value of effective asymmetry (Sherman) function S_{eff} depends on electron energy, target foil thickness, specific detector geometry, etc., and can be determined in a number of methods. One traditional method is to measure the scattering asymmetry for foils of different thickness and then extrapolate to zero foil thickness where the data are normalized to the theoretical scattering asymmetry for single atom scattering. [132,133] A second method involves a double-scattering experiment in which initially unpolarized electrons scatter from two equivalent targets, and S_{eff} is measured directly. [134,135] The third method is that use a beam of electrons with known polarization to calibrate the Mott polarimeter. [136,137,138] Our Mott polarimeter use the third method to determine the value of S_{eff}. By this method, we just need a beam of electrons with known polarization of P_0, and measure the value of scattering asymmetry A_0, then the value of S_{eff} can be calculated by $S_{eff} = A_0/P_0$.

Chapter 3 Research of polarization photocathode

3.1 Experimental apparatus and technology

Both the activation and measurement of photocathodes are performed in ultra-high vacuum (UHV) chamber. In usual, the photocathode sample is attached on the sample holder within the vacuum chamber and activated using yo-yo activation technology with Cs and NF_3 to form NEA. The QE was measured and analyzed by picoammeter and laser power meter. The ESP was measured by a low-voltage retarding-field Mott polarimeter. This section will introduce the experimental apparatus and technology used for the research of the thesis, including two vacuum chamber system, photocathode activation system/technology, UHV system/technology and the Mott polarimeter.

3.1.1 UHV system

Two vacuum chambers were used for our research. All the chambers can be used to activate the photocathodes and measure QE. The main difference between them is that one chamber possesses a hydrogen ion source and another chamber possesses a Mott Polarimeter. The chamber with hydrogen ion source is called H1 chamber in the thesis, and the chamber with Mott Polarimeter is called mini-Mott chamber.

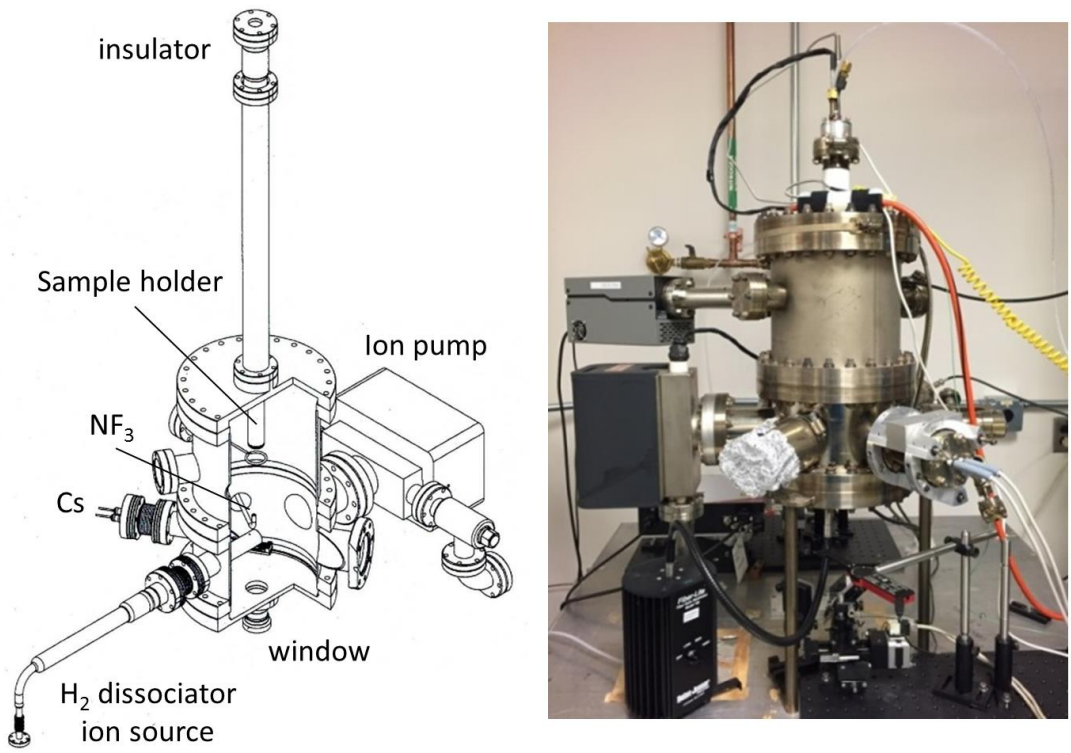

Figure 3-1: Schematic representation of the H1 chamber (left) and a photograph of the chamber (right).

Figure 3-1 shows the schematic representation and photograph of the H1 chamber. The hydrogen ion source is originally used to clean photocathode but used in thesis as ion source for ion implantation (discussed in chapter 4). A series of pumps are used in the chamber to get UHV: low vacuum pump system (turbo pump integrated with diaphragm backing pump), ion pump and Non-Evaporable Getter (NEG) pump. A Residual Gas Analyzer (RGA) is installed in the chamber to detect the component gases present and pressure.

The low vacuum pump system (from Pfeiffer Vacuum Company) consists of a turbo pump and diaphragm backing pump, which provide a pumping speed of 30 l/s. This pump system can operate from the atmosphere pressure to 10^{-8} Torr. Figure 3-2 shows a photograph of the low vacuum pump system. The pump system was connected to chamber with Klein flange (KF) and there is a valve between the chamber and pump. The pump-down time of the pump system is fast, and it takes approximately 10-20 minutes to pump H1 chamber from atmospheric pressure to 10-7 Torr where we open the ion pump to obtain higher vacuum.

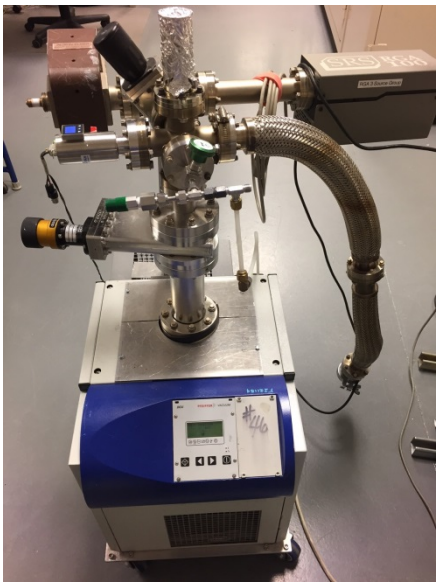

Figure 3-2: A photograph of the low vacuum pump system

Ion pump installed in our chamber are from Physical Electronic company and Gamma Vacuum company. The schematic representation of ion pump structure is shown in Figure 3-3. After the ion pump is turned on, free electrons get pulled towards the anode, but get caught in the magnetic field and rotate around it. They are bound to hit a gas molecular and ionize the molecular, creating positively charge molecular within the positive anode tube. The positively charge molecular accelerates towards the titanium cathode at high velocity and impact the titanium cathode. This sputters titanium onto the anode walls and the original charge molecular chemically combines with the titanium. This means the number of gas molecular in the vacuum decreases and therefore a higher vacuum is created. The ion pump can pump most of the partial gas within the chamber but is not effective for hydrogen gas because the hydrogen ion is hard to combines with titanium. The vacuum pressure within the ion pump can be

indicated by the electric current reading from the HV supply. In the ion pump, the production rate of ions that determines the electric current level is linear to the vacuum pressure, so that the vacuum pressure is almost linear to the electric current in the pressure region required by our research of the thesis and the relation between them is given by: 1A = 10^{-3} Torr.

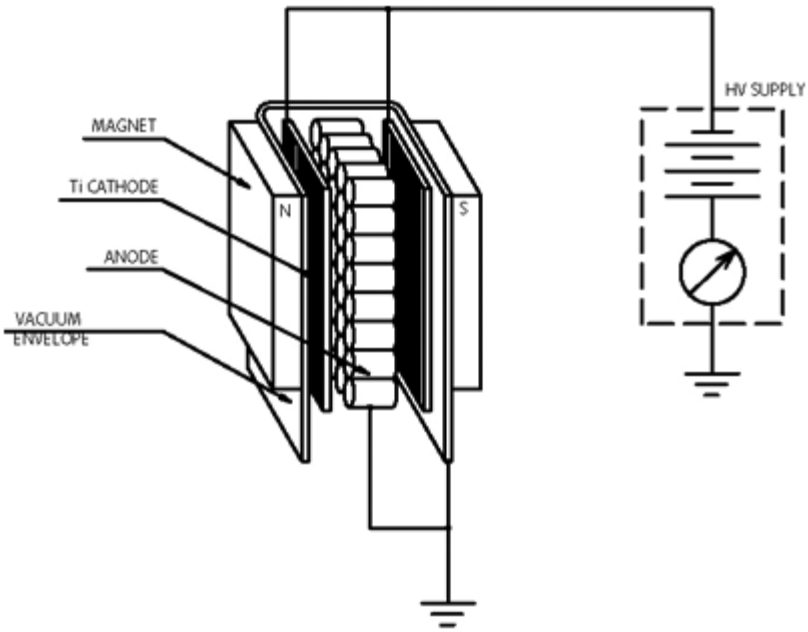

Figure 3-3: Schematic representation of ion pump structure

A NEG pump (from SAES Getter Company) is used together with ion pump to help to get higher vacuum, which exhibits a high pumping speed for all active gases (especially for hydrogen gas). NEG pump removes or pumps active gases by gettering (chemically combining) gases with metal alloys. NEG modules are made of pleated copper-nickel alloy Constantan strips coated with St 707 (or St 101), a reactive zirconium-vanadium-iron powder mixture (or zirconium-vanadium-aluminum mixture). St 707 reduces the chamber pressure by gettering or chemisorbing active gases like O_2, CO, and N_2 permanently on the surface of getter base material. H_2 and its isotopes diffuse into the getter material forming a solid solution, which can later be released at higher temperature. NEG pump does not pump noble gases, but they can used to purify the inert/noble gases. Figure 3-4 shows a photograph of NEG pump. The metallic strip was folded many times in order to obtain a more compact pump unit, having the same active surface.

The St 707 in the module will become saturated with active gases after operating long time, and its pumping speed decreases. At the saturation point, heating it by giving it electric current can reactivate the strip. This diffuses active gases like O_2, CO, and N_2 deeper into the wafer structure and release the hydrogen. NEG pump has a high capacity, which means a very long lifetime.

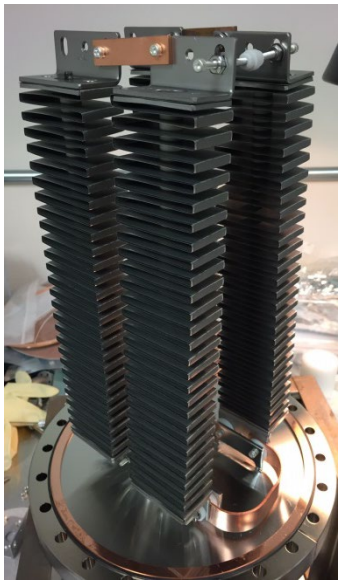

Figure 3-4: The photograph of a NEG pump

To get Ultra-High Vacuum (UHV), bake the entire chamber is to be performed. The procedure of UHV achievement for H1 chamber is listed as follows:

1) Pump down the chamber to 10^{-6} Torr by the low vacuum pump system. Then open the below ion pump that will not be bake.
2) Bake the entire chamber at 200°C for 36 hours, then cool down to 120°C and bake it at this temperature for 4 hours.
3) Turn on the main ion pump while the bake temperature is 120°C. Close the valve connected to low vacuum pump system and the below ion pump, aimed to separate the baked system and unbaked system. And then, activate the Non-Evaporable Getter (NEG) pump with 15A for 1 hour
4) After bake, degas the RGA detector for 2 hours and degas the cesium dispenser with 3.5A for 1 hour. Meanwhile, degas the cathode at 300°C for 30 minutes.
5) After a few hours, the vacuum reaches to 10-11 Torr scale.

RGA (shown in Figure 3-5) is used to provide detailed gas analysis of vacuum system. The RGA is a mass spectrometer consisting of a quadrupole probe and an Electronics Control Unit (ECU) which mounts directly on the probe's flanges and contains all the electronics necessary to operate the instrument. The quadrupole probe consists of an ionizer, quadrupole mass filter, and a detector. The ionizer converts many neutral gases molecular into positive ions in a well-controlled region at a specified electric potential. These ions are next accelerated by a series of electrostatic "lenses" and formed into a beam. The ion beam is subsequently passed into the quadrupole mass filter, in which ions with a user chosen mass to charge ratio (M/e) will very nicely pass through but all the other ions get pushed aside into walls where they neutralize and become undetectable. The ions that are passed through this filter are detected as current at detector (Faraday cup). By choosing a mass to charge ratio

and making a measurement of the signal obtained, one can immediately find out the number of those molecules present in the ionizer region of the RGA, and therefore find out those gases pressure if the RGA has been calibrated. By sweeping through a whole range of M/e ratios, one can find the full range of chemical components in the gas and their partial pressure.

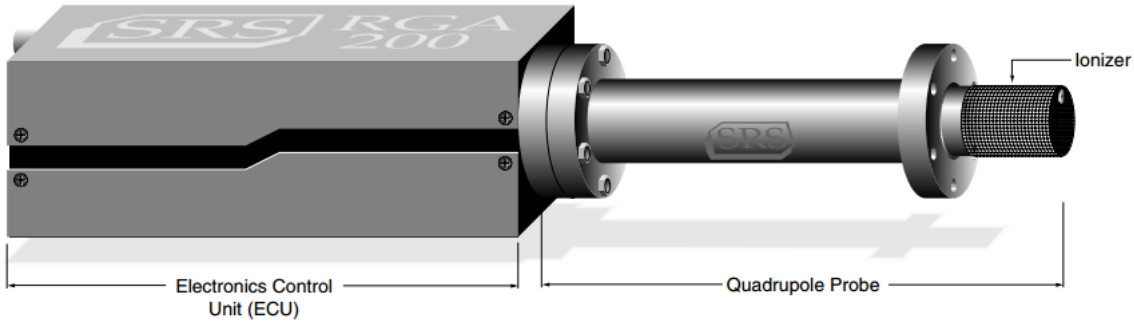

Figure 3-5: The RGA components

Table 3-1 shows the residual gases partial pressure in the H1 chamber measured by RGA when the vacuum pressure is 1.12×10^{-11} Torr reading from ion pump. H_2 is the main gas in the chamber, but it was not big bad for quantum efficiency. All the oxide is the main factor of quantum efficiency decrease. Most of CO_2 and CO comes from RGA probe, so they can be suppressed by turning off RGA before activation. So, the vapor water comes to be the main factor of quantum efficiency decay.

Table 3-1: The residual gases partial pressure in H1 chamber

Mass	Pressure (Torr)	Gas
2	1.37×10^{-10} (76.9%)	H_2
28	1.15×10^{-11} (6.45%)	N_2/CO
19	1.02×10^{-11} (5.72%)	HO/F
44	8.31×10^{-12} (4.66%)	CO_2
18	6.81×10^{-12} (3.82%)	H_2O
16	2.22×10^{-12} (1.25%)	O/CH_4
17	2.15×10^{-12} (1.21%)	HO/NH_3

Figure 3-6 shows a photograph of mini-Mott chamber that possesses a Mott polarimeter used to measure ESP of photocathodes (discussed in section 2.6.4). The pump system in mini-Mott chamber is almost same with that in H1 chamber. The procedure of UHV achievement for this chamber is also same to H1 chamber. However, this chamber possesses a load-lock bellows that make it avoid baking whole chamber during changing the photocathode sample. The procedure of changing photocathode sample and UHV achievement is listed as follows:

1) Raise the stalk (sample holder) then close the separate valve to divide the chamber to two part: upper chamber (load-lock bellows) and below chamber.
2) Open upper chamber and change the photocathode.

3) Pump down the upper chamber to 10-6 Torr by the low vacuum pump system. Then open the ion pump and close the valve connected to low vacuum pump system.
4) Bake the upper chamber at 250 °C for 24 hours then cool down to room temperature
5) After bake, open the separate valve and lower the stalk to below chamber.
6) After a few hours, the vacuum reaches to 10-11 Torr scale.

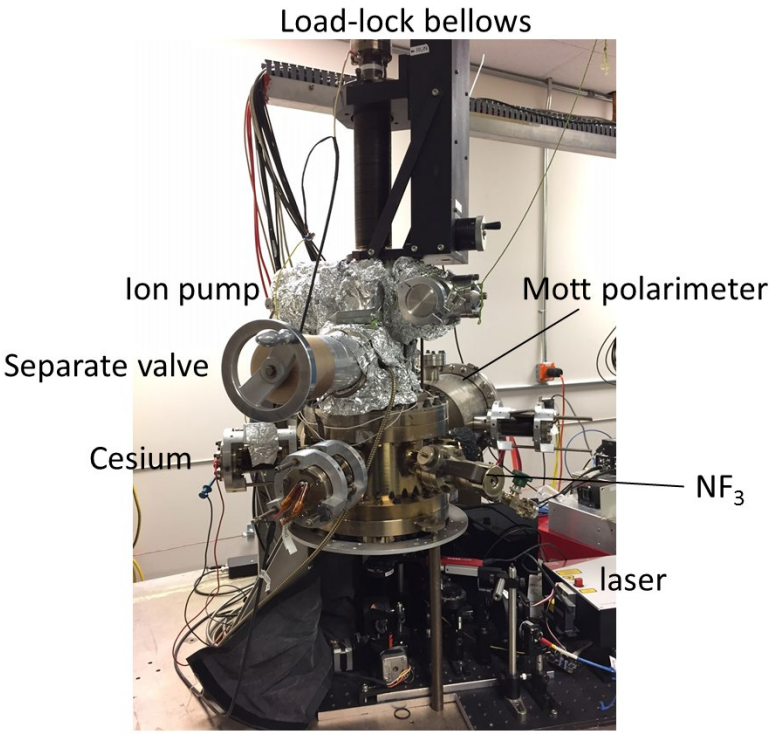

Figure 3-6: A photograph of mini-Mott chamber

3.1.2 Preparation for photocathode activation

Photocathode sample was cut into 15mm×15mm small pieces to put onto a 25mm diameter stalk endpoint surface on which there is a groove. Indium is used to solder the photocathode onto the stalk, which make the thermal conduction between the cathode and the stalk surface more enough and uniform. In addition, a tantalum cup is used to fix the cathode onto the stalk. Figure 3-7 shows the photocathode holder and photocathode sample on the holder.

Cesium and NF_3 are used to form NEA surface of the photocathode in our experiment. The NF_3 is introduced into the chamber by a leak valve from a reservoir tube in which we usually load 5 psi NF_3. The amount of the NF_3 is controlled by monitoring the total pressure within the chamber (usually $9 \times 10^{-10} - 1 \times 10^{-9}$ torr).

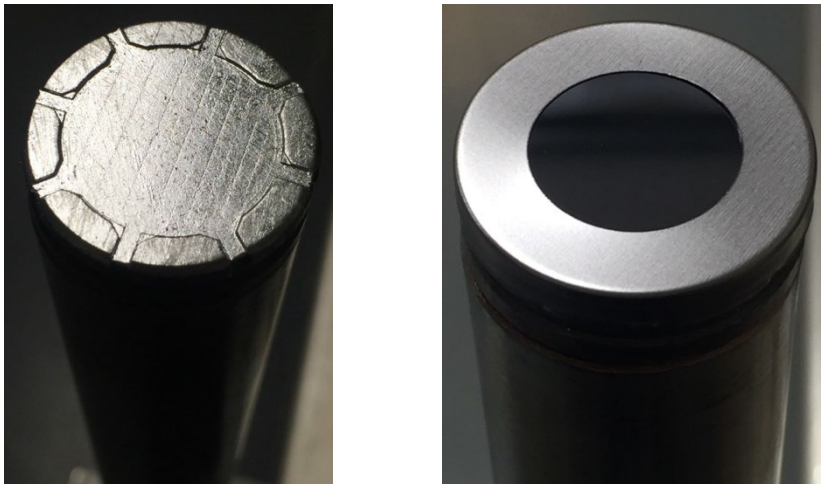

Figure 3-7: Photocathode holder (stalk) and photocathode sample on the holder

The cesium atoms are provided by a SEAS Alkali Metal Dispenser (AMD): cesium dispenser. The release of cesium for a dispenser is dependent on time and temperature. In our experiment, we control the release of cesium by the amount of current passed through the dispenser. Figure 3-8 (a) shows a cesium dispenser and (b) shows the curves between the cesium pressure in the chamber and the current for the cesium dispenser, the pressure is measured by RGA. The cesium evaporates at the temperature between 550°C and 850°C which responds to the current between 4A and 7.5A. We keep the cesium pressure around 2-3×10-13 Torr in our activation experiment. As using the Cs dispenser, its yield will decay, which lead to the released Cs into the chamber (Cs pressure) will decrease at the same current passed through the dispenser. Thus, the current value used in photocathode activation is increasing with the usage time of the dispenser.

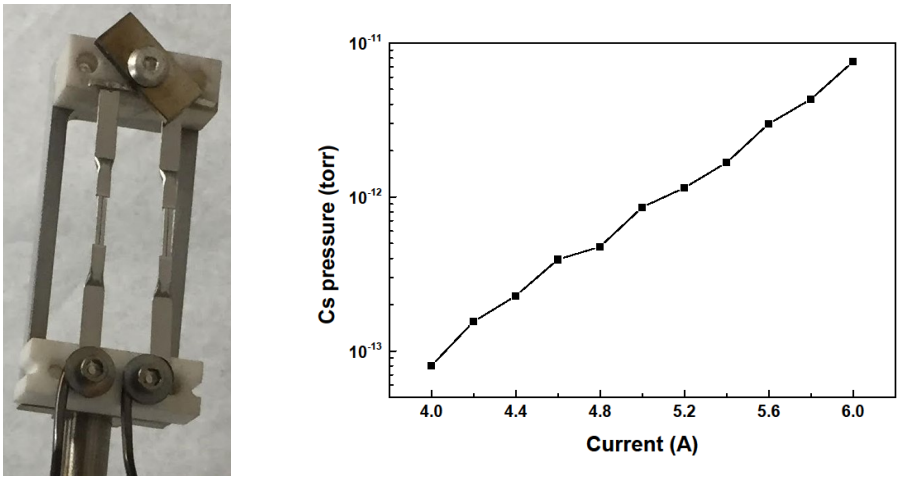

Figure 3-8: (left) SEAS Cesium Dispenser; (right) Pressure/current curves for a new cesium dispenser, the pressure is decreasing with the usage time due to the yield decay.

To drive GaAs, a laser source with continuous optional wavelength from 400nm to 850nm is used for our experiments. The laser source composed with a “SuperK EXTREME-High Power Supercotinuum White Light Laser” and a “SuperK VARIA-Variable Bandpass Filter”. The SuperK

EXTREME generate white light with continuous wavelength, the SuperK VARIA filter the white light come from the SuperK EXTREME and output a laser light with defined wavelength (from 400 nm to 850 nm) and bandwidth. In the experiment, the bandwidth is set to be 1 nm, and the power of the laser is usually set at microwatt scale. The laser D4σ is 1.041mm to 1.120 mm (the laser spot is shown in Figure 3-9).

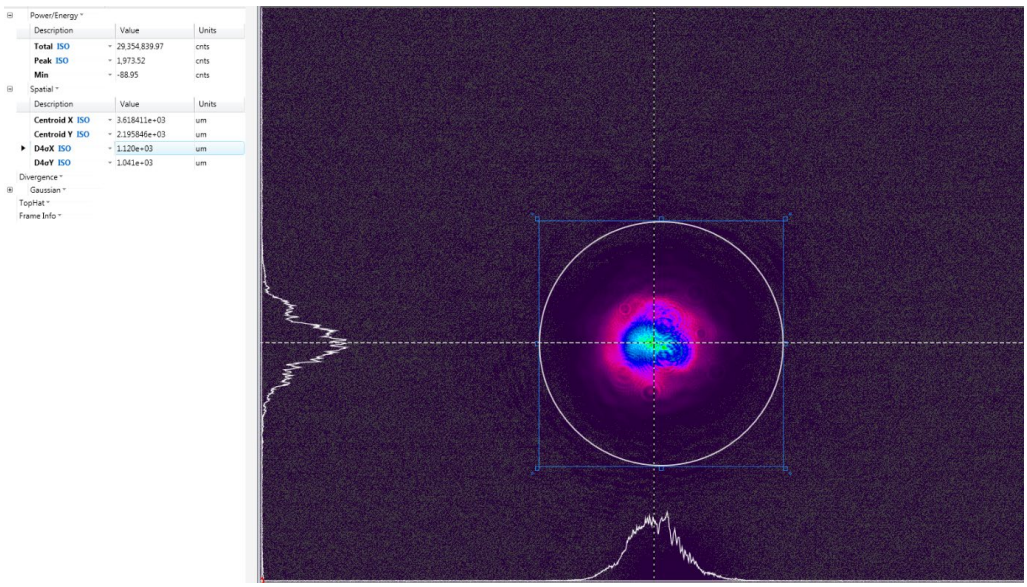

Figure 3-9: laser spot illuminate on the cathode for 500nm

The performance of GaAs photocathodes strongly depends on the surface condition, so the surface clean is needed to remove the contaminants like cesium, oxide, fluorine and carbon, etc. There are two methods to clean the surface to achieve a surface free of Cs-F and any other contaminants. One is heat the cathode to high temperature (Bulk GaAs: 550°C; Super-lattice GaAs: 500°C) for about 1 hours. Another method is atomic hydrogen cleaning which was done at a lower temperature of 300°C for about 45 minutes. Following the atomic hydrogen cleaning cycle, the sample need to be heated to 450°C for about 30 minutes to remove bound and adsorbed hydrogen. [139,140] The high temperature heat cleaning is much more convenient than atomic hydrogen cleaning, which also need less time to recover to the ultra-high vacuum after cleaning than atomic hydrogen cleaning. So, in our experiment, we almost use high temperature heat cleaning method. For the bulk GaAs, the crystal lattice would be damaged when the temperature is higher than 620°C. It's very necessary to control the temperature accurately. We use a stalk heater to heat the cathode, reading the temperature of heater by a thermal couple on the heater. The calibration of the temperature between cathodes and heater is measured. For bulk GaAs: $T_{cathode} = 0.81T_{heater} + 3.8\ °C$; For super-lattice GaAs: $T_{cathode} = 0.79T_{heater} + 4.2\ °C$.

In order to know how the activation layer changes with the heating temperature, the QE decay and vacuum pressure increase with heating temperature is measured when heat clean the bulk GaAs (shown in Figure 3-10). QE comes to decay when the temperature is higher than 40°C, due to the structure of Cs-F layer is to be damaged. The vacuum pressure comes to increase quickly when temperature reach

to 300°C. At this temperature, the structure of Cs-F layer is totally damaged, and the atoms begin to be removed from the cathode surface, i.e., the NEA surface disappear, and the surface potential barrier is too high to prevent electrons to emit, thus the QE almost become to 0.

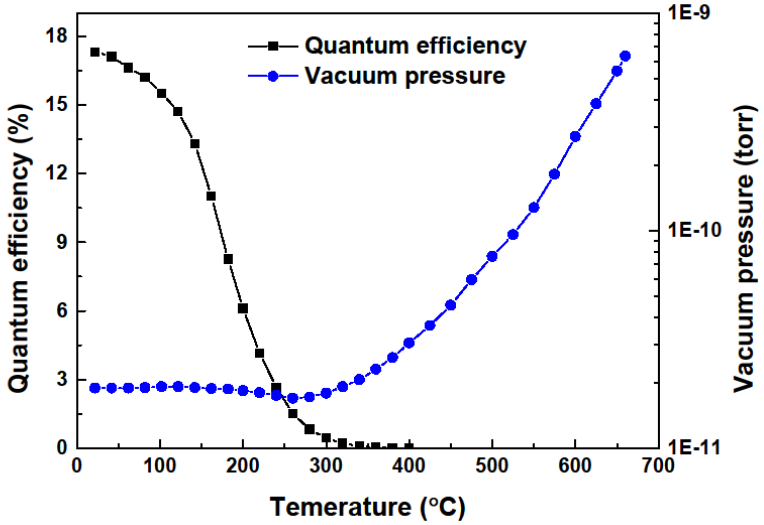

Figure 3-10: Quantum Efficiency decay and vacuum pressure increase with the heating temperature (for the heater) when heat cleaning for bulk GaAs. The heating rate is 11°C/min

3.1.3 Photocathode activation process

The activation process, the way to obtain NEA surface on the GaAs photocathodes, is extremely important to optimize the performance of GaAs photocathodes which have been and continues to be the most important activity in the GaAs photocathode development. The formation of the NEA surface and the performance of GaAs photocathodes strongly depend on the activation process. Up-to-date, three different activation techniques can be used to form NEA surface on the GaAs photocathodes. First technique is the so-called yo-yo technique, [141,142] in which the Cs and F (or O) layers are alternately deposited onto the GaAs surface. The second technique is the so-called co-deposition technique, [100] in which the Cs layers are deposited continuously until the activation process is complete and the F (or O) layers are deposited periodically onto the GaAs surface. The third one is the so-called saturation technique, [143] in which the Cs and F (or O) layers are continuously deposited onto the GaAs surface.

1) The yo-yo technique

The yo-yo activation technique is performed by exposing GaAs photocathode surface to Cs and NF3 alternately. In this technique, the Cs atoms are firstly released from the dispenser into chamber and then deposited onto GaAs surface. The amount of Cs atoms is controlled by the current passed through the dispenser. During the activation, the GaAs photocathode is illuminated by the laser, and the generated photocurrent that is used as an indication of the amount of deposited Cs and F is recorded simultaneously. After a given amount of time, the photocurrent is generated and increases due to the

EA of GaAs lower by forming the electric dipole on the surface induced by the deposited Cs and As. The photocurrent evolution for yo-yo activation is shown in Figure 3-11.

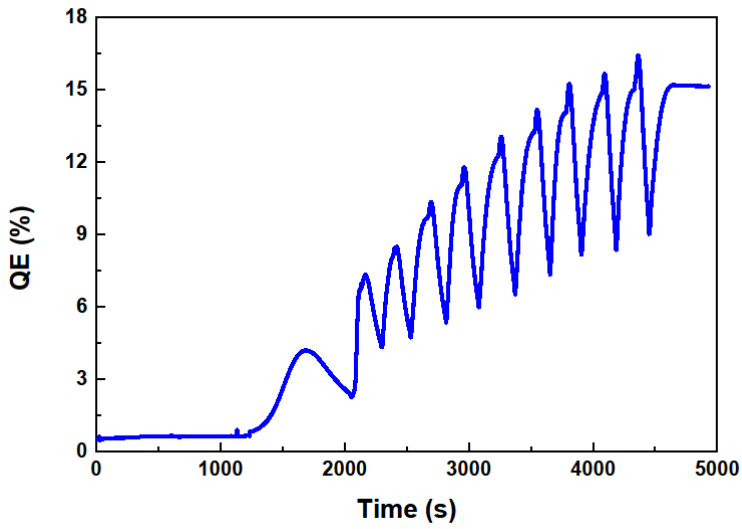

Figure 3-11: A typical plot of evolution of QE during the activation with yo-yo technique for GaAs (100) photocathode with 650 nm laser illuminating

As the deposition of Cs, the photocurrent increases to maximum value (1st peak) and then decreases. At the 1st peak position, all the deposited Cs is used to form electric dipole. As more Cs depositing, these excess Cs will accumulate on the surface and form Cs islands, which depolarize the electric dipole, and therefore increasing the EA of GaAs. So, the photocurrent begins to decrease after 1st peak. When the photocurrent drops to approximately 2/3-1/2 of the peak value, the Cs deposition is stopped and then NF_3 is immediately introduced into chamber through a leak valve. The amount of the NF_3 is controlled by controlling the total pressure within the chamber (usually $9 \times 10^{-10} - 1 \times 10^{-9}$ torr). As exposing to NF_3, fluorine deposits onto the surface by combining with Cs and forming Cs-F dipole that leads to the EA of GaAs decrease and therefore the photocurrent increases again. The increasing rate of the photocurrent depends on the pressure of NF_3within the chamber. After the photocurrent reaches its peak again, the NF_3 exposing is stopped and then immediately deposit Cs again. Now, the 1st yo-yo cycle is done.

After that the Cs is repeatedly deposited at each peak and NF_3 is repeatedly deposited at each valley, and the photocurrent increases from cycle to cycle. When the peak value increases no further, typically after 10-15 cycles, the activation process is complete. The maximum achievable photocurrent is the maximum photocurrent obtained from the photocathode. If the process is continued even further, the peak values decrease slowly, this is so-called over-activation.

In our yo-yo activation technique, the cesium is excess at each yo-yo cycle and then give oxidant (NF_3or O_2) to eliminate the excess cesium by forming electric dipole, which can be called yo-yo activation technique with excess cesium. Oppositely, we can let the oxidant excess at each cycle and

then give cesium to eliminate the excess oxidant by forming electric dipole, which can be called yo-yo activation technique with excess oxidant. In which the Cs starts to be deposit at each valley of photocurrent and stops at each peak of photocurrent, and the oxidant starts to be deposit at each peak of photocurrent and is stopped at each valley of photocurrent. Besides, there is another way to execute the yo-yo activation technique, which can be called yo-yo activation technique with excess cesium and excess oxidant alternately. Where the cesium is first deposited to make the photocurrent increase to peak then decrease to valley, at the time the cesium is stopped and oxidant starts to be deposit to make the photocurrent also increase to peak and then decrease to valley, i.e. the cesium and oxidant both start to be deposit at one valley of photocurrent and is stopped at the following valley of photocurrent.

No matter how to execute the yo-yo activation technique, their essentials are same - the cesium and oxidant is deposited onto photocathode surface alternately. The final QE obtained from three ways is no big difference if photocathodes were fully activated by the three ways under same condition. It is noted that we found the performance of photocathode will become worse if too much oxidant is deposited onto the photocathode surface. Thus, there is a need to control the oxidant carefully. Our suggestion is using the yo-yo activation technique with excess cesium to activate GaAs photocathodes.

2) The co-deposition technique

The co-deposition activation technique is performed by exposing GaAs photocathodes to Cs continuously and to NF_3 periodically. In this technique, the Cs is firstly deposited onto the photocathode surface in similar manner to the yo-yo technique. After a given time, the photocurrent is generated and increases to 1st peak then begins to decrease. When the photocurrent drops to approximately 2/3-1/2 of the peak value, NF_3 is immediately introduced into the chamber through the leak valve. In contrast to the yo-yo technique, the Cs deposition continues during NF_3 exposure and continues until the activation process is complete. As exposing to NF_3, the photocurrent increases again. Once the photocurrent reaches to its peak, NF_3 exposure is immediately stopped, leading to the photocurrent decrease again. Repeat this cycle until the peak value becomes steady, then stop Cs and NF_3 exposure.

Here we also make the Cs excess at each cycle. Same to yo-yo technique, the co-deposition technique can also be executed under the condition with excess oxidant or with excess Cs and excess oxidant alternately. No matter which way, their essential is same. The difference to the yo-yo technique is that the flux of oxidant should be higher to make sure there is more oxidant to accumulate on the photocathode surface. If the flux of oxidant is low, all the deposited F (or O) will combine with Cs to form electric dipole, which decreases the EA, and the photocurrent just only increase, no decrease occurs. It's worth noting that if the flux of oxidant is too low, there is no enough oxidant to combine with the deposited Cs, leading to Cs accumulating onto the photocathode surface and form Cs islands that decrease the QE, i.e., the activation process is not good, and the final QE is lower than best value.

Therefore, the flux of oxidant should be precisely controlled when using this technique to activate photocathodes.

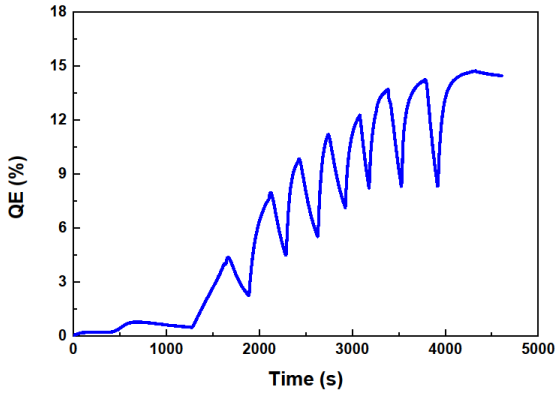

Figure 3-12: A typical plot of evolution of QE during the activation with co-deposition technique for GaAs (100) photocathode with 650 nm laser illuminating

3) The saturation technique

The saturation activation technique is performed by exposing GaAs photocathodes to Cs and NF3 continuously. In this technique, we also firstly release the Cs into the chamber in similar manner to the two techniques mentioned before. Once the photocurrent increases to 1st peak, the NF_3 is immediately introduced into the chamber through the leak valve. And then the Cs and NF_3 both continue until the photocurrent reaches to maximum value.

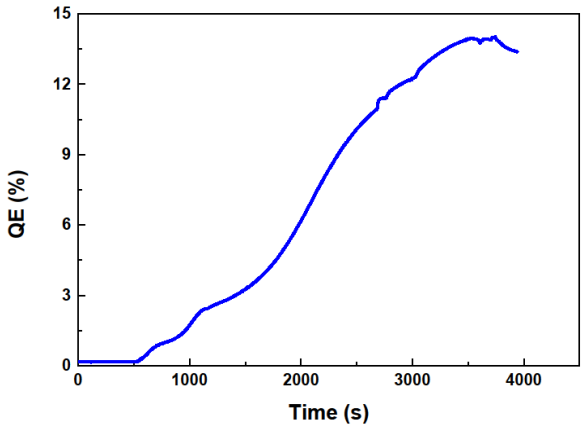

Figure 3-13: A typical plot of evolution of QE during the activation with saturation technique for GaAs (100) photocathode with 650 nm laser illuminating

Compared to other techniques, the saturation activation technique is very difficult to control. No matter which of the cesium and oxidant is excess than another one, the excess one will accumulate onto the surface and break the forming of electric dipole, leading to the final QE is lower than the best value. Thus, the speed of Cs release and the flux rate of oxidant must be carefully monitored and regulated throughout the activation process.

Comparing the three activation techniques, we found that the yo-yo activation technique takes time longer than other techniques, but it is easiest to be controlled and come true, and the maximum QE obtained from yo-yo activation is slightly higher than others because the fraction of Cs and F can be matched better during yo-yo activation process. The performance of saturation activation technique is opposite to the yo-yo activation technique. So, in our experiments, we apply the yo-yo technique to activate our photocathodes.

3.1.4 QE decay and re-activation

The QE decay of photocathode depends on cathode material, vacuum pressure, residual gas component, operational photocurrent, and ion bombardment, etc. The dark lifetime (no laser illuminate) is far higher than the operational lifetime. The dark lifetime for the GaAs photocathode mainly depends on the residual gas component and their pressure in the chamber. The commonly residual gas existed in the chamber are H_2, N_2, CO, CO_2, H_2O, CH_4, O_2, NF_3 etc. H_2, CH4 and N_2have no effect on the QE decay, and CO, CO_2, H_2O, O_2, NF_3 (all the oxidant) have the ability to reduce the QE, in which O_2 has the biggest effect on the QE decrease. [144,145] In our chamber, the vacuum pressure is very low ($\sim 10^{-11}\ torr$), and H_2 is main residual gas (>75%), the oxidant gas is very few (as shown in Table 3-1). The QE in our two chambers can last some weeks even to months without laser illuminating.

The decay of photocurrent (QE decay) for GaAs (100) photocathodes was measured in two chambers at 77K and 300K and is shown in Figure 3-14. The photocathodes were illuminated with low power laser to provide the initial photocurrent at μA level. The QE decay in H1 chamber is faster than that in mini-Mott chamber, and the decay at low temperature (77 K) is faster than that at room temperature (300 K). The 1/e lifetime is list as follows: 300 K in mini-Mott chamber: 69.2 hours, 300 K in H1 chamber: 42.5 hours, 77 K in mini-Mott chamber: 13 hours, and 77 K in mini-Mott chamber: 0.82 hours. The 1/e lifetime strongly depends on the temperature. The 1/e lifetime also depends on the operating photocurrent that is different for our lifetime test. Higher operating photocurrent leads to lower 1/e lifetime. To estimate the lifetime more effectively, the charge lifetime is given as follows: 300 K in mini-Mott chamber: 239 mC, 300 K in H1 chamber: 246 mC, 77 K in mini-Mott chamber: 63 mC, and 77 K in H1 chamber: 3.88 mC.

There are two main mechanisms that were identified as potential causes for the decrease of QE when photocathode is in operating to provide photocurrent: one is thermal heating and another one is ion bombardment. The thermal heating causes the Cs-F layer degrading, which makes the QE decrease. The ion bombardment reduces the QE by ion implanting into photocathode and damaging photocathode structure, [81] and by degrading Cs-F layer. A way was proposed to prolong the lifetime by adding additional cesium to the photocathode surface after normal activation. [146] The QE of the overcesiated photocathode will firstly increase due to the Cs was firstly removed leaving a better matched Cs/F on the surface, and then the QE slowly drops because of the evaporation of Cs-F layer. Thus, exposure the activated photocathode to the cesium during the photocathode in operating can be proposed to prolong

the lifetime due to the excessive forms a protective layer on the surface, which separates harmful gases from the Cs-F layer and prevents the Cs-F layer from evaporating. [147]

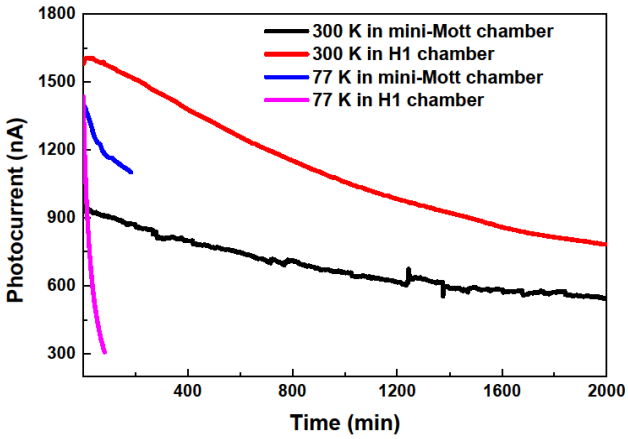

Figure 3-14: The decay of photocurrent for GaAs (100) photocathode in two chambers at different temperature

It is also worth noting that the lifetime of GaAs photocathodes can be greatly improved by introducing Li in the Cs/ NF_3 activation process due to the immunity of GaAs photocathode from contaminants can be enhanced by this way. [148] After adding Li to the Cs/ NF_3 activation process, the Li will interact with NF_x to form $Li^+ - NF_x$, which become more stable. And the interaction between Li and NF_x leads to NF_x take a F-on-top orientation and shifts the charge away from F atoms, which further attracts charge from Cs atoms on the top of the activation layer. The resulting positively charged Cs atoms on the top of activation layer can reduce the sticking coefficient of contaminants from the surrounding environment, because the metallic Cs is a good getter material, but charged Cs is not. Therefore, the more stable activation layer and the reduction of contaminants adsorption improved the lifetime of the Cs + Li + NF_3 activated photocathodes. [149]

The reduced QE can be recovered by re-activation. It is believed that the main reason to decrease of QE is the loss of Cs and oxidant. The loss rate of Cs is faster than that of oxidant, leaving the mismatch between Cs and oxidant. Thus, the photocathode can be re-activated by introduce Cs onto the surface. By this way, a high fraction of the QE can be recovered. Continue give Cs and oxidant can get more QE, but the QE obtained by re-activation is usually lower than before. To obtain the initial high QE, the photocathode should be cleaned by heating to high temperature, and then activate again.

3.1.5 Measurement and analysis of polarization

The apparatus (mini-Mott chamber) for measuring the ESP of photocathodes consists of a light system, a low-voltage electron source chamber, a beam transport line and a Mott polarimeter. The schematic of the experimental apparatus is shown in Figure 3-15. The light system provided a left-handed (or right-handed) circularly polarized light, which includes a shutter, polarizer, reflect mirror, half-wave plate and quarter-wave plate. A beam of driven light first passed through the polarizer to

obtain linearly polarized light, and then be transformed to circularly polarized light by the quarter-wave plate. The circularly polarized orientation of light was controlled by plugging in or drawing out the half-wave plate.

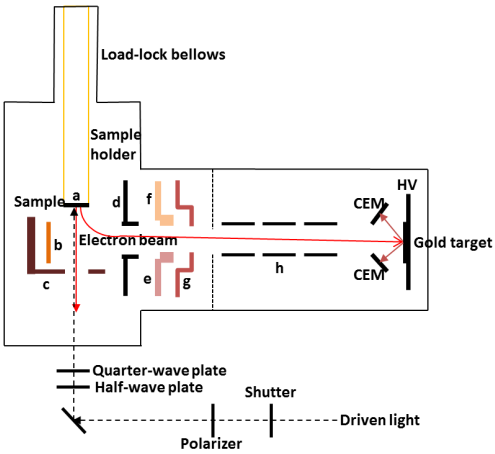

Figure 3-15: Schematic of experimental apparatus for measuring ESP of photocathodes: light system, electron source chamber, electron transport line, Mott polarimeter

The circularly polarized light illuminated onto the photocathode in the electron source chamber, producing longitudinally polarized electron beam. The longitudinally polarized electron beam was bent 90° by electrostatic bend (elements b and c) [150], forming transversely polarized electron beam required to be detected by Mott polarimeter. And then the transversely polarized electron beam was focus and steered using one split lens (element f and e), two cylindrical lenses (element d and g) [150] and three electrostatic tube lenses (element h) [151] to the gold target of the Mott polarimeter. The number of electrons reached to the target can be monitored by a picoammeter. Only a part of electrons can be bent and transported to the target. The fraction of electrons transported to the target was defined as transmission of the transport line (usually about 10% for our apparatus). Adjusting the voltage of the transport lenses helps to find a best transmission that is helpful to data collection and analysis.

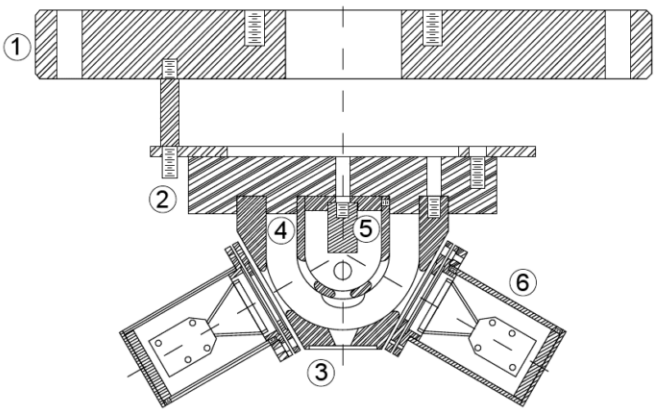

Figure 3-16: The cross section drawing of Mott polarimeter: 1) 8'' Conflat flange with 2.75'' flange for high-voltage bushings and feedthroughs; 2) insulating standoff and mounting plate; 3) outer hemisphere; 4) high polished stainless steel inner hemisphere; 5) target screwed into high voltage electrode; 6) channel electron multiplier (CEM) in housing attached to retarding field grid assembly

The cross section drawing of Mott polarimeter is shown in Figure 3-16. [152] Electrons entered the polarimeter were accelerated to energies from 5 to 50 keV (usually set to 20 keV) between two hemispherical stainless steel electrodes (element 3 and 4 in Figure 3-16) supported on a ceramic insulator. To reduce the chance of electrical discharge, the outer surface of the inner hemisphere was highly polished, and aperture holes in both hemispheres are rounded and polished. Electrons scattered from a gold target (5 μm of gold plated on a copper cylinder) inside the inner hemisphere. Scattered electrons decelerated in the gap between the inner and outer hemispherical electrodes and were detected with two channel electron multipliers (CEMs from Dr. Sjuts Optotechnik GmbH), each subtending 0.27 sr, centered at 120°. Two gold mesh grids in front of each CEM, separated by 3.5 mm, established a spatially well-defined retarding potential volume and rejected inelastically-scattered electrons. Grids were affixed to aluminum support rings using Aerodag (from Acheson Industries) and isolated by ruby balls. As the retarding field increased negatively from ground, electrons that lost energy through inelastic scattering were increasingly excluded from the measurement, and when the retarding potential energy approached that of the incident beam kinetic energy, only the elastically scattered electrons were detected.

After activating the photocathode, the ESP measurement can be performed. The procedure of ESP measurement is list as follows:

1) Bias the target at 300 V and measure the photocurrent reached to the target with a picoammeter, which used to compare to the photocurrent produced by the photocathode to determine the transmission of the transport. Adjusting the transport lens (element b-h in Figure 3-15) to obtain a best transmission (usually about 10%) of the transport line
2) After obtaining a best transmission, Bias the target at 20 kV and the CEMs at 2 to 3 kV that determined by the detection rate. Setting the retarding voltage on the mesh grids to 150 V
3) Close the shutter, measure the counts on the CEMs for the dark signal.
4) Open the shutter and keep the half-wave plate out of the laser transport line, measure the counts on the CEMs (L1, R1)
5) Keep opening the shutter and plug in the half-wave plate to flip the polarization of laser, measure the counts on the CEMs (L2, R2)
6) Repeat steps 4 and 5 two times and then repeat step 3
7) Increase the retarding voltage on the mesh grids to 160, 170, 180 … 350V one by one, repeat steps 3 to 6 at each voltage
8) Change the wavelength of laser and repeat steps 3 to 7 to measure the polarization at different wavelength

During the measurement, the shutter, half-wave plate, and retarding field, laser machine and picoammeter were all controlled by a computerized data acquisition program, written in NI LabVIEW, which also records the counts for the CEMs and wavelength of laser. An optical attenuator system was

used to vary the laser power, and subsequently the photocurrent, which also was controlled by the computerized program to keep the photocurrent same.

The measured scattering asymmetry at each retarding field can be calculated from equation 3-6 and given by $A = \frac{N_+ - N_-}{N_+ + N_-}$, with $N_+ = \sqrt{\bar{L}_1 \bar{R}_2}$ and $N_- = \sqrt{\bar{L}_2 \bar{R}_1}$, in which $\bar{L}_1, \bar{L}_2 \bar{R}_1, \bar{R}_2$ are the average value for the counts on the CEMs at each retarding field. The scattering asymmetry was measured from 150 V to 350 V of the retarding voltage, thus there should have 21 values of scattering asymmetry. However, when the retarding voltage is bigger than 268 V, only the elastically scattered electrons were detected. Thus, only the values from 150 V to 260 V are effective. These values before 11th one are averaged as the final scattering asymmetry $\bar{A}$. After obtaining the scattering asymmetry $\bar{A}$, the ESP of photocathode can be calculated by $P = \bar{A}/S_{eff}$.

The effective Sherman function, S_{eff}, was estimated by generating electron beam from photocathode material with known polarization which is identical to the CEBAF polarized source [153]. The effective Sherman function depends on the target bias voltage and its value for 20 kV of the target bias voltage is 2.01.

The ESP of photocathode obtained from the method is based on assuming that the polarization of laser light is 100%. In practical, the polarization of laser light is smaller than 100%, which depends on the polarizer, quarter (and half)-wave plate, and the laser wavelength. The polarization of laser light (P_l) passed through our light system is shown in Figure 3-17 as a function of light wavelength. Thus, the real ESP of photocathode should be written by $P = \bar{A}/(P_l \cdot S_{eff})$.

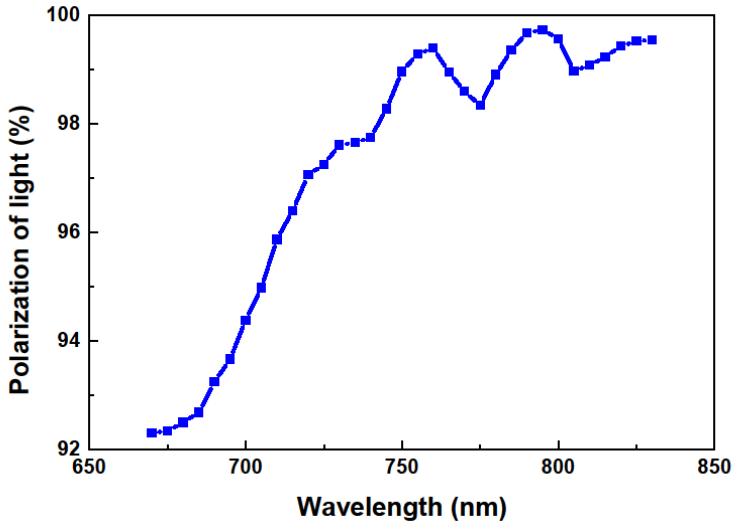

Figure 3-17: The polarization of light passed through the polarizer and quarter (and half)-wave plate

3.2 Ion Bombardment

DC high voltage photoguns with GaAs photocathodes are used to generate spin-polarized electron beams for nuclear and particle physics research. [154] More recently, these photoguns have found application in material science where spin-polarized electron beams can be used for magnetization-sensitive imaging. [155] DC high voltage photoguns with alkali-antimonide photocathodes [71,156] or GaAs [157,158] are also used to produce bright electron beams for accelerator-based light sources. Ion back-bombardment represents the dominant lifetime-limiting mechanism of modern DC high voltage photoguns. [22,23] This section studies how the ion bombardment decreases the QE of GaAs photocathode.

3.2.1 Theory

Ion back-bombardment is the process whereby residual gas within the cathode/anode gap is ionized by the extracted electron beam and attracted to the negatively-biased photocathode. Photogun experts speculate that ions strike the photocathode surface sputtering away the chemicals used to create a negative electron affinity (NEA) condition, or they become implanted within the photocathode material knocking out atoms from the crystal structure and altering the energy band structure, or they serve as interstitial defects that reduce the electron diffusion length. All these possibilities are problematic because the net result is reduced photocathode yield, or quantum efficiency (QE), which results in reduced operating lifetime of the photogun. Improving the vacuum within the photogun is the best way to reduce ion back-bombardment and thereby prolong the operating lifetime of the photogun, but modern DC high voltage photoguns are already operating in the 10^{-11} Torr pressure range, or lower, so improving the photogun vacuum further is thus very challenging.

In this study, we explored the sensitivity of bulk GaAs photocathodes with (100), (110) and (111A) surface cleave planes to ion bombardment at hydrogen-ion energies of 100 and 10,000 V. Tests were performed using an ultrahigh vacuum chamber where GaAs photocathodes were created in the usual manner, with the photocathode biased at low voltage and with the surface work function reduced by applying cesium and NF_3 to create a NEA condition. After verifying that each sample provided high QE at 532 nm, the NEA layer was removed. Then samples were implanted with hydrogen ions from an atomic hydrogen source, originally used to clean photocathodes, [139,159,160] but used here as an ion source. The energy of the implanted ions was determined by the value of the negative bias applied to the photocathode (more details provided below). Samples were then heated and re-activated – i.e., chemicals were reapplied to the GaAs surface to recreate the NEA condition. Repeated heating and activation using different heating protocols (temperature and duration) provided a means to evaluate a sample's sensitivity to ion bombardment. A central motivation of this study was to determine the susceptibility of each cleave plane to ion damage, and to what extent ion channeling [161,162] plays a role in QE reduction. We sought to test if enhanced ion channeling would serve to deliver ions deeper into the photocathode material, beyond the region near the surface of the photocathode where the photo-

emitted electrons originate. Enhanced ion channeling could benefit a photogun, minimizing the ill-effects of ion bombardment and prolonging the photogun operating lifetime.

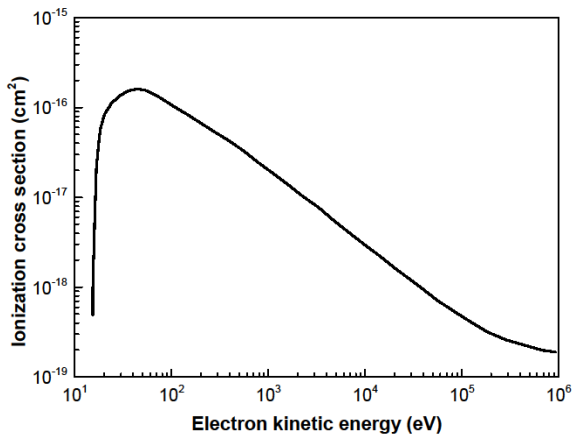

Figure 3-18: Electron impact ionization cross section for hydrogen molecules - the dominant gas species inside modern DC high voltage photoguns - as a function of electron kinetic energy.

To understand ion back-bombardment inside a photogun, it is important to note that the energy spectrum of the extracted photoemitted electron beam within the cathode/anode gap is broad, with electrons leaving the cathode electrode at zero velocity, and then gaining energy until reaching the anode. For a typical DC high voltage photogun, the photocathode is biased at voltages between -100 and -350 kV. Hydrogen is the dominant gas species inside a modern photogun, and the peak ionization cross section occurs at ~ 100 V and drops by more than two orders of magnitude at 100 kV [23,163] (Figure 3-18). So under typical photogun operation, the surface of the photocathode is bombarded by significantly more low energy ions than high energy ions. Determining the sensitivity of photocathode QE to ion energy represents another key motivation of this study.

Since the late 1960s, [97,164] GaAs has been extensively studied for its properties as an effective photo-emitter. James et al., [102] working with vacuum-cleaved samples, reported that (100) and (110) surfaces - with equal amounts of Ga and As atoms at the surface – provide similar QE as a function of the illumination wavelength (i.e., QE spectral response), whereas the (111A) surface comprised of only Ga atoms has the lowest QE and the (111B) surface comprised of only As atoms has the highest QE. Today it is a trivial matter to purchase high quality GaAs samples with the desired cleave plane surface. For this work, 3" diameter bulk GaAs wafers were purchased from a commercial vendor with (100), (110) and (111A) surface cleave planes. All samples were p-doped with Zn at nominal concentration $\sim 1 \times 10^{19}$ atoms/cm3. Other characteristics are provided in Table 3-2. No chemical preparation was performed on samples prior to installation in the vacuum test chamber. They were cleaved into 15 x 15 mm squares and attached to a sample holder, described below. This work also serves to assess which cleave plane surface provides the highest QE using commercially available material and modern vacuum hardware and techniques.

Table 3-2: The specifications of three bulk GaAs samples with different surface cleave planes.

	(100)	*(110)*	*(111A)*
Dopant	GaAs-Zn	GaAs-Zn	GaAs-Zn
Orientation	(100) ±0.5°	(110) ±0.5°	(111A) ±0.5°
Carrier concentration (a./c.c.)	1.0~1.3E19	1.3~1.4E19	1.1~1.14E19
Resistivity (ohm.cm)	6.6~7.7E-3	6.1~6.6E-3	7.17~7.38E-3
Mobility (cm2/v.s.)	74~80	71~74	77~78
Thickness (μm)	600~650	475~525	500~550

Whereas ion implantation in the form of ion back-bombardment is detrimental to the photocathode inside a DC high voltage photogun, ion implantation is beneficial and widely used in the fabrication of integrated circuits. As a result, implantation has been extensively studied. [165] The nuclei and the electrons within a crystallographic plane repel a positively charged ion like the hydrogen ions used in this experiment. As a result, positively charged particles tend to follow the direction between two neighboring crystal planes. This process - called channeling - leads to deeper penetration of the positive ions in the material. Channeling is more pronounced at higher ion energies. Figure 2-6 shows the relative spacing of atoms in the GaAs crystal structure for the three surface-cleave planes studied, viewed at normal incidence. The red boxes in Figure 2 denote the recurring geometric cells used for calculating the atomic number density which is a measure of the "open space" between atoms. The atomic number densities for the (100), (110) and (111A) GaAs cleave planes were calculated to be $8/a^2$, $4\sqrt{2}/a^2$, and $4\sqrt{3}/a^2$, respectively, where a is the GaAs lattice constant (5.6535 Å). We reasoned channeling would be enhanced for the (110) cleave plane which possesses the smallest atomic number density (i.e., the most open space between atoms), and that the (110) surface cleave plane would therefore be the most insensitive to ion bombardment.

Although the software program SRIM (Stopping Range of Ions in Matter) [166] does not take into account the crystal orientation of the GaAs photocathode, and thus does not describe channeling, the program was used to estimate the penetration depth of the hydrogen ions into the material and the number of vacancies created within the material when ions collide with gallium and arsenic atoms and knock them out of their positions within the crystal lattice. In the simulation, the hydrogen ions were injected into GaAs at normal incidence and the ion injection energy was varied from 100 to 10,000 V while keeping the ion dose constant for each simulation. The stopping depth of implanted hydrogen ions and the distribution of knock-out vacancies for different ion energies are shown in Figure 3-19. Unsurprisingly, higher energy ions penetrate deeper into the material and do more damage to the crystal structure compared to lower energy ions. The penetration depth (defined as the depth at which the dose falls to 1/e of its original value) is 69 Å and 1690 Å for 100 V and 10,000 V hydrogen ions, respectively, while gallium and arsenic atoms begin to be knocked out from their lattice positions at ion energies

greater than ~500 V. Laser light at 532 nm will be absorbed within 1300 ~ 1480 Å of the surface [115,116,167] and we note the diffusion length of electrons in GaAs is of the order 10,000-40,000Å. [168,169] Because these dimensions are comparable to the distance scales described in Figure 3-19 for implantation and knock-out vacancies, we hoped that our QE measurements would be sensitive to different ill-effects that might result from low and high energy ions at 100 and 10,000 V.

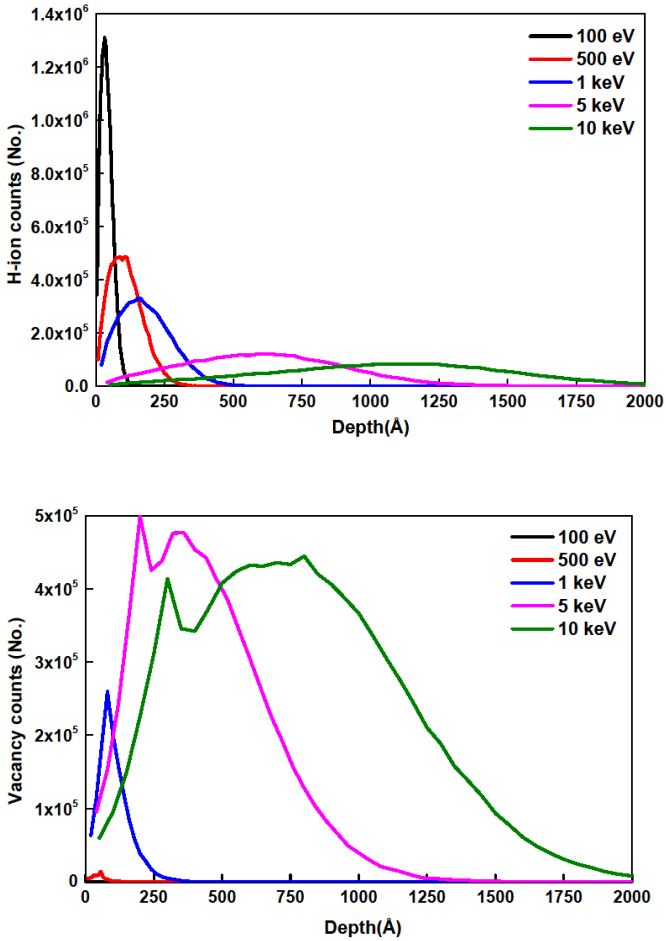

Figure 3-19: (up) Hydrogen ion distribution and (down) vacancy distribution within GaAs for different hydrogen ion energies. All simulations preformed using the same hydrogen ion dose of $\mathbf{8.1 \times 10^5}\ \boldsymbol{nA \cdot s}$. Plots obtained using SRIM.

3.2.2 Apparatus and Experiment

The experiment followed a sequence of steps. A photocathode sample was attached to a long tubular sample holder and installed in the vacuum test chamber which was then baked to achieve ultrahigh vacuum. Afterwards, the sample was heated to 550°C for 1 hour and allowed to cool. A photocathode was manufactured by applying cesium and NF_3 to the surface using a standard "yo-yo" activation protocol and afterwards the QE was mapped using a low power green laser beam that could be scanned across the photocathode surface. The sample was then biased at either 100 or 10,000 V and exposed to hydrogen ions of a prescribed dose. Finally, the sample was heated and re-activated multiple times to observe QE evolution. Additional specific details are provided below.

Square-shaped photocathode samples were cleaved to appropriate dimension (15 x 15 mm) using a diamond tipped scribe and secured to a molybdenum disc at the end of a tubular holder using indium foil and a tantalum cap with 13 mm diameter cutout in the center. During installation of the photocathode sample, care was taken to limit the amount of water vapor introduced into the apparatus (Figure 3-1) by applying a vigorous flow of clean dry nitrogen through the vacuum pump cart. After tightening the sample holder Conflat flange, the flow of nitrogen through the apparatus was halted and the chamber was evacuated using a turbo pump. When pressure within the chamber reached $\sim 10^{-6}$ Torr, electrical current was applied to the substrate of the non-evaporable getter pumps to liberate adsorbed gas, and the ion pump was energized. A pre-bake leak check was performed using a residual gas analyzer and oven panels were erected around the chamber which was then baked at 200 °C for 36 hours. Following the bakeout, the pressure within the chamber reached 10^{-11} Torr.

A heat cycle always immediately preceded photocathode activation. The photocathode was heated to 550 °C for 1 hour before the first activation, and at different temperatures and durations for activations following ion implantation. Heat liberates loosely bound gas at the photocathode surface, and it liberates hydrogen atoms and molecules that penetrate the photocathode surface during the ion implantation phase of the experiment. After the sample was cooled to room temperature, cesium and NF_3 were applied to reduce the surface work function. The sample was biased at – 250 V and illuminated with a white light source. A "yo-yo" activation protocol was employed - cesium was applied until photocurrent reached a peak and then decayed to approximately half the maximum value. At this point, the cesium source was turned off and a leak valve was opened to introduce NF_3 into the apparatus. Photocurrent was observed to increase to a new peak value. The NF_3 leak valve was then closed, and additional cesium was added, which caused the photocurrent to decrease. When photocurrent decreased to approximately half the new maximum value, the cesium source was de-energized and more NF_3 applied, each time providing more photocurrent than the previous cycle. This so-called "yo-yo" procedure was repeated approximately 12 times until the new peak current was within ~ 3% of the previous cycle maximum. With photocathode activation complete, the photocathode QE was mapped by a scanning focused laser beam at 532 nm. Because vacuum conditions inside the apparatus were very good, the "lifetime" of the photocathode was very long, and photocathode QE remained stable during the QE x-y scan and for many hours afterwards.

The hydrogen ion source is based on work in ref. 170. Commercial research-grade molecular hydrogen flows through a leak valve into a Pyrex glass dissociator (2.5 cm dia.). The molecular hydrogen was dissociated using an rf-inductive discharge created by a 12-turn coil 3.5 cm in diameter, which is part of an inductor-capacitor (LC) tuned circuit. The LC circuit resonated at ~ 100 MHz and the atomic fraction was maximized when the pressure inside the dissociator was 15 mTorr and the absorbed rf power exceeded 50 W. Gas exits the dissociator through a 1 mm dia. hole toward the photocathode sample approximately 10 cm away. A portion of the gas leaving the dissociator is ionized,

and these ions were directed at the sample by applying a negative bias to the sample holder which was electrically isolated from the grounded apparatus using a commercial ceramic break. During implantation, a valve was opened to a baked beamline leading to a turbo-molecular pump. This pumping scheme serves to maintain pressure near $\sim 1 \times 10^{-5}$ Torr to provide a mean free path for hydrogen of over 1 m.

As previously mentioned, two different hydrogen ion implantation energies were studied, 100 and 10,000 V. An picoammeter (as shown in Figure 3-20) in series with the photocathode bias-voltage power supply was used to continuously monitor the ion current at the sample, and the time integrated current represented the applied ion dose. A LabView program was used to monitor and integrate the real-time dose and the implantation was stopped when the dose reached about $8.1 \times 10^5\ nA \cdot s$, corresponding to a typical ion current of 900 nA and for an implantation duration of 15 minutes.

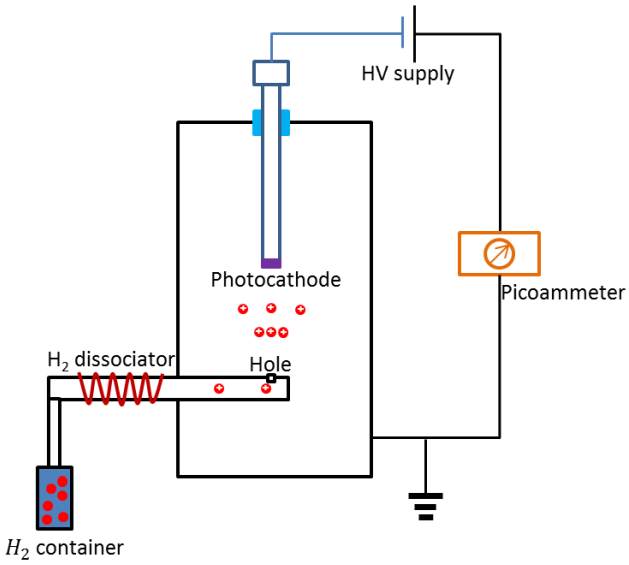

Figure 3-20: The schematic diagram for ion implantation

Hydrogen ions leave the source at relatively low energy (~eV) and travel in different directions. With no bias voltage applied to the sample, few ions reach the photocathode, as evidenced by the picoammeter which registers low current (<10% of current with bias voltage). But when the sample is biased at negative voltage, the ions are attracted to the sample (and the sample holder). The software program CST Studio Suite [171] was used to evaluate the electrostatic conditions of the apparatus and to estimate ion trajectories for the two bias voltages (see Figure 3-21). Although the number of ions emitted from the source and the duration of exposure were nominally identical for both energies, the dose at 100 V was approximately a factor of two smaller compared to 10,000 V trials because roughly half the ions struck the sample holder due to weaker electrostatic focusing. The applied dose per unit area was an additional factor of 10 smaller for the 100 V trials based on simple geometric considerations, namely 100 V ions illuminated the entire 13 mm diameter sample, whereas 10,000 V ions were focused

at the sample within a region ~4 mm diameter. There was no accounting for possible secondary electron emission from the sample at either energy.

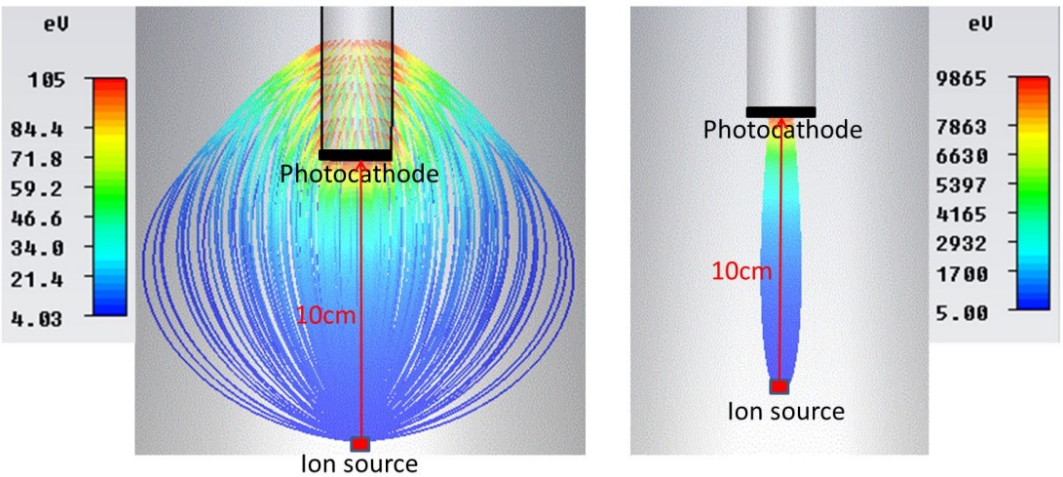

Figure 3-21: Ion trajectory from the hydrogen ion source to the photocathode sample when the photocathode sample is biased at 100 V (left) and 10,000 V (right). Ions exit the dissociator glassware from a 1 mm diameter hole located approximately 10 cm beneath the photocathode sample.

3.2.3 Results and Discussion

Prior to implantation, each photocathode sample was heated, cooled and activated. The QE was then measured as a function of laser wavelength and the results are presented in Figure 3-22. Quantum efficiency was calculated using the expression $QE = 124I/P\lambda$, where I is the measured photocurrent in μA, P is the laser power in mW, and λ is the wavelength of the laser light in nm. The cleave planes (100) and (110) provided the highest QE, approximately 21% at the laser wavelength 532 nm. Cleave plane sample (111A) provided the lowest QE, approximately 19% at 532 nm. Although these values are lower than reported in ref. 102, the relative trend between samples is consistent (i.e., $QE_{100} > QE_{110} > QE_{111A}$).

After determining that each sample provided high QE, samples were heated to 250 °C for 20 minutes to remove the activation layer of Cs and NF_3. Samples were then cooled to room temperature and implanted with hydrogen ions at the chosen energy and for the prescribed dose. The vacuum was allowed to recover overnight. Photocathode samples were then repeatedly heated and activated following different heating protocols (temperature and duration). Following each activation, the photocathode QE was measured at 532nm and compared to the pre-implantation value. In this manner, the sample's sensitivity to ion damage was evaluated. Figure 3-23 shows typical QE maps for samples implanted with 100 and 10,000 V hydrogen ions (the caption provides specific details of the cleave plane surface and heating protocol). For 100 V ions, QE degradation was uniformly distributed across the sample. But for 10,000 V hydrogen ions, the QE degradation was localized to a specific region of the sample, consistent with the electrostatic simulation that predicted a focused ion beam. Because the ion damage was displaced from the center of the photocathode, we assume the output hole of the hydrogen dissociator was misaligned relative to the photocathode sample. The misalignment was along

the left/right axis of the dissociator, which could not easily be corrected with existing vacuum hardware. The damage site location remained the same throughout the experiment, for each implantation and each sample.

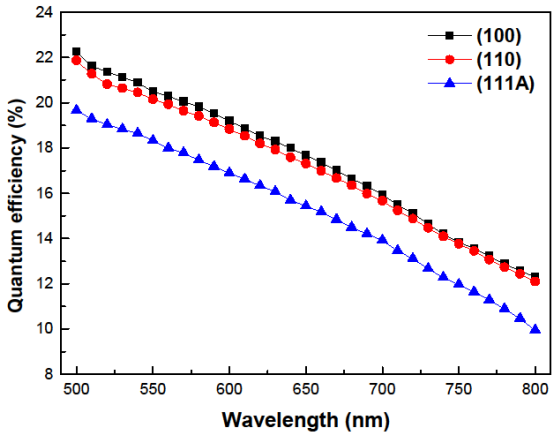

Figure 3-22: Photocathode QE versus laser wavelength for commercial bulk GaAs samples with different surface cleave planes, prior to ion implantation.

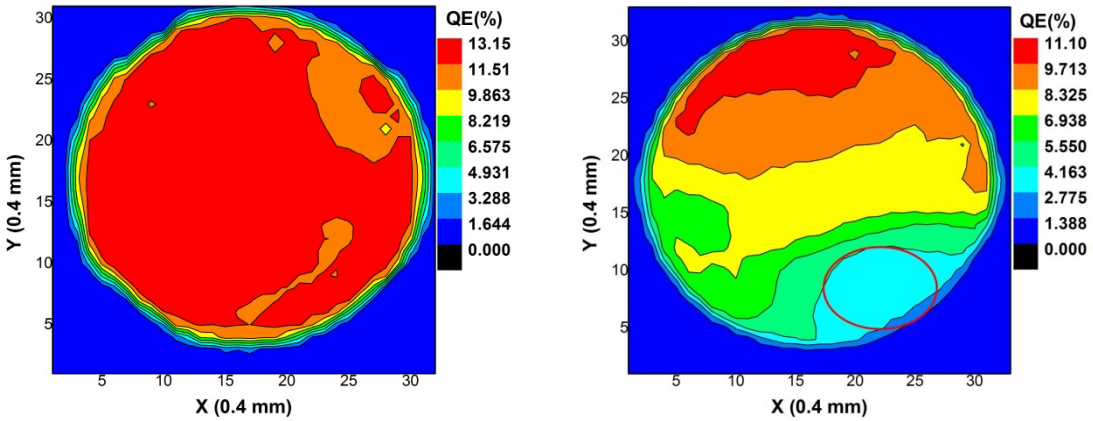

Figure 3-23: Typical QE maps of the photocathode obtained by scanning a focused low power green laser beam across the photocathode following activation. These maps show the bulk GaAs (111A) sample. Left: after the third activation following implantation with 100 V hydrogen ions. Right: after the third activation following implantation with 10,000 V hydrogen ions. The 2-dimensional plots help to illustrate ion implantation uniformity: 100 V hydrogen ions were uniformly distributed across the entire sample, but 10,000 V hydrogen ions were focused to a region denoted by the red circle, consistent with the particle tracking code simulations.

Figure 3-24 summarizes the results of the experiment, with QE at 532nm plotted as a function of repeated activation following a variety of heating protocols described within the caption, for samples implanted with 100 and 10,000 V hydrogen ions, and for samples that were not implanted with ions. When samples were repeatedly heated and activated – but not subjected to hydrogen ion implantation – the QE at 532 nm remained constant to within 5%. This speaks to the quality of the vacuum within the apparatus, which was dominated by chemically inert gas species like H_2, CH_4, CO and CO_2. The

QE of each sample did not degrade following repeated heating and activation, due to adverse chemical reactions that might take place under degraded vacuum conditions, especially when samples were hot.

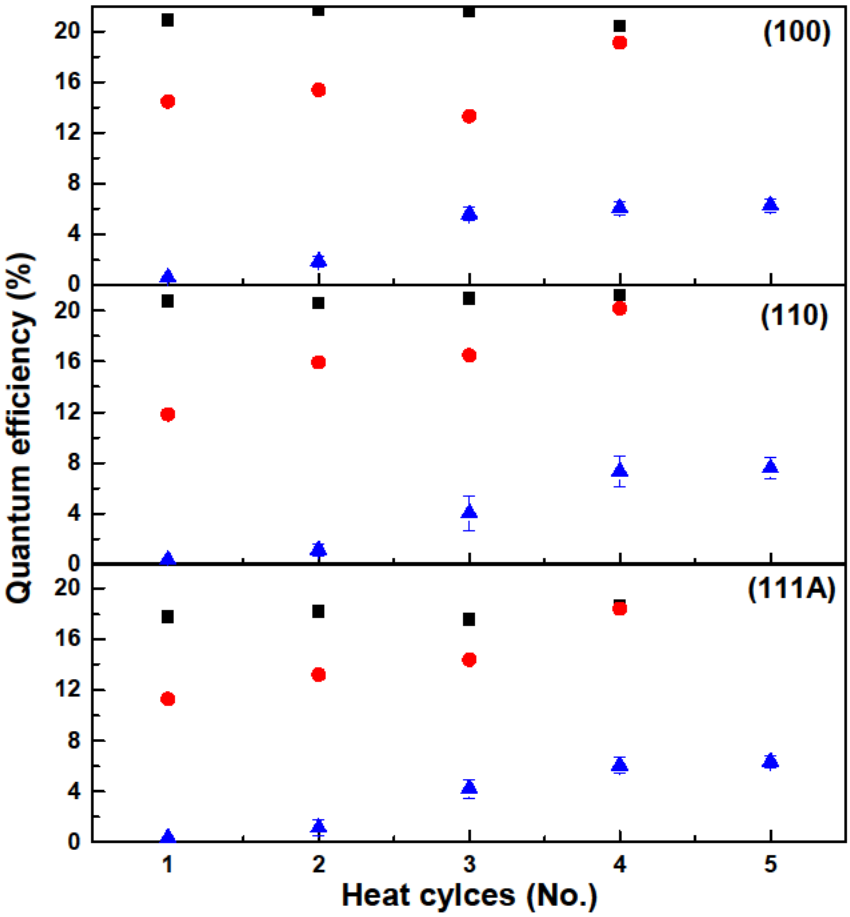

Figure 3-24: QE versus heat cycle for bulk GaAs with three different surface-cleave planes. Black Square: no implantation; Red Circle: implantation with 100 V hydrogen ions; Blue Triangle: implantation with 10,000 V hydrogen ions; Error bars represent the standard deviation in QE values averaged over the entire sample for "no implantation": and 100 V results, and over the small region denoted by the red circle in Figure 7 (right) for the 10,000 V results. Error bars are smaller than the data point symbols for "no implantation" and 100 V results because QE was very uniform across sample. Heat cycle number 1: 250°C for 20 minutes; 2: 370°C for 30 minutes; 3: 490°C for 1 hour; 4 and 5: 550°C for 1hour.

The next observation evident in Figure 3-24 is that both 100 and 10,000 V hydrogen ions served to degrade the sample QE, however the QE degradation associated with 10,000 V ions was significantly greater than that caused by 100 V ions. In general, for both ion energies, heating the sample to higher temperature and for longer time served to restore QE. For implantation with 100 V hydrogen ions, the QE could be completely restored by heating the sample. But for implantation with 10,000 V hydrogen ions, only a fraction of the QE could be restored. It should be noted that data points presented in Figure 3-24 were obtained by averaging the QE measurements over a specific region of the photocathode sample surface. For 100 V ion implantation, QE measurements were averaged over the entire sample. For the 10,000 V ions, QE values were averaged only in the region where the ions were focused, as indicated by the red circle shown in Figure 3-23 (right).

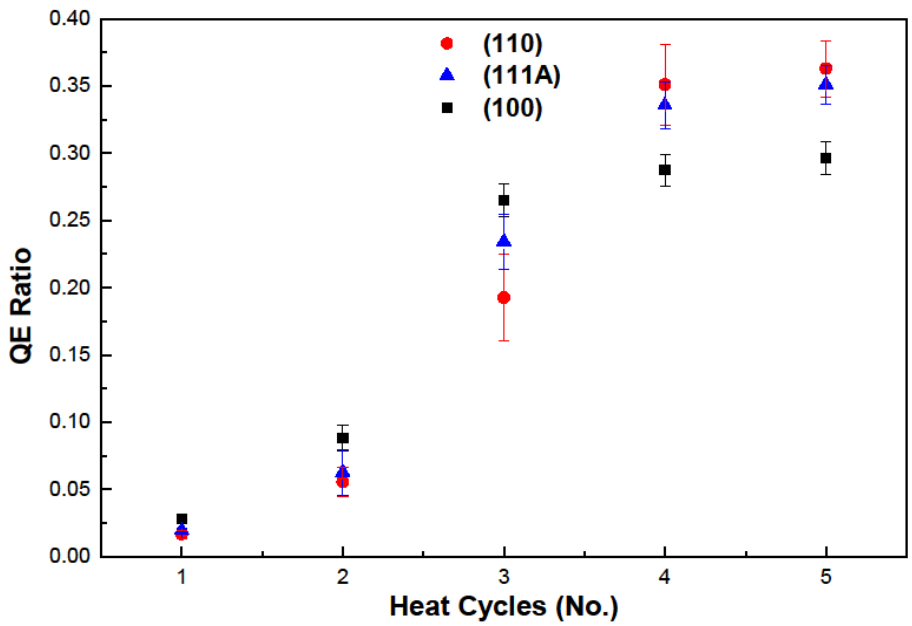

Figure 3-25: QE ratio - samples implanted with 10,000 V hydrogen ions to samples that were not exposed to hydrogen ions - as a function of heat cycle, for bulk GaAs with three different surface-cleave planes. Heat cycle numbers: 1: 250°C for 20 minutes; 2: 370°C for 30 minutes; 3: 490°C for 1 hour; 4 and 5: 550°C for 1 hour

To determine if a specific surface cleave plane provided enhanced ion channeling, the QE results from the 10,000 V ion implantation studies were divided by the non-implantation QE results (as shown in Figure 3-25). Per our supposition, when ions penetrate deeper into the material, they pass beyond the surface region that contributes to photoemission and therefore provide less QE degradation. When comparing QE values of implanted and non-implanted samples, those with the highest QE ratio would correspond to samples with enhanced ion channeling. The simple picture presented in Figure 2-6 suggests samples would be ordered (110), (111A) and (100), in terms of samples supporting the highest level of channeling to the least amount of channeling. This simple picture is consistent with results presented in Figure 3-25, at least for samples that were heated sufficiently long and at a relatively high temperature (see results for heat cycles 4 and 5 in Figure 3-25). The (110) GaAs cleave plane - i.e., the sample with the most "open space" between atoms, and therefore the sample supporting the highest level of ion channeling - exhibited the highest QE ratio. Whereas the cleave plane (100) - i.e., the sample with the least "open space" between atoms, and therefore the sample supporting the lowest level of ion channeling - exhibited the lowest QE ratio. If one assumes a strict QE dependence on atomic number density, the QE of (110) and (111A) cleave planes following ion implantation should be greater than sample (100) by roughly 41 and 15%, respectively. In comparison, looking at Figure 3-25 heat cycle 5 values, the measured QE of (110) and (111A) cleave planes following ion implantation are greater than sample (100) by 33 and 30%, respectively, however there is fairly good agreement between measurements and predictions when error bars are taken into account.

In summary, we have shown that commercial bulk GaAs can be used to manufacture photocathodes with high QE without implementing complicated chemical surface treatments. Sample heating to ~ 550°C inside a vacuum apparatus constructed using modern ultrahigh vacuum techniques was enough to obtain QE near 20% at 532nm for all of the tested cleave plane surfaces, with cleave plane sample (100) providing the highest QE. For accelerator applications requiring high average current, photocathodes like these could produce more than 100 mA average current with just one Watt of laser power.

Implantation of the photocathode with either low or high energy hydrogen ions served to reduce photocathode QE, but the QE degradation caused by 100 V hydrogen ions was modest and QE could easily be recovered following sample heating. In sharp contrast, the QE degradation caused by 10,000 V hydrogen ions was severe and QE could not be fully recovered with heat. These observations suggest that low energy ions penetrate the surface, stopping at locations between atoms and creating interstitial defects that likely reduce the diffusion length of the electrons within the material, reducing the number of available electrons that reach the photocathode surface that can contribute to photoemission. During sample heating, the interstitial defects diffuse throughout the material, restoring the electron diffusion length and the photocathode QE. Whereas high energy ions likely generate knock-out vacancies within the crystal structure that permanently adversely alter the band structure of the semiconductor. As noted above, inside a DC high voltage photogun, the photocathode will be bombarded by considerably more low voltage ions than high voltage ions. This is fortuitous and explains why the photocathode QE can be routinely restored following simple heating and reactivation, except at the electrostatic center of the photocathode, where the highest energy ions are directed. [23,153]

Our data support the simple picture that channeling is enhanced for the sample with the most "open space" between atoms. More "open space" leads to enhanced channeling which means high energy ions create fewer vacancies that lead to reduced and unrecoverable QE. Surface cleave plane (110) has the most "open space" and cleave plane (100) the least "open space". As such, surface cleave plane (110) was the least sensitive to ion bombardment and cleave plane (100) the most sensitive. Considering all the results in total, the best choice for a photogun using bulk GaAs would be surface cleave plane (110), providing the highest QE and least sensitivity to ion bombardment. It's true that modern high-current accelerator applications now prefer alkali-antimonide photocathodes over GaAs photocathodes, because alkali-antimonide photocathodes offer similarly high QE but with longer operating lifetime. However, spin-polarized accelerator applications may be forced to use bulk GaAs as the only practical means to generate milliampere-levels of spin-polarized beam. [172]

We admit that the hydrogen ion source used in this experiment was rather primitive. Ion energy was set by the voltage applied to the sample during implantation, and not by the ion source itself, which introduced unappealing energy-dependent electrostatic focusing at the photocathode sample. And it is important to note that ion implantation was performed with the photocathode NEA layer removed. This

was done for a practical reason, namely, the ion source also emitted neutral atomic hydrogen which is a very effective chemical cleaning agent. The NEA layer was removed prior to implantation so as not to confuse QE reduction due to implantation with uninteresting QE reduction due to chemical removal of the Cs and F layer via atomic hydrogen cleaning. As such, our work did not directly evaluate photocathode sensitivity to sputtering of the Cs and F layer. However, because the ion dose required in this work was orders of magnitude greater than the ion dose delivered to the photocathode inside a photogun operating at 10^{-11} Torr, these results suggest ion sputtering of the NEA layer might be more deleterious than implantation. Future tests aimed at studying ion back-bombardment would benefit from using activated and un-activated photocathodes, and a dedicated ion source offering better control of the applied dose, the ion energy, and the ion distribution at the sample.

3.3 The Polarization Dependence

Photoelectron yield, or quantum efficiency (QE), and electron spin polarization (ESP) are important characteristics of GaAs photocathodes used at electron accelerators worldwide. For decades, photocathode experts have worked to increase these quantities. The QE of GaAs photocathodes is affected by many factors including cathode material quality, the wavelength of the incident light, the thickness of the photocathode, dopant density, the temperature of the photocathode, surface contamination, the negative-electron affinity condition on the photocathode surface, the power density of the laser light, the bias voltage and the vacuum pressure under which photo-extracted beam is produced. These factors also affect ESP via spin relaxation/depolarization mechanisms that influence conduction-band electrons migrating toward the surface of the photocathode, and then emitted into vacuum. Although bulk GaAs provides relatively low polarization compared to the strained-superlattice photocathodes commonly used at modern polarized electron accelerators, [90,153,173] it represents a convenient and inexpensive tool that can help differentiate depolarization mechanisms and possibly assist with the engineering of higher polarization photocathodes. And because high polarization strained-superlattice photocathodes possess relatively low QE, bulk GaAs - with higher QE - might be the only photocathode material that can satisfy the high current requirements of some proposed new applications [174,175]. This work provides an updated evaluation of polarization sensitivities of bulk unstrained GaAs. We perform the studies using commercial bulk GaAs samples and modern equipment and vacuum techniques, evaluating ESP sensitivity to sample temperature, Zn dopant density, Cs-F activation layer, and surface cleave plane orientation. The sample temperature, dopant density and the surface NEA layer have a significant impact on ESP, whereas ESP is insensitive to cleave plane orientation. In general, ESP can be increased at the expense of QE. The highest polarization of 50% was obtained using a bulk GaAs photocathode at 77 K and with a relatively low dopant density.

3.3.1 Spin Relaxation Mechanism

The spin polarization of photoelectrons emitted from highly doped GaAs photocathode at room temperature is a order of ~30%, a value considerably less than the theoretical maximum of 50%. The spin relaxation (or depolarization) of thermalized conduction electrons is the predominant factor reducing the electron spin polarization of photocathode. The investigation of spin relaxation has a long history dating back to the 1950s. Literature describes two main spin relaxation mechanisms for p-type III-V semiconductor: 1) The lack of inversion symmetry in III-V semiconductor leads to a spin splitting of the conduction band, called D'yakonov-Perel (DP) mechanism. [123] 2) The exchange interaction mechanism between electrons and holes, called Bir-Aronov-Pikus (BAP) mechanism. [124] For p-type GaAs, the BAP mechanism is dominant at low temperature and high dopant concentration, and the DP mechanism is dominant at high temperature and low dopant concentration. [125,126] There are other depolarization processes, but these are typically considered to have little consequence and are frequently ignored. These include the Elliot-Yafet (EY) mechanism [121,122] in which the spin–orbit interaction generates non–pure spin states in the conduction band, and radiation trapping, in which ESP is diluted by supplemental photoemission that results from the absorption of linearly polarized recombination light. . There is a wealth of literature describing polarization studies using bulk GaAs, as a function of temperature [125,176,177], dopant concentration [125,176,177] , electron (and hole) density [178], and thickness of the photocathode [179].

Electrons in the conduction band will arrive at an equilibrium polarization when the photocathode reaches a steady-state condition defined as, $dP/dt = P_0/\tau - P/\tau - P/\tau_0 = 0$. The term P_0/τ is the rate of polarization creation using circularly polarized light, P/τ describes polarization loss due to electron recombination to the valence band, and P/τ_0 is the rate at which polarization disappears due to spin relaxation effects. So the equilibrium polarization is given by: [125]

$$P = P_0 \frac{1}{1+\frac{\tau}{\tau_s}} \qquad 3\text{-}1$$

where P_0 is the initial polarization determined by the quantum mechanical selection rules (as mentioned above, $P_0 = 50\%$ for bulk GaAs), τ and τ_s describe the electron lifetime and spin relaxation time for electrons at the bottom of the conduction band, respectively. The electron lifetime τ of GaAs is of the order 10-9 to 10-10 s, with the exact value dependent on the temperature and doping concentration of the sample. The cumulative spin relaxation time is composed of individual spin relaxation mechanisms given by, $1/\tau_s = 1/\tau_s^{DP} + 1/\tau_s^{BAP} + 1/\tau_s^{EY} + 1/\tau_s^{rad}$, where the superscripts represent the different spin relaxation mechanisms mentioned above. For p-type GaAs, the terms related to the EY mechanism and radiation trapping can be neglected.

The GaAs material is lack of inversion symmetry that is broken by the presence of two distinct atoms in the Bravais lattice, which induce the momentum states of the spin-up and spin-down electrons are not degenerate: $E_{\boldsymbol{k}\uparrow} \neq E_{\boldsymbol{k}\downarrow}$. The resulting energy difference plays the role of effective magnetic field

and results in spin precession during the time between collisions, which contribute to spin relaxation due to the magnitude and direction of $\boldsymbol{k}$ changes in an uncontrolled way. This is so called DP mechanism, and the spin relaxation rate is given by: [123,127]

$$\frac{1}{\tau_s^{DP}} = Q\tau_p\alpha^2\frac{(k_BT)^3}{\hbar^2E_g} \qquad 3\text{-}2$$

where Q is a dimensionless factor and ranges from 0.8 to 2.7 depending on the dominant momentum scattering mechanism, τ_p is the momentum relaxation time, α is a dimensionless parameter specifying the strength of the spin-orbit interaction ($\alpha = 4\Delta m_e/m_{ev}\left((E_g+\Delta)(3E_g+2\Delta)\right)^{\frac{1}{2}}$, here m_e is the effective mass of the electron, m_{ev} is a constant close in magnitude to the mass of free electron [176]), and E_g is the bandgap of GaAs. The temperature dependence of the spin relaxation rate is $1/\tau_s^{DP}\sim T^3\tau_p\sim T^{9/2}$. [176]

In p-type GaAs, the spin relaxation can also result from the spin exchange interaction between electrons and holes. This is so called BAP mechanism, and the spin relaxation rate is given in two terms. [124,127] In case of exchange with nondegenerate holes:

$$\frac{1}{\tau_s^{BAP}} = \frac{2}{\tau_0}N_Aa_B^3\frac{v_k}{v_B}\left[\frac{N_h}{N_A}|\psi(0)|^4 + \frac{5}{3}\frac{N_A-N_h}{N_A}\right] \qquad 3\text{-}3$$

where τ_0 is an exchange splitting parameter and given by $1/\tau_0 = (3\pi/64)\,\Delta_{ex}^2/\hbar E_B$ (with Δ_{ex} is the exchange splitting of the excitonic ground state and $E_B = \hbar^2/2m_ea_B^2$ is the Bohr exciton energy), $a_B = \hbar^2\epsilon/e^2m_e$ is the exciton Bohr radius, v_k is the electrons velocity, $v_B = \hbar/m_ea_B$ is the exciton Bohr velocity, N_h is the density of free holes, and $|\psi(0)|^2$ is the Sommerfeld's factor.

In case of exchange with degenerate holes and the electrons velocity v_k is greater than the Fermi velocity of the holes, the spin relaxation rate is given by: [127]

$$\frac{1}{\tau_s^{BAP}} = \frac{3}{\tau_0}N_ha_B^3\frac{v_k}{v_B}\frac{k_BT}{E_f} \qquad 3\text{-}4$$

where E_f is the hole Fermi energy. If the electrons are thermalized, v_k needs to be replaced by the thermal velocity $v_e = (3k_BT/m_e)^{1/2}$.

The temperature dependence of τ_s^{BAP} is dominated by the temperature of $|\psi(0)|^2$ as well as by the density of free holes N_h. The dependence on the acceptor density is essentially $1/\tau_s^{BAP}\sim N_A$ for nondegenerate holes from Eq. (3) and $1/\tau_s^{BAP}\sim N_A^{1/3}$ for degenerate holes from Eq. (4). In between, $1/\tau_s^{BAP}$ is only weakly dependent on N_A.

The formulas cited above were used to calculate the spin relaxation rate as a function of temperature for bulk GaAs with dopant concentrations of $1\times10^{19}\ cm^{-3}$ and $5\times10^{17}\ cm^{-3}$, as shown in Figure 3-26. The BAP mechanism clearly dominates over the DP mechanism, which contributes appreciably only at higher temperature. The clear message from this plot is that low spin relaxation rates - and

therefore higher ESP – will be obtained at lower dopant densities and temperatures. For the p-doped samples evaluated in this work and over the temperature range studied, the spin relaxation rate $1/\tau_s$ varied from ~ 6 x 108 to 1 x 1010 s-1, corresponding to spin relaxation times between $10^{-10} - 10^{-9}\ s$.

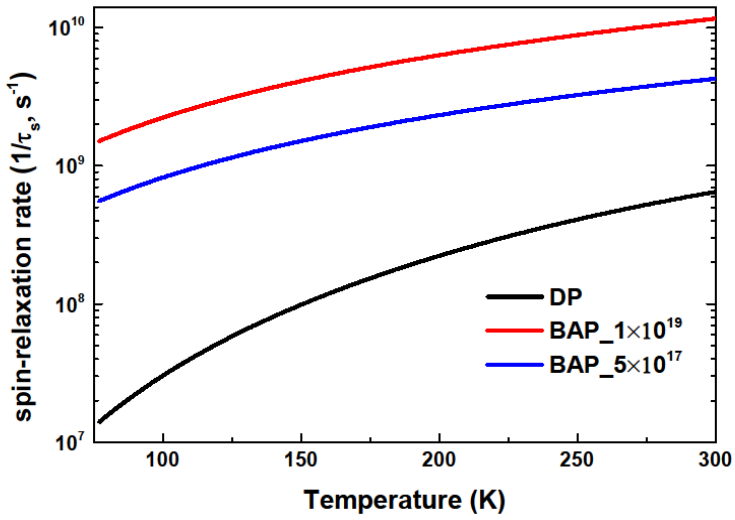

Figure 3-26: Temperature dependence of the spin relaxation rate for the DP mechanism, BAP mechanism in bulk GaAs with dopant concentrations of $\mathbf{1 \times 10^{19}}\ \boldsymbol{cm^{-3}}$ and $\mathbf{5 \times 10^{17}}\ \boldsymbol{cm^{-3}}$

3.3.2 Evaluation of Electron Escape Probability

The QE of GaAs photocathode can be estimated by Eq. 2-11. Assuming the $\frac{\alpha_{pe}}{\alpha} = 1$, the equation is simplified as:

$$QE = (1 - R)\frac{P}{1+\frac{1}{\alpha L}} \qquad 3\text{-}5$$

where R represents the reflectively of the photocathode, α is the absorption coefficient, L describes the electron diffusion length, and P_{esc} is the electron escape probability. Since the QE of a photocathode is easily measured as a function of the illumination wavelength, Equation 5 can be used to solve for the escape probability, which is expected to be very sensitive to the photocathode surface condition and activation process, and therefore could prove relevant for interpreting polarization behavior:

$$P_{esc} = (1 + \frac{1}{\alpha L})\frac{QE}{(1 - R)}$$

The reflectivity R and the absorption coefficient α depend on the wavelength of incident light and the temperature of the photocathode, whereas the electron diffusion length L depends on the temperature and doping concentration of the sample. In sections below, expressions are developed to estimate the terms R, α, and L.

1) Modeling the optical constant R and α of GaAs

The optical dielectric function $\epsilon = \epsilon_1 + i\epsilon_2 = \overline{n}^2 = (n + ik)^2$ is estimated by the modified Adachi's model. The optical dielectric function in Adachi's model [180,181] is represented by the sum of terms attributed to four energy gaps (E_0, $E_0 + \Delta_0$, E_1, $E_1 + \Delta_1$) and damped harmonic oscillators describing the contributions from higher lying transition (E_0', $E_2(X)$, $E_2(\Sigma)$), which describe transitions for inter-band critical points (CPs) in the joint density of states. Rakic and Majewski [182] proposed a modification model, in which the damping constants were replaced with the frequency dependent damping expression.

The E_0 and $E_0 + \Delta_0$ transitions in GaAs are of the three-dimensional (3D) M_0 CPs. The contribution of these gaps transitions to dielectric function is given by [183]

$$\epsilon_1(E) = A{E_0}^{-3/2}[f(X_0) + \frac{1}{2}\left(\frac{E_0}{E_0+\Delta_0}\right)^{3/2} f(X_{0s})] \qquad 3\text{-}6$$

with

$$f(X) = X^{-2}[2 - \sqrt{1+X} - \sqrt{1-X}] \qquad 3\text{-}7$$

$$X_0 = \frac{E+i\Gamma_0}{E_0}, X_{0s} = \frac{E+i\Gamma_0}{E_0+\Delta_0} \qquad 3\text{-}8$$

where A and Γ_0 are the strength and damping constants of the E_0 and $E_0 + \Delta_0$ transitions, respectively. The 3D-exciton effect at the E_0 and $E_0 + \Delta_0$ CPs can be neglect for GaAs.

The E_1 and $E_1 + \Delta_1$ transitions in GaAs are of the two-dimensional (2D) M_0 CPs. The contribution of this type of CPs to dielectric function is given by 183]

$$\epsilon_2(E) = -B_1{X_1}^{-2}\, ln\left(1 - {X_1}^2\right) - B_{1s}X_{1s}ln(1 - {X_{1s}}^2) \qquad 3\text{-}9$$

with

$$X_1 = \frac{E+i\Gamma_1}{E_1}, X_{1s} = \frac{E+i\Gamma_1}{E_1+\Delta_1} \qquad 3\text{-}10$$

where $B_1(B_{1s})$ and Γ_1 are the strengths and damping constants of the E_1 and $E_1 + \Delta_1$ transitions, respectively. Since the coulomb-like interaction is always present between the electron and holes, the excitonic state should exist. The contribution of the Wannier-type 2D excitons at E_1 and $E_1 + \Delta_1$ CPs to dielectric function can be given by [183]

$$\epsilon_3(E) = \sum_{n=1}^{\infty} \frac{1}{(2n-1)^3}\left(\frac{B_{1x}}{E_1 - [G_1/(2n-1)^2] - E - i\Gamma_1} + \frac{B_{2x}}{E_1 + \Delta_1 - [G_{1s}/(2n-1)^2] - E - i\Gamma_1}\right) \qquad 3\text{-}11$$

where B_{1x} (B_{2x}) and G_1 (G_{1s}) are the strengths and Rydberg energy of the E_1 and $E_1 + \Delta_1$ excitons, respectively. Here, it is assumed that $G_1 = G_{1s} = 0$.

The nature of the E_0', $E_2(X)$ and $E_2(\Sigma)$ transitions is more complicated. They do not correspond to a single, well-defined CP. These CPs can be characterized by the damped harmonic oscillators and written as [184]

$$\epsilon_4(E) = \sum_{j=2}^{4} \frac{{f_j}^2}{{E_j}^2 - E^2 - iE\Gamma_j} \qquad 3\text{-}12$$

with $f_j = \sqrt{C_j {E_j}^2}$, where C and Γ_j are strengths and damping constants of the E_j (E_0', $E_2(X)$ and $E_2(\Sigma)$) transitions, respectively.

In the modification model, the damping constants Γ_i were replaced with the frequency dependent damping expression Γ_i' that given by [182]

$$\Gamma_i' = \Gamma\left[-\alpha\left(\frac{E-E_0}{\Gamma}\right)^2\right] \qquad 3\text{-}13$$

where the additional parameter α allows for a continuous change of the linearly range from a purely Lorentzian (for $\alpha = 0$) to nearly Gaussian (for $\alpha = 0.3$).

The optical dielectric function is obtained by summing over all the contributions as described above with replacing the damping constants Γ_i with the frequency dependent damping expression Γ_i', and written by

$$\epsilon(E) = \epsilon_\infty + \epsilon_1(E) + \epsilon_2(E) + \epsilon_3(E) + \epsilon_4(E) \qquad 3\text{-}14$$

where ϵ_∞ is the high-frequency dielectric constant containing the contribution of higher-lying transitions. The energy gaps E_0, $E_0 + \Delta_0$, E_1, $E_1 + \Delta_1$, E_0', $E_2(X)$, and $E_2(\Sigma)$ change with the temperature, thus the optical constant is a function of temperature. We finally arrive at the temperature dependence of the optical absorption coefficient α and reflectively R by recalling, $\epsilon = (n + ik)^2$ and noting:

$$\alpha = \frac{4\pi k}{\lambda}$$

$$R = \left|\frac{1-n}{1+n}\right|^2$$

The calculation refractive index n and extinction coefficient k for GaAs at 300 K are shown in Figure 3-27 as a function of photon energy and wavelength compared with the experiment data. [114,115,116] It shows the calculating by the modified Adachi's model match well with the experiment data.

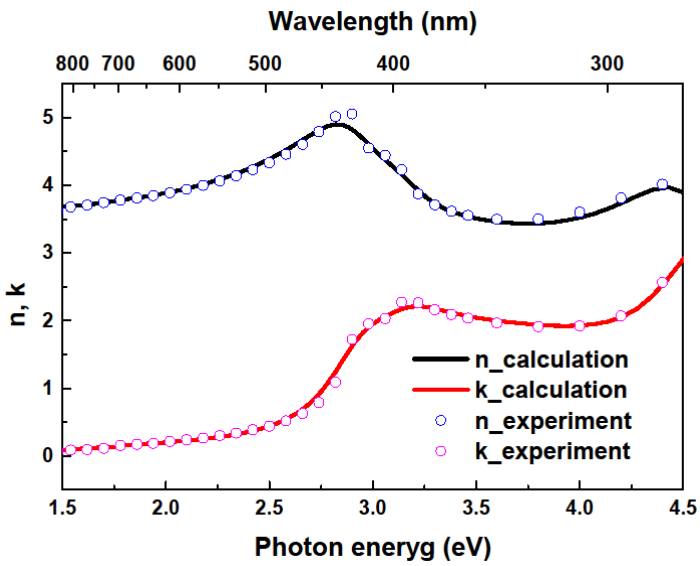

Figure 3-27: The refractive index and extinction coefficient for GaAs at 300 K.

The energy gaps (E_0, $E_0 + \Delta_0$, E_1, $E_1 + \Delta_1$, E_0', $E_2(X)$, $E_2(\Sigma)$) changes with the temperature, thus the optical constant is a function of temperature. Adding the temperature dependence of bandgaps energy into the optical dielectric function, we can obtain the temperature dependence of the optical constant, and therefore achieve the temperature dependence of the optical absorption and reflectivity. The calculation of temperature dependence of optical absorption coefficient and reflectivity for GaAs responded to 650 nm are shown in Figure 3-28 and Figure 3-29, respectively.

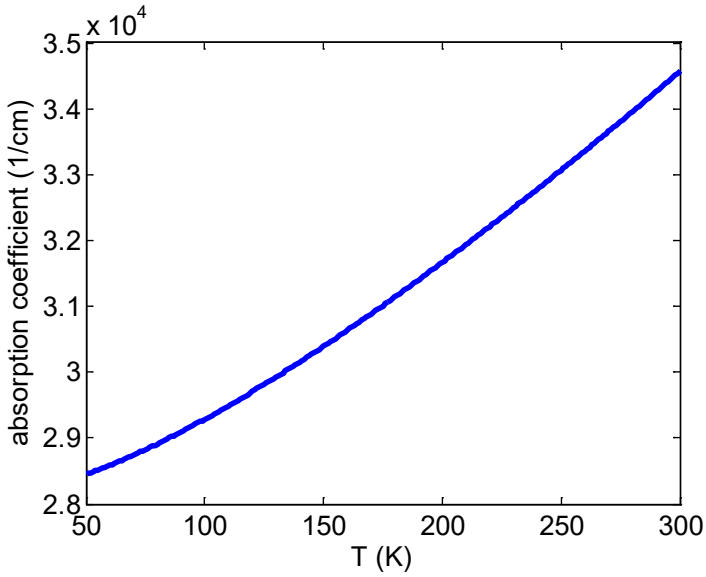

Figure 3-28: The temperature dependence of optical absorption coefficient for GaAs responded to 650 nm

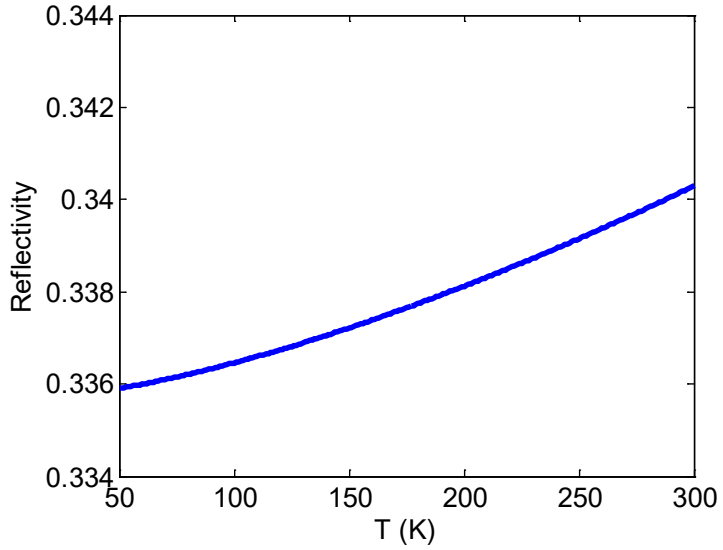

Figure 3-29: The temperature dependence of optical reflectivity for GaAs respond to 650 nm

2) Calculating the electron diffusion length in GaAs

The electron diffusion length is the average distance that electrons can move before they recombine. It depends on the electron lifetime and diffusion constant that is relative to the electron mobility and temperature in GaAs. The electron diffusion length can be given by

$$L = \sqrt{D \cdot \tau} \qquad 3\text{-}15$$

where electron lifetime τ is the average time electrons exist before they recombine with holes. The electron recombination rate determines the lifetime, and there are three types of recombination in GaAs: radiative recombination, Auger recombination, and Shockley-Read-Hall recombination. The recombination rate depends on the doping concentration and temperature, thus the electron lifetime relate to the doping concentration and temperature in GaAs, which is range from 10-9 to 10-10 s. The diffusion constant D can be given by Einstein–Smoluchowski relation:

$$D = \frac{\mu k_B T}{e} \qquad 3\text{-}16$$

where e is the electron charge, T is the absolute temperature, k_B is the Boltzmann's constant, and μ is the electron mobility that also depends on the temperature and doping concentration, and can be estimated by [185]

$$\mu = \mu_{min} + \frac{\left(\frac{300}{T}\right)^{\theta_1} \mu_{max}(300) - \mu_{min}}{1 + \left(\frac{N}{(T/300)^{\theta_2} N_{ref(300)}}\right)^{\lambda}} \qquad 3\text{-}17$$

Where N is the doping concentration of GaAs; $\theta_1, \theta_2, \lambda$ are constants; μ_{min} is the saturation mobility at very high doping concentration, which is temperature independent; $\mu_{\max}(T)$ is the saturation mobility

at very low doping concentration, which itself reduces with increasing temperature; $N_{ref}(T) = \left(\frac{T}{300}\right)^{\theta_2} N_{ref}(300)$ is the doping concentration at which mobility reduces to almost half of its maximum value at low doping.

Figure 3-30 shows the electron diffusion length for GaAs with doping concentration of $1 \times 10^{19}\ cm^{-3}$ as a function of temperature. The electron diffusion length decreases with increasing temperature.

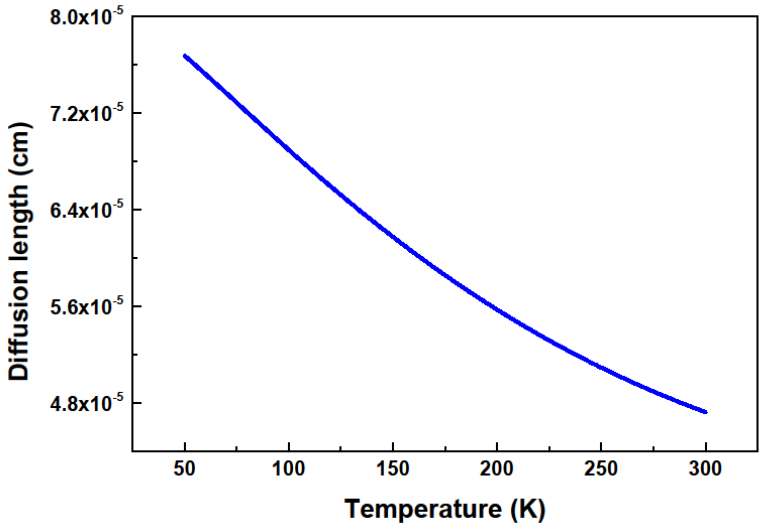

Figure 3-30: The electron diffusion length for GaAs with doping concentration of $\mathbf{1 \times 10^{19}\ cm^{-3}}$ as a function of temperature

To summarize, photocathode QE and ESP can be measured as a function of illumination wavelength. From these measurements, one can infer the wavelength-dependent quantities *R, α,* and *L*, and thereby estimate the photocathode escape probability, P_{esc}. In this work, we attempt to correlate P_{esc} to ESP.

3.3.3 Experiments and Results

1) Experiments

All of the p-doped bulk GaAs samples were purchased from a commercial vendor and manufactured using the vertical gradient freeze technique. Sample characteristics, including Zn dopant carrier concentration and surface cleave plane orientation, are shown in Table 3-3. Samples were cleaved into 15 x 15 mm squares from 3” diameter wafers. No chemical preparation was performed on samples prior to installation in the vacuum test chamber.

Table 3-3 The specifications of bulk GaAs samples

	(111A)	*(110)*	*(100)*	*(100)*	*(100)*
Dopant	GaAs-Zn	GaAs-Zn	GaAs-Zn	GaAs-Zn	GaAs-Zn
Orientation	(111A) ±0.5°	(110) ±0.5°	(100) ±0.5°	(100) ±0.5°	(100) ±0.5°
Carrier concentration (a./c.c.)	$1.1-1.14\times10^{19}$	$1.3-1.4\times10^{19}$	$1.0-1.3\times10^{19}$	$1.6-1.79\times10^{18}$	$5.01-6.0\times10^{17}$
Resistivity (ohm.cm)	$7.17-7.38\times10^{-3}$	$6.1-6.6\times10^{-3}$	$6.6-7.7\times10^{-3}$	$2.48-2.68\times10^{-2}$	$5.4-6.23\times10^{-2}$
Mobility (cm2/v.s.)	$77-78$	$71-74$	$74-80$	$141-146$	$193-200$
Thickness (μm)	$500-550$	$475-525$	$600-650$	$325-375$	$425-475$

Each sample (one at a time) was attached to a sample holder and installed into mini-Mott chamber. At typical vacuum pressure $\sim10^{-11}$ Torr, photocathodes were heated to 550 °C to remove adsorbed gas, then cooled to room temperature and activated to achieve a negative electron affinity condition using the standard yo-yo activation procedure with cesium and NF_3. A low average power (~uW) laser was provided by the laser source to measure QE and ESP to avoid the surface charge saturation limit [99,186].

The sample holder consisted of a hollow stainless-steel tube with thin molybdenum end plate upon which the sample was affixed. The heater that was normally inserted into the bore of the holder could be removed, providing a means to cool photocathode samples. Samples could be cooled by filling the sample holder with dry ice or liquid nitrogen. Samples remained cold for many hours with just one filling. A thermal analysis indicated sample temperature was very nearly identical to the temperature of the LN_2.

2) Temperature and Zn dopant dependence

Three photocathodes, each with 100 surface-cleave plane but with dopant densities spanning roughly 1.5 orders of magnitude, were activated at room temperature and evaluated using the retarding field Mott-polarimeter apparatus. Photocathode QE and ESP were measured as a function of illumination wavelength, first at room temperature and then with the sample holder filled with dry ice (195K) and LN2 (77 K). Care was taken to evaluate ESP at the same photocurrent to ensure similar photoelectron density at the photocathode, and at low laser power to minimize sensitivity to surface charge limit.

The QE and ESP spectral scans presented in Figure 3-31 exhibit the typical shape for bulk GaAs, namely ESP increases while QE decreases as the energy (wavelength) of the illumination light is decreased (increased), with the highest polarization obtained when the energy of the light is equal to the semiconductor bandgap ensuring that only electrons from the $P_{3/2}$ ground state are excited to the conduction band. More interesting is the effect of dopant density on QE and ESP. Higher dopant concentrations serve to increase band bending, which lowers the surface work function, which increases

the electron escape probability and leads to higher QE, however at the expense of polarization. For the commonly used dopant density of $10^{19}\ cm^{-3}$, photocathode QE at room temperature reached ~ 6.9% but provided a maximum ESP of only ~ 30%. Polarization increased to ~ 41% for the low-doped sample but provided QE of only ~ 1.5%. This behavior is consistent with predictions of the BAP mechanism that describes the spin relaxation rate proportional to the dopant concentration. Higher dopant concentration leads to greater spin relaxation rate, and thus lower ESP.

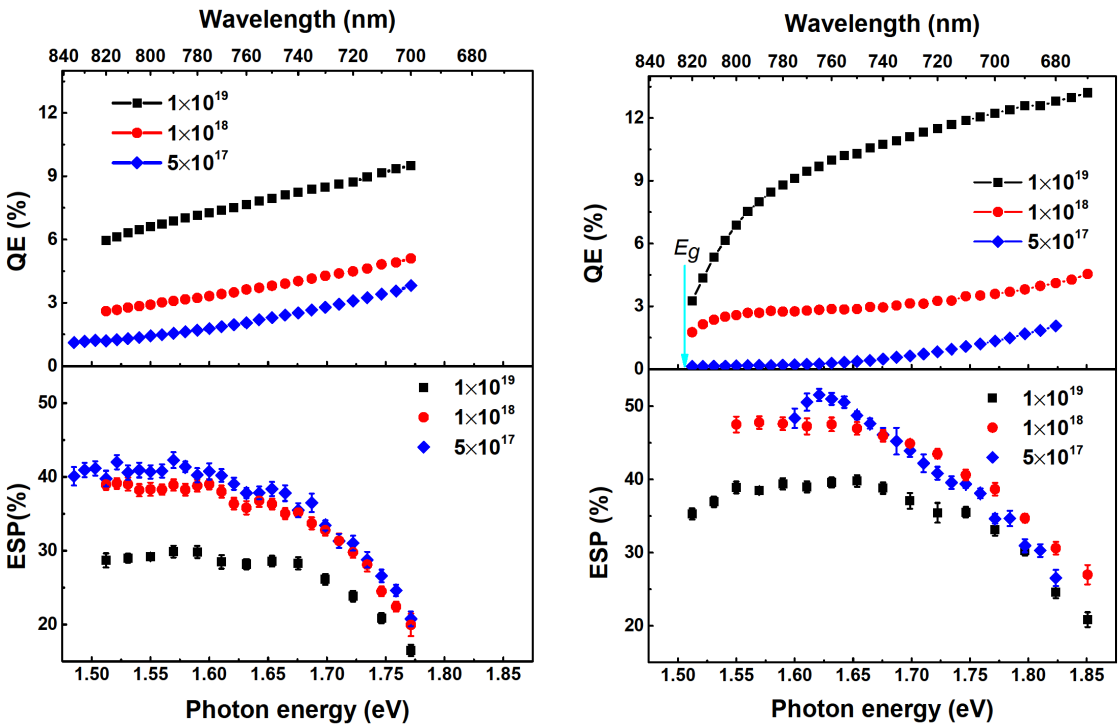

Figure 3-31: The QE and ESP of bulk GaAs (100 cleave plane) with different Zn dopant densities, and measured at 300 K (left) and 77 K (right). Error bars are statistical. Axes ranges were kept identical to highlight the measurement variations observed between conditions. The bandgap energy E_g could be discerned for samples at 77K (note arrow).

Cooling the samples to 77K modifies the crystal lattice structure and shifts the bandgap energy. This bandgap shift means peak polarization occurs at higher photon energies. The bandgap energy for GaAs can be calculated using $E_g(T) = 1.519 - \frac{5.41\times10^{-4}T^2}{T+204}$, which yields bandgaps of 1.51 and 1.42 eV for samples at 77 and 300K, respectively. Only the 77 K bandgap "knee" is visible in the QE spectral plot of Figure 3-31 (top right). More noteworthy is the significant increase in ESP observed for all three samples cooled to 77K. The ESP for the highly-doped sample increased from ~30 to 41%, and from ~ 40 to 52% for the low-doped sample. This behavior is consistent with Figure 3-26 which predicts smaller spin relaxation rates for both mechanisms (BAP and DP) at lower temperature. It is interesting to note that for the low-doped sample at 77K, measured polarization exceeds the theoretical maximum value of 50%. This could point to an inaccurate effective Sherman Function used in the Mott polarimeter analysis, with this measurement serving to identify the magnitude of systematic error relevant to the entire study, or perhaps an indication of interesting physics phenomenon, e.g., the

creation of strain within the sample at cryogenic temperature, which serves to eliminate the energy level degeneracy of the $P_{3/2}$ ground state.

The temperature and dopant density studies are summarized in Figure 3-32, which shows ESP versus temperature for the three samples with different dopant concentrations. Overall, lower temperature leads to lower spin relaxation rate, and therefore higher ESP. From this plot, it is difficult to discern the impact of each spin relaxation mechanism, DP versus BAP. The DP mechanism is supposed to play a role only for low dopant samples, which is the only expected to play a role.

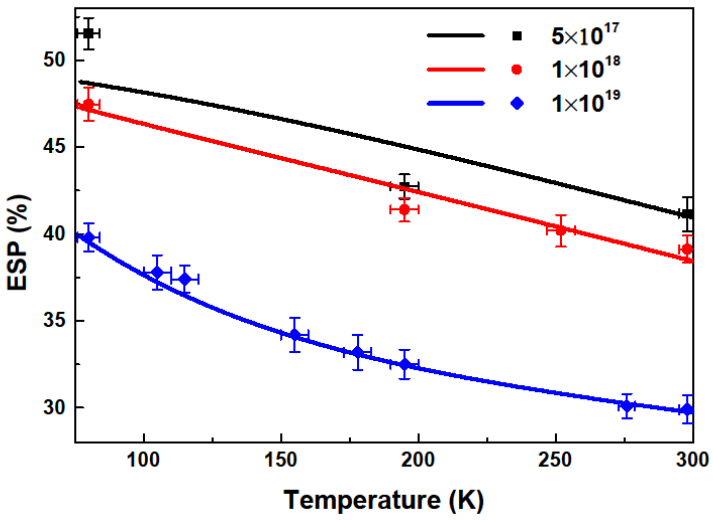

Figure 3-32: Maximum ESP versus sample temperature and dopant density (the wavelength of illumination was allowed to vary to provide peak polarization). Vertical error bars are statistical. Horizontal error bars are attributed to uncertainty in sample temperature.

As mentioned above, sample temperature affects the bandgap energy, which influences the wavelength required for peak polarization. For a constant illumination wavelength, the QE of the photocathode decreases as the sample temperature is reduced. However, if the illumination wavelength is allowed to vary to achieve the highest ESP, photocathode QE should remain nearly constant. It was difficult to verify this statement because of surface contamination on the photocathode surface that occurred as samples were cooled to cryogenic temperature. Imperfect vacuum led to gas adsorption on the photocathode surface, which influenced P_{esc} and therefore QE. It was difficult to ensure identical photocathode surface conditions throughout the temperature study. The QE change was uncertain during cooling down the photocathodes. Figure 3-33 shows the photocurrent evolution as a function of time during cooling down the photocathodes with different dopant concentration. As the temperature goes down, the photocurrent firstly increases and then decreases. For the high dopant concentration sample, the QE at 77 K was higher than that at 300 K. However, the QE at 77 K was lower than that at 300 K for the low dopant concentration sample. The QE values for samples at room temperature, at the wavelength of peak polarization, were 6.9%, 3.1% and 1.5% (in order decreasing dopant concentration) compared to 10%, 2.9% and 0.79% for samples at 77K.

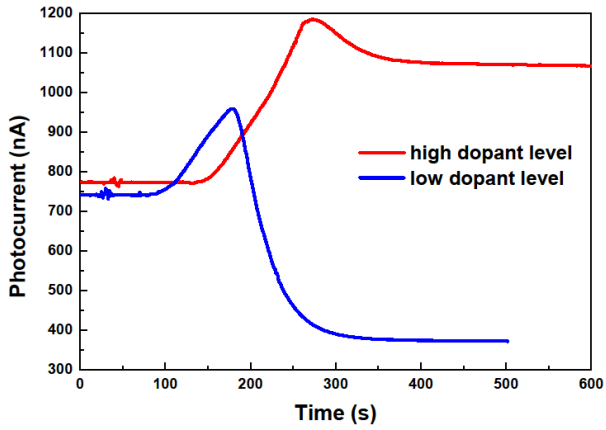

Figure 3-33: The photocurrent evolution as function of time during filling LN2 into stalk to cool down photocathodes with different dopant concentration from 300 K to 77 K. Photocurrent firstly increase and then decrease as temperature goes down

The calculation of electron escape probability for GaAs (100) photocathode at different temperature is shown in Figure 3-34 as a function of photon energy and wavelength. When the photocathode was cooled down, more electrons can reach to the surface and emitted into vacuum due to the electrons energy and NEA state changed, i.e., the electron escape probability went up. However, when the temperature went to too low, too more electrons reach to the surface, leading to a fraction of electron couldn't escape and accumulated on the surface, which caused the NEA state going up and reduced the electron escape probability, this is so-called surface charge saturation limit.

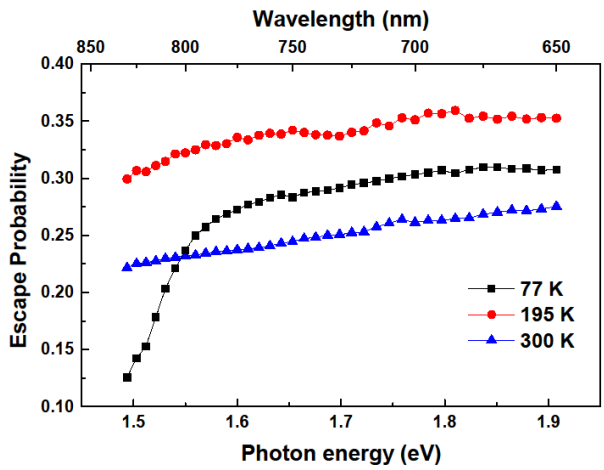

Figure 3-34. The electron escape probability for GaAs (100) photocathode at different temperature

3) Activation layer dependence

Some accelerators report delivering electron beams with higher ESP by intentionally varying the amount of chemicals applied to the photocathode surface, [187] in which the chemicals used to reduce the surface work function and create an NEA condition. To explore this behavior, the QE and ESP of GaAs photocathode with dopant concentration of $1 \times 10^{19}\ cm^{-3}$ were measured at different times

throughout the activation process. The so called "yo-yo" method of activation was employed, where the photocathode was exposed to incremental doses of Cs and NF_3 in an alternating manner until photocurrent (and therefore QE) reached a maximum value. The first measurements of QE and ESP occurred with only Cs deposited on the photocathode surface. Specifically, Cs was deposited until photocurrent fell to half of its first peak value. Then QE and ESP were measured after adding only one dose of NF_3 which served to double the photocathode QE. Then continuing the yo-yo activation, QE and ESP measurements were made at the 6th and 13th cycles. At the 13th application of Cs and NF_3, the photocathode QE had reached a maximum and the activation was considered complete. These measurements are summarized in Figure 3-35, showing QE and ESP a function of the photon energy and laser wavelength. The QE behavior is not surprising, with QE increasing significantly throughout the activation process until the photocathode NEA layer was fully formed at the 13th cycle. Photocathode QE at the wavelength of maximum polarization increased from 0.2, to 1.1, to 4.2 to 7%, for each of the cycles mentioned above. With only Cs, the maximum ESP was ~ 36% but fell to 32% with the addition of NF_3. At the 6th and 13th yo-yo cycles, ESP was constant at ~30%, which is a value consistent with measurements of the highly doped sample at room temperature described previously.

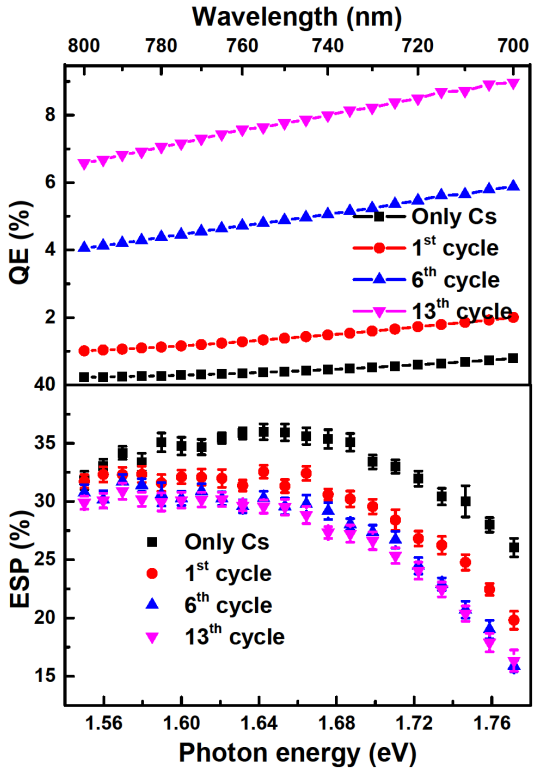

Figure 3-35: QE and ESP for bulk GaAs (110 cleave plane) with dopant concentration of $\mathbf{1 \times 10^{19}}$ as a function of surface activation layer. Cycle number refers to the number of applications of Cs and F. Error bars are statistical.

Ref. 187 describes depolarization at the surface activation layer (Cs-O-Cs layer) governed by the functional form: $P(n) = P_0 \exp(-\sigma n)$. Where, P_0 is the polarization of electrons that reached the photocathode surface but not passed thorugh the activation layer, σ is the exchange scattering cross

section between the electrons and the scattering sites in the activation layer, and n is the number of scattered electrons per cm^2 in the activation layer. This simple model suggests thicker activation layers introduce more scattering sites, and therefore more opportunity for spin relaxation. Our measurements partially support this idea, namely, an activation layer composed of only Cs provided the fewest scattering sites and the highest ESP. However, it would seem ESP would continue to decrease with each successive yo-yo cycle, whereas our measurements show nearly constant ESP for the 6th and 13th yo-yo cycles. This would imply there is a critical value of depolarization caused by this proposed mechanism. Once the thickness of a Cs-F layer reaches the critical value, additional Cs and NF_3 deposition does not lead to further depolarization.

Another explanation for the ESP behavior illustrated in Figure 3-35 relates to the height of the surface work function, the width of the band bending region, and thickness of the potential barrier that electrons must tunnel through to reach vacuum. When the NEA layer is fully formed, the height of the potential barrier is comparatively low, and the band bending region is wide. Electrons fall into the band bending region and thermalize. These electrons have more opportunity to depolarize and still leave the photocathode into vacuum. When the NEA layer is only partially formed, only the highest energy electrons can overcome the potential barrier at the surface, and these electrons have not thermalized and therefore they possess higher ESP.

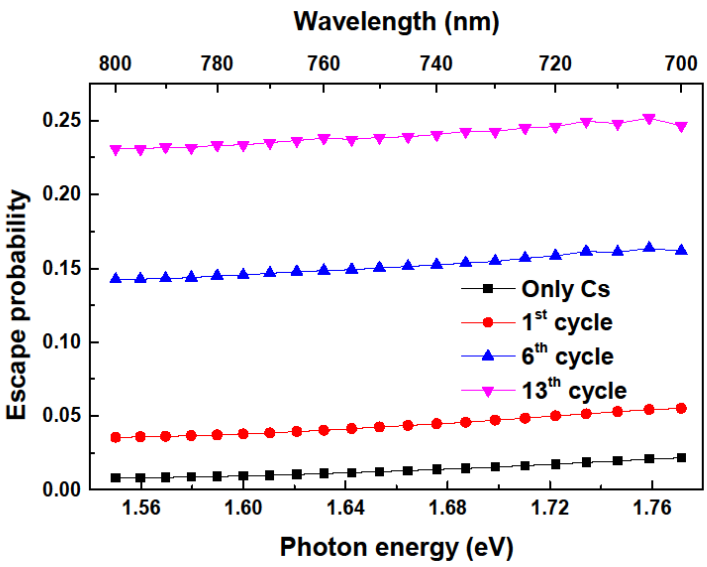

Figure 3-36: The electron escape probability for GaAs (100) at different activation cycles

The electron escape probability for GaAs (100) at different activation cycles was calculated and shown in Figure 3-36. Depositing Cs onto GaAs surface decrease the EA by forming Cs-As electric dipole, making it is possible that electron escape from the surface. However, the EA is still high that only a few electrons can be emitted, so the electron escape probability is very low. After NF_3 depositing onto the surface, the Cs-F electric dipole was formed, as a result, the EA was further decreased and continuously decrease as depositing more Cs and NF_3, leading to the electron escape went up. After

depositing enough thickness of Cs-F layer, the NE decrease to minimum value to form NEA state, and the electron escape probability reach to maximum value.

4) Cleave planes dependence

The final study relates to the photocathode crystal orientation. Photocathode QE and ESP were evaluated for bulk GaAs samples with (100), (110), and (111A) surface cleave planes. Each sample had the same nominal Zn dopant concentration $1 \times 10^{19}\ cm^{-3}$. Photocathodes were activated in an identical manner to ensure similar surface conditions. As shown in Figure 3-37, the cleave planes (100) and (110) provided the highest QE (~ 7%) and cleave plane (111A) provided the lowest QE (~ 6%) at the wavelength of maximum polarization. No difference in ESP could be discerned between samples: the maximum ESP for all three samples was ~30%. From this measurement, it appears crystal orientation does not affect the ESP of bulk GaAs photocathodes.

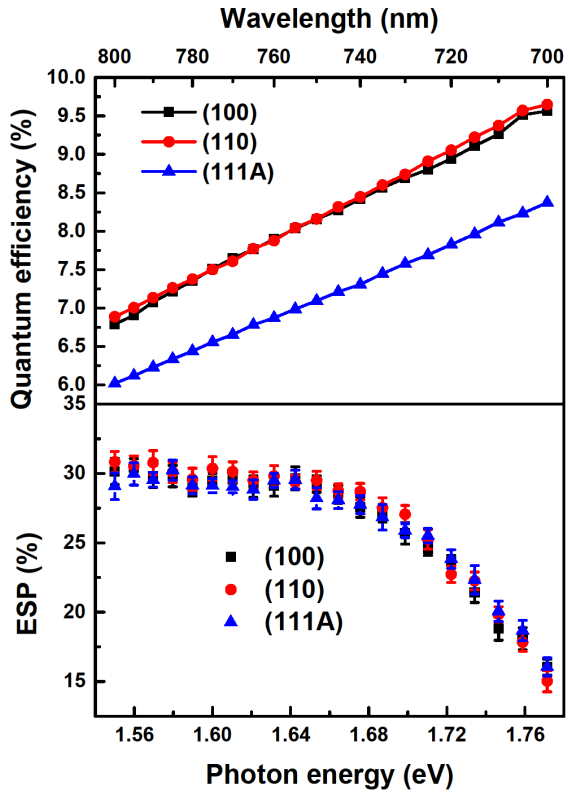

Figure 3-37: QE and ESP of bulk GaAs with three different cleave planes, Zn dopant concentration $\mathbf{1 \times 10^{19}\ cm^{-3}}$ measured at room temperature. Error bars are statistical.

The difference between the QE of three bulk GaAs photocathodes was caused by the difference of electron escape probability for three photocathodes. The calculated electron escape probability for three photocathodes is shown in Figure 3-38. The (100) and (110) surface with equal amounts of Ga and As atoms at the surface provide similar electron escape probability, and therefore similar QE. The (111A) surface comprised of only Ga atoms has the lowest electron escape probability, and therefore lowest QE.

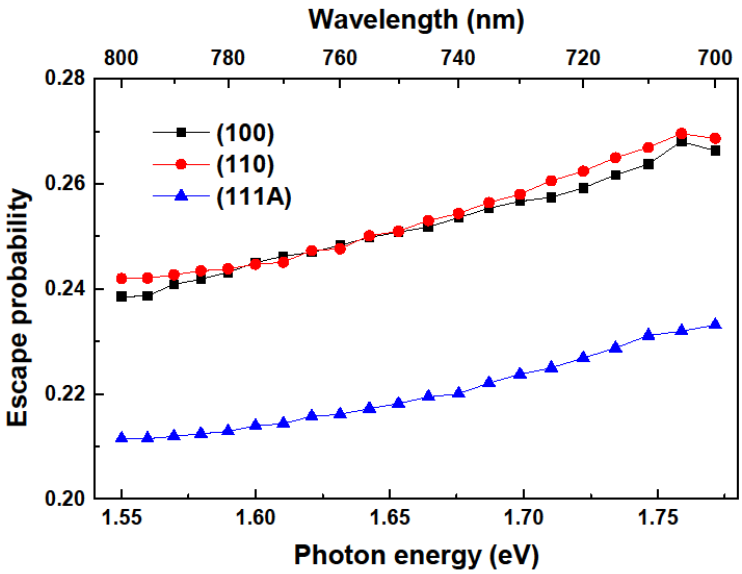

Figure 3-38: The electron escape probability for three bulk GaAs photocathodes

The electron escape probability is also relating to the photon energy (or wavelength), which increases with increasing photon energy. Electrons absorbed photon with higher energy has higher kinetic energy after being excited into conduction band. As a result, the average energy of these electrons transported to the surface is higher. These high energy electrons are easier to escape into vacuum, i.e. they exhibited high escape probability, and therefore high QE.

3.3.4 Discussion

This work clearly illustrates the importance of temperature and dopant density as factors that influence ESP of bulk GaAs photocathodes, in a manner consistent with accepted BAP and DP spin relaxation mechanisms. Highly doped bulk GaAs samples at room temperature provide ESP ~ 30%, but at low temperature and with low dopant concentration, samples provided ESP comparable to the theoretical maximum value of 50%. Measured ESP of 52% (for lowest doped sample at 77K) could indicate an inaccurate effective Sherman Function used in the Mott polarimeter analysis, however the retarding field Mott polarimeter was originally calibrated against the MeV Mott polarimeter used at CEBAF [153], which is considered to be a very accurate device. Table 3-4 lists maximum ESP values from cited references. Maximum ESP values exceeding 50% from bulk GaAs were also reported by Peirce et al. [82] Our dopant density-dependent measurements contradict those of Fishman et al. [125] who reported increasing ESP as at higher dopant concentration. However, it is widely accepted that higher ESP is obtained with lower dopant concentrations – these older measurements must have suffered from an unknown systematic error.

Table 3-4: Reported maximum ESP values

Reference	*note*	*Dopant Concentration*	*Temperature (K)*	*Max ESP(%)*
This work		1×10^{19}	300	30
This work		1×10^{19}	77	40
This work		$5 - 6 \times 10^{17}$	77	52
Ref. 82 (Pierce)	NEA	1.3×10^{19}	< 10	40
Ref. 82 (Pierce)	PEA	1.3×10^{19}	< 10	54
Ref. 179 (Maruyama)	0.9 um thick	5×10^{18}	300	41
Ref. 179 (Maruyama)	0.2 um thick	5×10^{18}	300	49
Ref. 125 (Fishman)		4×10^{19}	4.2	45
Ref. 125 (Fishman)		4×10^{18}	4.2	41
Ref. 125 (Fishman)		8×10^{16}	4.2	38
Ref. 125 (Fishman)		4×10^{18}	77	29
Ref. 188 (Hartmann)	Time resolved – Max. value	$2 - 3 \times 10^{19}$	300	43
Ref. 188 (Hartmann)	Time resolved - Ave. value	$2 - 3 \times 10^{19}$	300	27

Our measurements also point to ESP sensitivity to the activation layer. A photocathode with a more fully formed NEA condition, i.e., a thicker activation layer, exhibited lower ESP. Two explanations were discussed: electron scattering within the Cs-F surface layer, and a filtering effect associated with the characteristics of the band bending region. Because measured ESP was only sensitive to the first yo-yo cycles of chemical deposition, it seems more likely the observed ESP dependence relates to the characteristics of the band bending region. A thicker activation layer reduces the work function at the surface, creating a deeper band bending region. Electrons thermalize within the band bending region, with more opportunity to depolarize, and yet still escape to vacuum. A thinner activation layer provides a comparatively higher potential barrier which serves to filter out electrons that have suffered depolarization. This measured trend is consistent with the measurements of ref. 82, comparing positive and negative electron affinity surface conditions. Although cleave plane samples (100) and (110) provided higher QE compared to cleave plane (111A), there was no ESP sensitivity to crystal orientation.

In the introductory sections of this paper, considerable effort was devoted to deriving P_{esc} with the intention of discerning a relationship between P_{esc} and ESP. The QE and ESP measurements presented herein where used to calculate P_{esc} and are summarized in Figure 3-39. Except for "cleave plane", all the parametric variables studied show ESP inversely proportional to P_{esc}, and consequently QE. So, in general, it can be said that ESP can be increased at the expense of QE. But it is also important to note low QE does not always imply high ESP. For example, a photocathode with contaminated surface can provide both low QE and low ESP.

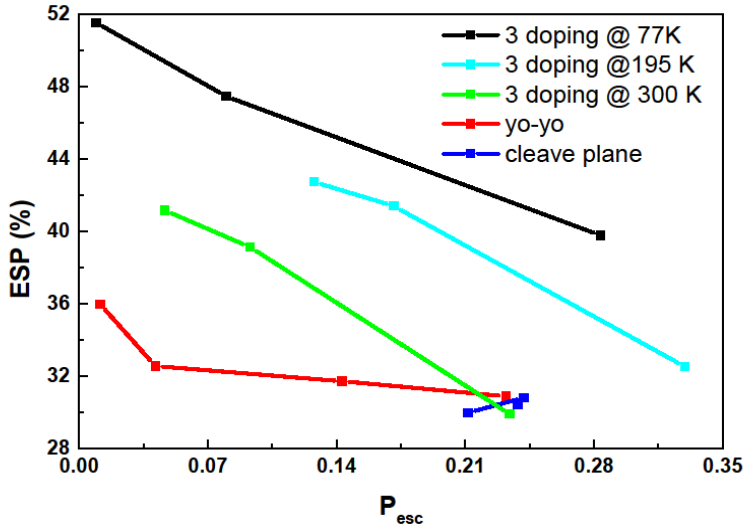

Figure 3-39: Maximum ESP versus $\mathbf{P}_{esc}$ for all the bulk GaAs photocathodes studied

3.4 Summary

In this chapter, GaAs polarization photocathodes are studied in two aspects. The effect of hydrogen ion back-bombardment on the QE of GaAs photocathode was studied systematically for the first time. The dependence of spin polarization on sample temperature, doping concentration, surface activation layer and crystal cleave orientation was evaluated using GaAs photocathode installed into the UHV chamber. The main research contents and results are summarized as follows:

1. Experiments show that commercial GaAs can be used as a good photocathode material without complicated chemical cleaning. The activated GaAs photocathode can produce a QE of up to 20% (corresponding to the laser wavelength of 532 nm).

2. The implantation of low-energy and high-energy hydrogen ions into photocathode results in the decrease of photocathode QE. Moreover, the QE decrease caused by the implantation of high-energy hydrogen ions is much greater than that caused by the implantation of low-energy hydrogen ions.

3. After hydrogen ion implanting, the reduced QE can be completely or partially recovered by heating the photocathode. Low energy hydrogen ion implantation only causes reversible damage to photocathode, so the reduced QE can be completely recovered. In addition to the reversible damage to photocathode caused by high-energy hydrogen ion implantation, irreversible damage was also caused, so the decreased QE could only be partially recovered.

4. When the atomic gap in GaAs lattice is large, the ion channeling effect will be strengthened, thus reducing the irreversible damage caused by implanted ions to the sample. The GaAs sample with cleave plane of (110) has the largest atomic gap, so it is the least sensitive to the ion back-bombardment. On the contrary, the GaAs sample with a cleave plane of (100) is the highest sensitivity to the ion back-

bombardment. Therefore, the best choice for photogun using GaAs-based photocathodes would be surface cleave plane (110).

5. Experiments show that photocathode polarization is greatly affected by cathode temperature and doping concentration, and the relationship between them is the same as the behavior characterized by spin relaxation mechanism, that is, the higher the cathode temperature or doping concentration is, the lower the photocathode polarization is. The polarization of the GaAs photocathode with high doping concentration used in this experiment was ~30% at room temperature, while the polarization of the GaAs photocathode with low doping concentration was 50% that is above the theoretical limit at low temperature, with the actual measured value reaching 52%.

6. Photocathode polarization is sensitive to the thickness of activation layer on the photocathode surface. The increase of activation layer thickness will lead to the decrease of the polarization. At room temperature, the polarization of GaAs with high doping concentration is 36% at the initial activation stage (activation layer has only cesium). As the activation layer thickens (more cesium and NF_3 are added), the polarization decreases and eventually remains around 30%.

7. Although the crystal cleave orientation (or plane) of GaAs has a certain effect on the photocathode QE, it has no effect on the polarization.

Chapter 4 High Polarization Photocathodes

Spin-polarized electron sources play a critical role in nuclear and high energy physics research, where the spin of the electron is used to study nuclear structure, the dynamics of strong interactions, electro-weak nuclear physics, including parity-violation, and physics beyond the Standard Model. [55] Inexpensive bulk GaAs provides very high quantum efficiency (QE) but electron-spin polarization (ESP) cannot exceed 50% due to the heavy-hole, light-hole degeneracy of the 2p3/2 valence band state. [82] Photocathodes grown on a crystal structure with a different lattice constant can provide beam polarization exceeding 50% because of induced uniaxial strain that eliminates the degeneracy of the valence band. [83,84] Throughout the 1990s, single-strained-layer GaAs/GaAsP photocathodes providing polarization 75%-80% and maximum QE ~ 0.3% [85,189] were used at electron accelerators worldwide [190,191,192,193], but beam delivery using single-strained-layer photocathodes made apparent the delicate competing balance between maintaining the required degree of strain, and growing a layer thick enough to provide sufficient QE. In the following decade, strained superlattice structures consisting of very thin quantum-well active layers and alternating lattice-mismatched barrier layers were developed. [26] The superlattice structure maintained the required degree of strain to produce high polarization and provided sufficient active layer thickness to obtain higher QE. The strained GaAs/aAsP $_{0.36}$ superlattice structure reported in ref. 84 provided QE of 1.2% with polarization of 86% and is available commercially. Strained superlattice photocathodes fabricated at other facilities have also demonstrated very high polarization but no higher QE. [85,86,194]

This chapter presents two type high polarization photocathodes. In section 4.1, a commonly used strained GaAs/GaAsP superlattice photocathode is firstly introduced. The purpose of our study is enhancing the QE by adding a Distributed Bragg Reflector (DBR) into the photocathode. Then, a new type strained GaAsSb/AlGaAs superlattice photocathode is described in section 4.2.

4.1 GaAs/GaAsP Photocathode with DBR

One of the proposed Electron Ion Collider (EIC) designs, eRHIC [174], requires milliamperes of polarized electron beam representing a factor of ~ 250 beyond today's state-of-the-art. A photocathode with a QE of only 1% would require ~ 8 W of laser light (with RF structure) to generate the desired 50 mA average beam current and even more light when QE decays during operation due to ion-bombardment. In the standard strained superlattice design, most of the incident laser light simply heats the photocathode instead of promoting electron ejection, which can degrade QE due to evaporation of the chemicals used to reduce the surface work function. [195] Methods to cool the photocathode during beam delivery are complicated because the photocathode floats at high voltage. Developing photocathodes with enhanced QE could simplify the photogun design, reduce the drive-laser power requirements and prolong the effective operating lifetime of the photogun.

4.1.1 Strained GaAs/GaAsP Superlattice Structure

Growing the GaAs well layers on the GaAs1-xPx barrier layers induced uniaxial strain to the GaAs layer, which alters the band structure of the GaAs. The band structure of strained GaAs/GaAsP superlattice is shown in Figure 4-1.

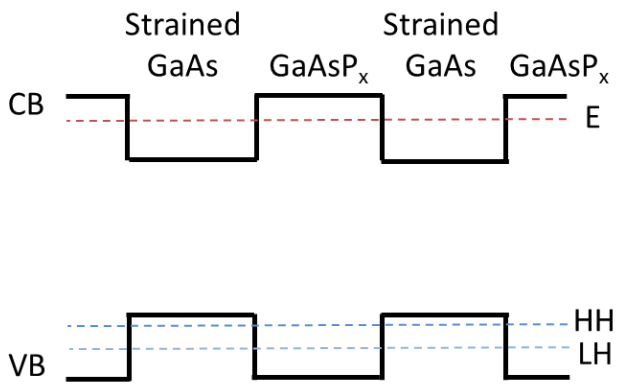

Figure 4-1: The sketch of band structure of strained GaAs/GaAsP superlattice

The strain-dependence energy gap of the heavy-hole (HH) and light-hole (LH) to the conduction band are given by: [84]

$$E^{C,HH} = E_0 + \delta E_H - \delta E_S \qquad 4\text{-}1$$

$$E^{C,LH} = E_0 + \delta E_H + \delta E_S - \frac{(\delta E_S)^2}{2\Delta_0} + \cdots \qquad 4\text{-}2$$

where E_0 is the unstrained direct band gap of GaAs (1.424 eV at room temperature) and Δ_0 is the spin-orbit splitting. The quantities δE_H and δE_S are the hydrostatic-pressure shift and uniaxial stress-induced valence-band splitting, respectively, and are given by:

$$\delta E_H = -2a\frac{C_{11}-C_{12}}{C_{11}}\epsilon \qquad 4\text{-}3$$

$$\delta E_S = -b\frac{C_{11}+2C_{12}}{C_{11}}\epsilon \qquad 4\text{-}4$$

in which the parameters a $(-9.8\,eV)$ and b $(-1.76\,eV)$ are the interband hydrostatic pressure and uniaxial deformation potentials, respectively. The C_{ij} are elastic-stiffness constants for the GaAs crystal structure $(C_{11} = 11.88 \times 10^{11} dyn/cm^2,\ C_{12} = 5.32 \times 10^{11} dyn/cm^2)$. ϵ is the lattice-mismatch, and is given by: [120]

$$\epsilon = \frac{a_0 - a}{a} \qquad 4\text{-}5$$

Where a_0 and a are the lattice constants of the GaAs and GaAs1-xPx, respectively. The lattice constant a of GaAs1-xPx can be obtained by the Vegard's law (linear interpolation): [196]

$$a(GaAs_{1-x}P_x) = a(GaAs)(1-x) + a(GaP)x = 5.6535 - 0.203x \qquad 4\text{-}6$$

The thickness of the strained layer (GaAs) must be not so thick over the critical thickness (d_c), beyond which strain relax by forming misfit dislocations, causing to degrade material quality. The critical thickness can be estimated by: [83]

$$d_c = \frac{0.224}{\epsilon}[1 + ln\left(\frac{d_c}{4}\right)] \qquad 4\text{-}7$$

From the equations above, we can know that increasing the fraction of phosphor in GaAsP can increase the lattice-mismatch and improve the strain, i.e. enlarge the energy splitting between heavy-hole and light-hole ($\delta_s = E^{C,LH} - E^{C,HH}$), leading to better polarization. However, large fraction of phosphor makes the critical thickness smaller which makes the fabrication more difficult. To obtain good polarization, our strained GaAs/aAsP $_x$ superlattice have a high fraction of phosphor of $x \approx 0.35$. For this fraction of phosphor, all the above parameters are estimated (shown in Table 4-1).

Table 4-1: Parameters for strained GaAs/ $\mathbf{GaAsP_x}$ superlattice with $\boldsymbol{x \approx 0.35}$

x	ϵ	$E^{C,HH}$	$E^{C,LH}$	δ_s	d_c
0.35	1.26%	1.5192 eV	1.6014 eV	82.2 meV	68 Å

4.1.2 Design of Photocathode with DBR Structure

A photocathode with a distributed Bragg reflector (DBR) was first proposed in 1993 [24] and reported in following years [197,198] as a means to enhance photocathode QE. The DBR serves to create a Fabry-Perot cavity formed by the front surface of photocathode and a DBR region existing beneath the superlattice active layer. Instead of a single pass in the standard design, laser light of a particular wavelength reflects repeatedly within the Fabry-Perot cavity (as shown in Figure 4-2) which increases the beneficial absorption of the incident photons, and in principle, leads to enhanced QE. It was clear that the wavelength of peak reflectivity of the DBR was very sensitive to the refractive indices and thickness of each DBR layer constituent, and that the peak of resonant absorption was very sensitive to the thickness of the photocathode, especially the spacer layer between the DBR and the superlattice photocathode structures. Accurate control of the thickness of each layer and of the composition of each constituent chemical within the photocathode structure was challenging.

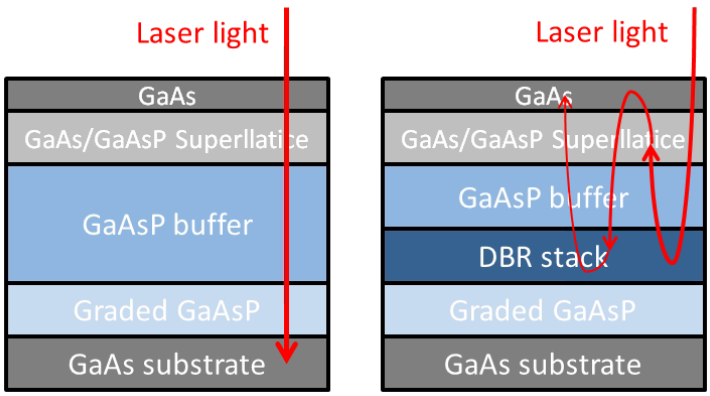

Figure 4-2: The optical transmission in the photocathodes without DBR (left) and with DBR (right)

The DBR is composed of multiple layers of alternating high and low index of refraction. A natural choice for high index of refraction layer was GaAsP which provides a good lattice match to the graded buffer layer. Though a challenge for growth, we chose AlAs1-yPy for the low index of refraction layer for maximum refractive index contrast and minimum DBR thickness. The reflectivity > 90% can be achieved around the wavelength of λ_{DBR} if the thickness of each layer coincides with the quarter wavelength condition: [24]

$$n_H(\lambda_{DBR})d_H = \frac{\lambda_{DBR}}{4} = n_L(\lambda_{DBR})d_L \qquad 4\text{-}8$$

where d_H and d_L represent the thickness of the high-refractivity and low-refractivity layers. The Fabry-Perot cavity is formed by the vacuum/GaAs cap layer interface and the DBR. Proper thickness of a GaAsP spacer layer between GaAs/GaAsP superlattice and the DBR ensures the maximum absorption in superlattice active layer coincide with the central reflective wavelength of the DBR. To design the structure, the refractive index of these layers can be estimated using a simplified interband transition model (Adachi's model used in 3.3.2) as a function of photon energy: [199]

$$n(E)^2 = A\left[f(X_0) + \frac{1}{2}\left(\frac{E_0}{E_0+\Delta_0}\right)^{\frac{3}{2}} f(X_{so})\right] + B \qquad 4\text{-}9$$

with

$$f(X_0) = X_0{}^{-2}(2 - \sqrt{1+X_0} - \sqrt{1-X_0}) \qquad 4\text{-}10$$

$$f(X_{so}) = X_{so}{}^{-2}(2 - \sqrt{1+X_{so}} - \sqrt{1-X_{so}}) \qquad 4\text{-}11$$

$$X_0 = \frac{E}{E_0} \qquad 4\text{-}12$$

$$X_{so} = \frac{E}{E_0+\Delta_0} \qquad 4\text{-}13$$

where A represents the strength parameter of the $E_0/(E_0+\Delta_0)$-gap electron transition and B represents the nondispersive contribution of the electron transitions among the higher-lying band gaps ($E_1, E_1 + \Delta_1, E_2, etc.$) for each layer. The quantities E_0 and Δ_0 are the band-gap energy and spin-orbit splitting, respectively, given by Vegard's Law for $GaAs_{1-x}P_x$: [196,200]

$$E_0(GaAs_{1-x}P_x) = (1-x)E_0(GaAs) + xE_0(GaP) - C_1x(1-x) \qquad 4\text{-}14$$

$$\Delta_0(GaAs_{1-x}P_x) = (1-x)\Delta_0(GaAs) + x\Delta_0(GaP) - C_2x(1-x) \qquad 4\text{-}15$$

where *Cn* represent the bowing parameters, which account for the deviation from a linear interpolation between GaAs and GaP, and x represents the phosphorus fraction. Similar expressions can be obtained for AlAs1-yPy. From these expressions, it can be seen that the phosphorus fraction in each layer determines the indices of refraction and the wavelength range for which the structure exhibits high reflectivity, as given by the formula: [24]

$$\Delta\lambda_{DBR} = \frac{4\lambda_{DBR}}{\pi} sin^{-1}\left(\frac{n_H(\lambda_{DBR})-n_L(\lambda_{DBR})}{n_H(\lambda_{DBR})+n_L(\lambda_{DBR})}\right) \quad 4\text{-}16$$

The desired wavelength of peak reflectivity was λ_{DBR} ~ 780 nm, compatible with CEBAF drive lasers. Setting the phosphorus fractions in the GaAs1-xPx and AlAs1-yPy layers to 0.35 and 0.4, respectively, provided refractive indices of $n_H(780nm) = 3.4506$ and $n_L(780nm) = 2.9443$. Other key parameters determined from Equations above are shown in Table 4-2. [114,200] From these parameters, the design values for the thickness of the aAsP $_{0.35}$ and $AlAsP_{0.4}$ layers were 56.5 nm and 66.5 nm, respectively. Actual layer thicknesses were very close to these design values, 54 nm and 64 nm, which set the wavelength of peak reflectivity to λ_{DBR} of 755 nm, and the reflectivity range $\Delta\lambda_{DBR}$ ~79 nm. This implies the DBR can achieve a high reflectivity > 90% for wavelengths between 715 and 795 nm.

Table 4-2: Parameters for the $\mathbf{GaAsP_x/AlAsP_y}$ DBR structure.

	E_0 (eV)	Δ_0 (eV)	n(780nm)
GaAs	1.424	0.34	3.6966+0.09i
GaP	2.752	0.08	
GaAsPx	$1.424 + 1.118x + 0.21x^2$	$0.341 - 0.336x + 0.03x^2$	3.4506+0.0006i (x=0.35)
AlAs	2.95	0.28	
AlP	3.56	0.07	
AlAsPy	$2.95 + 0.39y + 0.22y^2$	$0.28 - 0.27y$	2.9443 (y=0.4)

The final design consideration relates to the Fabry-Perot cavity formed by the front surface of photocathode and the DBR. Light at wavelength λ_R will be stored within the cavity, thereby enhancing the absorption of light, when the following resonance condition is satisfied: [24]

$$2nL = m\lambda_R \ \ (m: integer) \quad 4\text{-}17$$

where, n and L represent the refractive index and the total length of the cavity. For our case, $nL = n(GaAs) \cdot d_1 + n(SL) \cdot d_2 + n(GaAsP) \cdot d_3 + n(DBR) \cdot d_4$. Here, d_1, d_2, d_3, and d_4 are the thicknesses of the top GaAs layer, the GaAs/GaAsP superlattice structure, the intervening GaAsP layer, and the DBR layers. The wavelength spacing between neighboring resonances is given by: [24]

$$\Delta\lambda_R = \frac{\lambda_R^2}{2nL} \quad 4\text{-}18$$

Now, requiring λ_R to be equal to λ_{DBR} which was set to 780 nm and noting the many thickness parameters shown in Figure 4-3, $\Delta\lambda_R$ is roughly ~ 43 nm which provides two resonant absorption peaks near 726 nm and 776 nm, that lie within the range $\Delta\lambda_{DBR}$.

GaAs	5 nm	p=5 × 10^{19} cm^{-3}
GaAs/GaAsP SL	(3.8/2.8 nm) ×14	p=5 × 10^{17} cm^{-3}
$GaAsP_{0.35}$	2750 nm	p=5 × 10^{18} cm^{-3}
Graded $GaAsP_x$ (x = 0~0.35)	5000 nm	p=5 × 10^{18} cm^{-3}
GaAs buffer	200 nm	p=2 × 10^{18} cm^{-3}
p-GaAs substrate (p>10^{18} cm^{-3})		

GaAs	5 nm	p=5 × 10^{19} cm^{-3}
GaAs/GaAsP SL	(3.8/2.8 nm) ×14	p=5 · 10^{17} cm^{-3}
$GaAsP_{0.35}$	750 nm	p=5 × 10^{18} cm^{-3}
$GaAsP_{0.35}$/ $AlAsP_{0.4}$ DBR	(54/64 nm) ×12	p=5 × 10^{18} cm^{-3}
$GaAsP_{0.35}$	2000 nm	p=5 × 10^{18} cm^{-3}
Graded $GaAsP_x$ (x = 0~0.35)	5000 nm	p=5 × 10^{18} cm^{-3}
GaAs buffer	200 nm	p=2 × 10^{18} cm^{-3}
p-GaAs substrate (p>10^{18} cm^{-3})		

Figure 4-3: Schematic structure of the photocathodes: without DBR (left) and with DBR (right).

The transfer matrix method normally used to calculate the reflection and transmission of incident light through a stack of multilayer thin films was used to calculate the absorption of incident photos inside the Fabry-Perot cavity. The transfer matrix of the photocathode illuminated with light at normal incidence is given by: [201,202]

$$M = \begin{bmatrix} M_{11} & M_{12} \\ M_{21} & M_{22} \end{bmatrix} = J_{m-1\to m} F_{m-1} \cdots F_2 J_{1\to 2} F_1 J_{0\to 1} \qquad 4\text{-}19$$

with

$$J_{i\to i+1} = \begin{bmatrix} \frac{k_{i+1}+k_i}{2k_{i+1}} & \frac{k_{i+1}-k_i}{2k_{i+1}} \\ \frac{k_{i+1}-k_i}{2k_{i+1}} & \frac{k_{i+1}+k_i}{2k_{i+1}} \end{bmatrix} \qquad 4\text{-}20$$

$$F_i = \begin{bmatrix} e^{ik_i d_i} & 0 \\ 0 & e^{-ik_i d_i} \end{bmatrix} \qquad 4\text{-}21$$

where, k_i is the wave number of layer i. For example, i=0 represents vacuum and $k_0 = 2\pi/\lambda$; layer i=1 represents the first GaAs layer of thickness $5nm$ and $k_1 = 2\pi n(GaAs)/\lambda$, and so on until final layer 16 representing the buffer layer. The surface reflectivity R, the transmittance into GaAs substrate T, and the absorption in the Fabry-Perot cavity A can be obtained by:

$$R = \left| -\frac{M_{21}}{M_{22}} \right|^2 \qquad 4\text{-}22$$

$$T = \left| M_{11} - \frac{M_{12}M_{21}}{M_{22}} \right|^2 \cdot \frac{n_m}{n_0} \qquad 4\text{-}23$$

$$A = 1 - R - T \qquad 4\text{-}24$$

The surface reflectivity of $aAsP_{0.35}$/$AlAsP_{0.4}$ DBR with central wavelength $\lambda_{DBR} = 755\ nm$ is calculated for different number of pairs and shown in Figure 4-4. Increasing the number of $aAsP_{0.35}$/$AlAsP_{0.4}$pairs enhanced the surface reflectivity. The surface reflectivity at central wavelength for n=12 reached to 93.2% that is as high as required value.

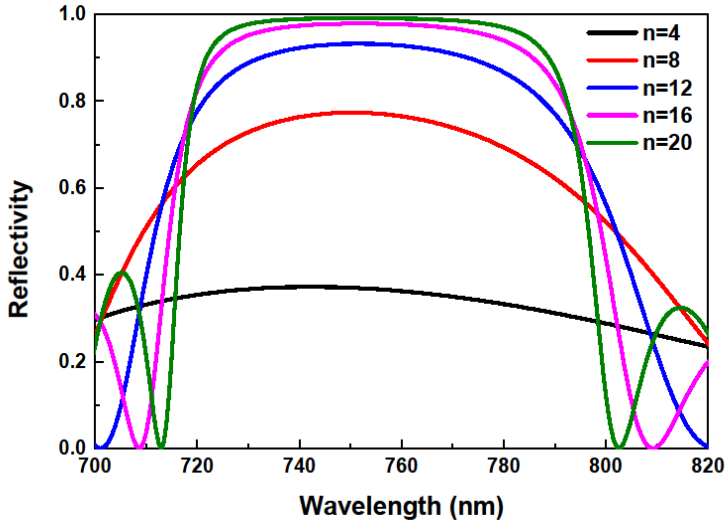

Figure 4-4: The surface reflectivity of $\mathbf{GaAsP_{0.35}/AlAsP_{0.4}}$DBR for different number of pairs from 4 to 20

Calculated values of reflectivity (R), transmittance (T) into the GaAs substrate, absorption (A) of photocathodes (not including the GaAs substrate) and the absorption enhancement factor as a function of wavelength, are shown in Figure 4-5. As expected, there are two resonant absorption peaks for the DBR photocathode at wavelengths 726 nm and 776 nm. The resonant peak at 776 nm is just 4 nm from the desired value 780 nm. This does not pose a problem for operation at CEBAF because the drive laser wavelength can be shifted this small amount. At 776 nm, the absorption is 21.03%, surface reflectivity is 50.14%, and transmittance into GaAs substrate is 28.83% for the DBR photocathode, corresponding to maximum electron spin polarization. The full-width half-maximum of the Fabry-Perot resonance is about 10 nm at 776nm. The absorption enhancement factor is 7.4 at this wavelength.

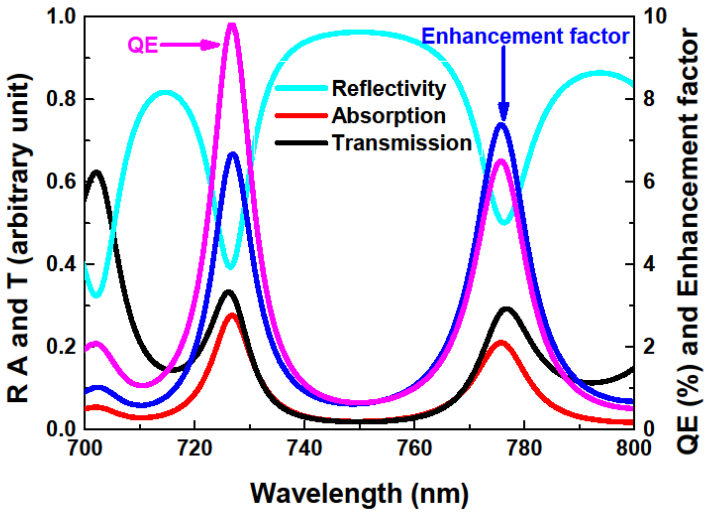

Figure 4-5: Calculated values of absorption, reflectivity and transmittance of the DBR photocathode, as a function of wavelength. Also shown, calculated QE and the enhancement factor compared to the photocathode without the DBR.

To estimate the quantum efficiency of photocathode, one can solve the one-dimensional diffusion equations, based on Spicer's three-step model: [86,194]

$$QE(\lambda) = \frac{P_L F_L A}{1+\frac{1}{\alpha_\lambda L_L}} + \frac{P_\Gamma exp[k(-\frac{1}{1.42}-\frac{\lambda}{1240})]A}{1+\frac{1}{\alpha_\lambda L_\Gamma}}[F_\Gamma + \frac{F_L L_\Gamma}{\alpha_\lambda F_L (L_\Gamma + L_L)(1+\frac{1}{\alpha_\lambda L_L})}] \quad 4\text{-}25$$

where P_Γ and P_L are the surface electron escape probabilities for the Γ and L minima, respectively, which are independent of the incident photon energy, F_Γ is the fraction of excited electrons remaining in the Γ minima, F_L is the fraction of electrons that is excited to energies greater than the L minima, A is the absorption of photocathode, L_Γ and L_L are the electron diffusion length for the Γ and L minima, respectively, α_λ is the absorption coefficient of the photocathode, and k is a coefficient ($k \geq 0$). The calculated QE for the DBR photocathode, together with the QE enhancement factor as a function of wavelength, are shown in Figure 4-5.

4.1.3 Results and Discussion

All photocathodes were grown in a solid-source molecular beam epitaxy (SSMBE) system equipped with As and P crackers on a (100) p-type GaAs substrate, upon which a 200 nm Be-doped ($2 \times 10^{18}\ cm^{-3}$) GaAs buffer layer was deposited. The 5-µm-thick Be-doped graded aAsP $_x$ layer was then grown with an increasing P composition from x=0 to 0.35, followed by a 2-µm-thick a $As_{0.65}P_{0.35}$ layer, in order to produce a strain-relaxed a $As_{0.65}P_{0.35}$ layer compatible with the superlattice active layer. The DBR structure consisting of 12-pair of a $As_{0.65}P_{0.35}$ (54 nm)/$AlAs_{0.6}P_{0.4}$ (64 nm) was subsequently grown on top of this layer. In order to create an effective Fabry-Perot resonant cavity for the desired wavelength near 780nm, a 750-nm-thick a $As_{0.65}P_{0.35}$ layer was grown on top of DBR acting as a spacer. Both a $As_{0.65}P_{0.35}$ and DBR layers were Be-doped at $5 \times 10^{18}\ cm^{-3}$ to promote high electrical conductivity. The p-type ($2 \times 10^{17}\ cm^{-3}$) GaAs (3.8 nm)/ a $As_{0.65}P_{0.35}$ (2.8 nm) superlattice layer was positioned between the a $As_{0.65}P_{0.35}$ spacer and the 5-nm-thick GaAs cap layer doped at p=$2 \times 10^{19}\ cm^{-3}$. The only difference between the DBR photocathode and the non-DBR photocathode was the 12-pairs of a $As_{0.65}P_{0.35}$ (54 nm)/ $AlAs_{0.6}P_{0.4}$ (64 nm) layers.

The growth of a $As_{0.65}P_{0.35}$/ $AlAs_{0.6}P_{0.4}$ DBR structure was very challenging due to the large differences in growth temperatures and the V/III flux ratios for the a $As_{0.65}P_{0.35}$ and $AlAs_{0.6}P_{0.4}$ layers. The optimal growth temperatures for a $As_{0.65}P_{0.35}$ and $AlAs_{0.6}P_{0.4}$ were 660-700 °C and 700-750 °C, respectively, as determined by surface temperature measurement and reflective high energy electron diffraction (RHEED) images during MBE growth. Thicknesses and composition were verified using x-ray diffraction measurements and x-ray simulation models. It was very difficult to accurately control the growth rate of a $As_{0.65}P_{0.35}$ at high temperatures, especially approaching 700 °C, because the re-evaporation rate of Ga atoms from the sample surface increases rapidly with increasing growth temperatures above 660 °C, resulting in inconsistent control of the layer thickness. Additionally, maintaining the As/P fraction in a $As_{0.65}P_{0.35}$ layers is difficult when grown below 650 °C, as the As/P

fraction is very sensitive at low growth temperatures. [203,204] For these reasons the thick graded composition GaAsP was grown at 660 °C. However, the material quality of $AlAs_{0.6}P_{0.4}$ layer was poor when grown at this temperature. Therefore, the growth temperature of a $As_{0.65}P_{0.35}$/ $AlAs_{0.6}P_{0.4}$ DBR had to be kept at 700 °C as measured by an SVT AccuTemp process monitor using a two-color infrared pyrometer. The large difference in V/III flux ratio during the growth between a $As_{0.65}P_{0.35}$ and $AlAs_{0.6}P_{0.4}$ added extra difficulty to achieving high quality DBR layers. The V/III ratio for a $As_{0.65}P_{0.35}$ is around 50, whereas the ratio is only around 3 for $AlAs_{0.6}P_{0.4}$. Numerous growth-calibration and material-characterization runs were required to develop suitable substrate temperature and source-switching recipes to enable the fabrication of high quality a $As_{0.65}P_{0.35}$/ $AlAs_{0.6}P_{0.4}$ DBR and strained-superlattice structures grown by SSMBE.

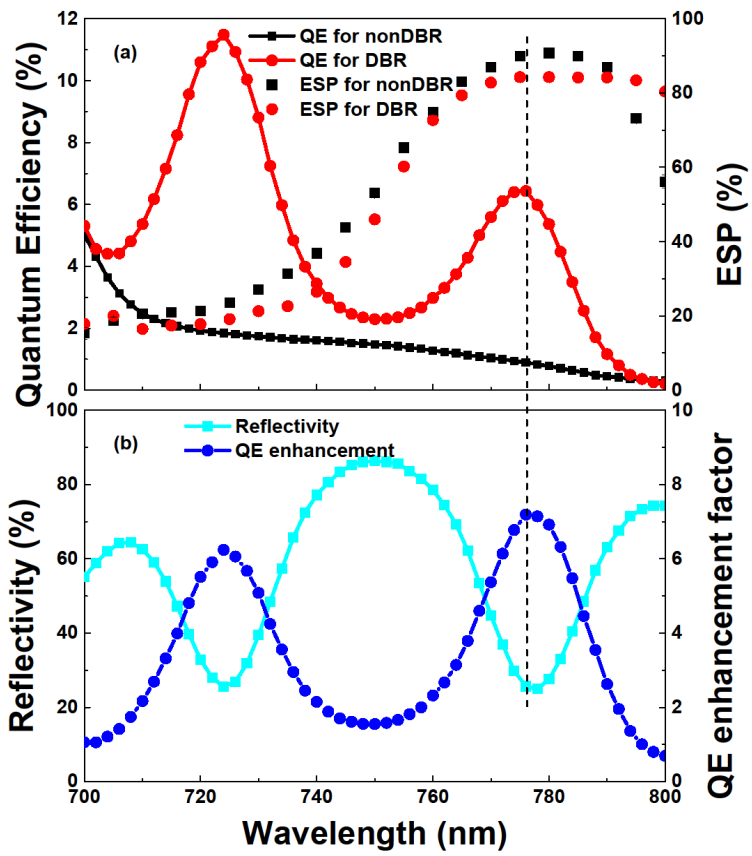

Figure 4-6: (a) The QE and electron-spin polarization (ESP) for the strained GaAs/GaAsP superlattice photocathodes with and without DBR as a function of the wavelength; (b) Reflectivity and QE enhancement factor of DBR photocathode as a function of the wavelength. The dash line indicates the resonant position.

Measured values of QE and polarization as a function of wavelength, for photocathodes with and without DBR, are shown in Figure 4-6 (a). For the non-DBR photocathode, results are consistent with past work [28] indicating peak polarization of 90% and QE of 0.89% at a wavelength ~ 780 nm. In stark contrast, the QE of the DBR photocathode shows the telltale prominent oscillatory behavior indicative of resonant absorption. Measured reflectivity and QE enhancement (i.e., the ratio of QE

values of photocathodes with and without DBR) are shown in Figure 4-6 (b). The two dips in the reflectivity spectrum are clearly correlated with wavelength locations of QE maxima. At the wavelength of interest, 776 nm, the QE was 6.4% and polarization ~ 84%. The measured QE enhancement of ~ 7.2 is very close to the predicted value of ~7.4. It should be noted that QE enhancement is a somewhat arbitrary metric dependent on when measurements were made following photocathode activation and subject to non-trivial variations in QE associated with vacuum conditions that influence photocathode lifetime.

These results are compared to results from other photocathodes listed in Table 4-3, showing QE, polarization and photocathode Figure of Merit (P^2QE). The Figure of Merit of our photocathode is a factor of four higher than the last highest value. In conclusion, a QE of 6.4% is the highest reported value of any "high polarization" photocathode. Precise control of the thickness of each layer and the composition of each constituent led to these improved results. Further optimization should lead to even higher QE, and polarization values approaching the best values from superlattice photocathodes without DBR structures.

Table 4-3: Figure of merit for polarized electron sources

Cathode	Ref.	P (%)	QE (%)	(P^2QE) (%)
GaAs/aAsP $_{0.36}$ (no DBR)	SLAC/SVT [28]	86	1.2	0.89
GaAs/aAsP $_{0.38}$ (no DBR)	Nagoya [86]	92	1.6	1.35
$Al_{0.19}In_{0.2}aAs$ /$Al_{0.4}aAs$ (with DBR)	St. Peterburg [31]	92	0.85	0.72
GaAs/aAsP $_{0.35}$ (with DBR)	JLab/SVT	84	6.4	4.52

4.2 GaAsSb/AlGaAs Photocathode

The theoretical analysis and numerical calculation show that GaAsSb/AlGaAs heterostructure has the largest valence band offset among all the GaAs-based heterostructures which include InGaAs/AlGaAs, InGaAs/GaAs, GaAs/GaAsP, and GaAsSb/AlGaAs. The large valence band offset of GaAsSb/AlGaAs heterostructure results in large splitting energy (δ) between Heavy-hole (HH) and Light-hole (LH) bands in the GaAsSb/AlGaAs strained superlattice (SSL) and therefore leads to high initial ESP. For example, the HH-LH splitting energy is as high as 131.7 meV for the a $As_{0.853}Sb_{0.147}/Al_{0.38}a_{0.62}As$ (1.2/2.4 nm ×10) SSL photocathode, which is the highest predicted splitting energy for any SSL photocathode.

4.2.1 GaAsSb/AlGaAs SSL Structure

Growing the a $As_{1-x}Sb_x$ well layers between the $Al_ya_{1-y}As$ barrier layers induced biaxial strain to the a $As_{1-x}Sb_x$ layer, forming a $As_{1-x}Sb_x/Al_ya_{1-y}As$ SSL, which altered the band structure of the a $As_{1-x}Sb_x$. The a $As_{1-x}Sb_x/Al_ya_{1-y}As$ SL layer positioned between the $Al_ya_{1-y}As$ spacer and the GaAs cap layer. The schematic structure of the SSL photocathode is shown in Figure 4-7.

GaAs	5 nm	p=5 × 10^{19} cm^{-3}
Ga_xAsSb/Al_yGaAs SL	(d_1/d_2) × N	p=5 × 10^{17} cm^{-3}
Al_yGaAs	250 nm	p=5 × 10^{18} cm^{-3}
GaAs buffer	200 nm	p=7 × 10^{18} cm^{-3}
p-GaAs substrate (p>5 × 10^{17} cm^{-3})		

Figure 4-7: The schematic structure of the SSL photocathode

The Luttinger-Kohn Hamiltonian (A flavor of the $\boldsymbol{k} \cdot \boldsymbol{p}$ model used for calculating the structure of multiple, degenerate electronic bands in bulk and quantum well semiconductors) taking into account the strain effects (or called Pikus-Bir Hamiltonian [205]) was used to estimate the band structure of the SSL photocathode. [206] The general Hamiltonian is described in terms of 4×4 matrix, which considers the heavy-hole band and light-hole band mixings. [207] The 4×4 Hamiltonian can be treated as block diagonalized. For a quantum well with strain, the structure does not have inversion symmetry, thus both upper and lower Hamiltonians are required to solve. Since the upper and lower Hamiltonians are degenerate, only a 2×2 matrix is required for each block of the Hamiltonian. For a symmetric quantum well without strain, the solutions for both Hamiltonian are degenerate, thus only a 2×2 Hamiltonian is required to solve to find the energy.

The estimated flat band structure of a SSL photocathode and the band structure along the $\vec{\boldsymbol{k}}$ axis of the SSL are shown in Figure 4-8. The structure of the photocathode used to calculate the band structure is shown in Figure 4-7, in which the component of the superlattice is aAsSb $_{0.147}$/$Al_{0.38}$aAs (1.2/2.4 nm ×10). The aAsSb $_{0.147}$ layer is quantum well layer and the $Al_{0.38}$aAs layer is barrier layer. The aAsSb $_{0.147}$/$Al_{0.38}$aAs SSL was grown on the $Al_{0.38}$aAs spacer layer. The strain occurred for the quantum well layer, but not for the barrier layer. The compression strain of the quantum well layer made its heavy-hole band shifted above the light-hole band. The splitting energy of the heavy-hole and light-hole band was 131.7 meV. The band was bent at the interface of each component due to their dopant concentration are different. The bandgap of the aAsSb $_{0.147}$/$Al_{0.38}$aAs (1.2/2.4 nm ×10) SSL at $\vec{k} = 0$ (Γ point) is 1.602 eV, corresponding to 774 nm of laser wavelength.

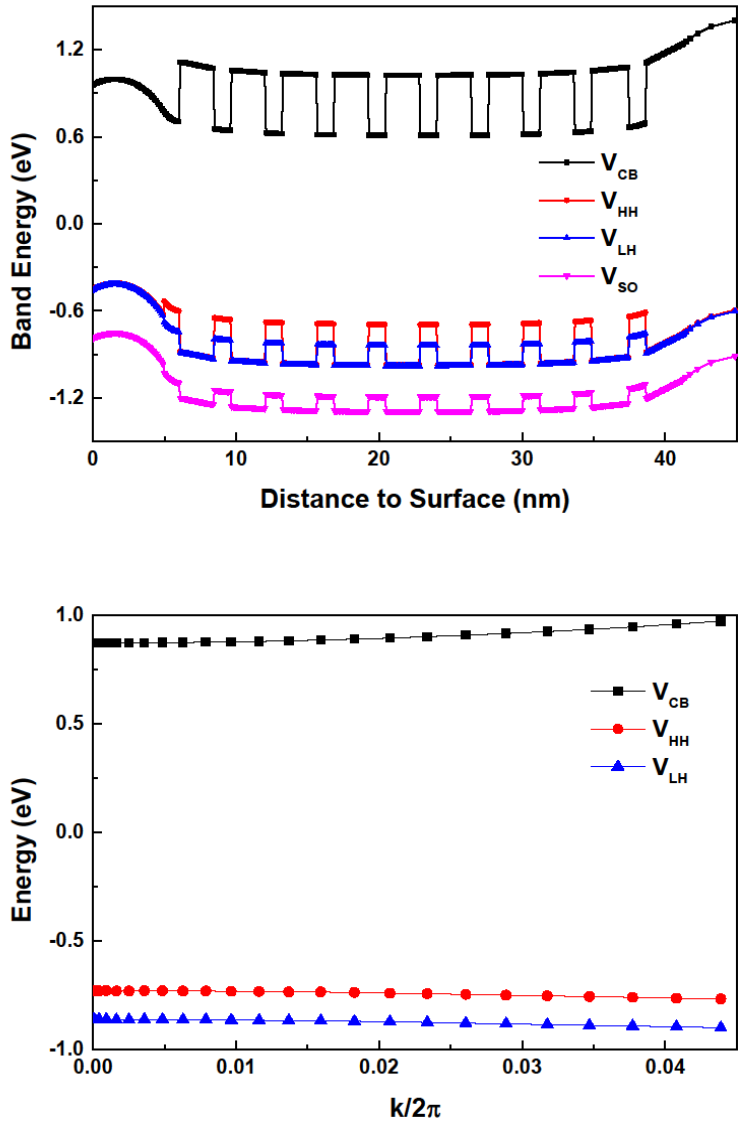

Figure 4-8: (up) The Flat band structure of a $\mathbf{GaAsSb_{0.147}/Al_{0.38}GaAs}$ (1.2/2.4 nm ×10) strained superlattice (SSL) photocathode and (down) band structure along the $\vec{k}$ axis of the strained $\mathbf{GaAsSb_{0.147}/Al_{0.38}GaAs}$ (1.2/2.4 nm ×10) SL. The SL bandgap is 1.602 eV, and the HH-LH splitting energy is 131.7 meV.

The bandgap and HH-LH splitting energy of strained a $As_{1-x}Sb_x/Al_ya_{1-y}As$ (1.2/2.4 nm ×10) SL as function of the fraction (x) of Sb in a $As_{1-x}Sb_x$ and the fraction (y) of Al in $Al_ya_{1-y}As$ are shown in Figure 4-9. The red lines present the bandgap and splitting energy at different fraction of Sb in a $As_{1-x}Sb_x$ with fixed fraction of Al in $Al_ya_{1-y}As$ (y=0.38), and the blue lines present the bandgap and splitting energy at different fraction of Al in $Al_ya_{1-y}As$ with fixed fraction of Sb in a $As_{1-x}Sb_x$ (x=0.15). The fraction of Sb in a $As_{1-x}Sb_x$ has a strong effect on the bandgap and splitting energy. Increasing the fraction of Sb reduced the bandgap but enlarged the splitting energy of SL strongly. However, the fraction of Al in $Al_ya_{1-y}As$ doesn't have so strong effect on the bandgap and splitting energy. When the fraction of Al is smaller than 0.33, the bandgap extended as increase of the fraction

of Al, and then the bandgap almost has no change as the fraction of Al increase from 0.33 to 0.4. The splitting energy decrease slightly as the fraction of Al increase from 0.3 to 0.4.

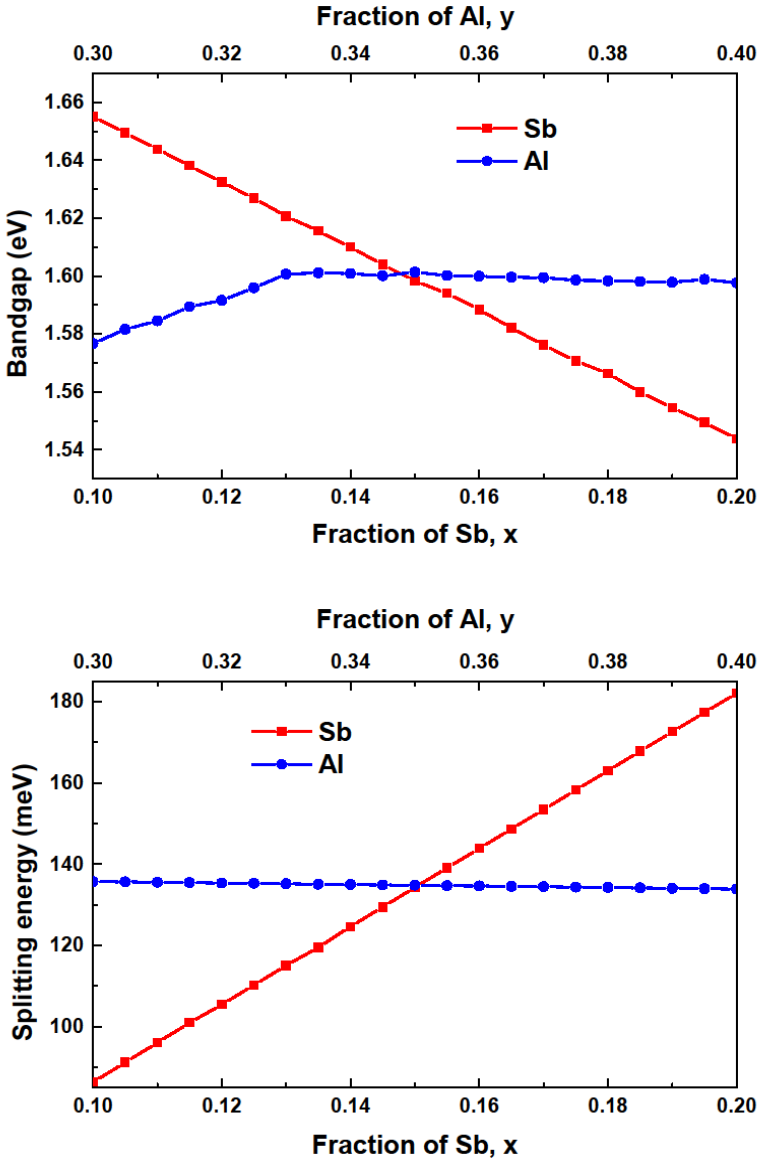

Figure 4-9: The bandgap (up) and HH-LH splitting energy (down) of strained $\mathbf{GaAs_{1-x}Sb_x}$/ $\mathbf{Al_yGa_{1-y}As}$ (1.2/2.4 nm ×10) SL as function of the fraction (x) of Sb in $\mathbf{GaAs_{1-x}Sb_x}$ (red line, y=0.38) and the fraction (y) of Al in $\mathbf{Al_yGa_{1-y}As}$ (blue line, x=0.15)

4.2.2 Results and Discussion

All photocathodes were grown in a solid-source molecular beam epitaxy (SSMBE) system equipped with Sb, Al and As crackers on a (100) p-type GaAs substrate (doping concentration $> 5 \times 10^{17}\ cm^{-3}$), upon which a 200 nm Be-doped ($7 \times 10^{18}\ cm^{-3}$) GaAs buffer layer was deposited. In order to produce a strain-relaxed layer compatible with the SL active layer, then a 250 nm Be-doped ($5 \times 10^{18}\ cm^{-3}$) $Al_ya_{1-y}As$ layer was grown upon the buffer. The p-type ($5 \times 10^{17}\ cm^{-3}$) a $As_{1-x}Sb_x/Al_ya_{1-y}As$ SL layer was positioned on the $Al_ya_{1-y}As$ layer. Finally, in order to

improve the photoemission (or the escape probability of electrons), a 5-nm-thick very high p-doped ($5 \times 10^{19}\ cm^{-3}$) GaAs was positioned on the top of photocathodes to help to form NEA surface.

Table 4-4: The QE and ESP at 780 nm and the maximum ESP with corresponding QE for five photocathode samples together with the SL structures of samples

Sample No.	Parameters of SL	ESP at 780 nm (%)	QE at 780 nm (%)	Max ESP & λ	QE at max Pol (%)
1	aAs $Sb_{0.173}/Al_{0.4}aAs$ 1.2/4 nm 20SL	68.9	0.066	73.1% 790 nm	0.041
2	aAs $Sb_{0.165}/Al_{0.4}aAs$ 1.2/4 nm 20SL	73.9	0.27	73.9% 780 nm	0.27
3	aAs $Sb_{0.15}/Al_{0.36}aAs$ 1.5/4 nm 15SL	70.1	0.61	76.7% 795 nm	0.33
4	aAs $Sb_{0.147}/Al_{0.38}aAs$ 1.2/2.4 nm 30SL	74.8	0.62	74.8% 780 nm	0.62
5	aAs $Sb_{0.115}/Al_{0.38}aAs$ 1.2/2.4 nm 30SL	45.4	0.29	75.6% 750 nm	0.46

Five photocathode samples with different SL structures (shown in Table 4-4) were fabricated and evaluated in the mini-Mott chamber. The measured values of QE and electron spin polarization (ESP) and maximum ESP with corresponding QE for five photocathode samples are shown in Table 4-4. The sample No. 4 has the best results among all the samples, which exhibits the highest ESP of 74.8% corresponding to ~780 nm (a wavelength compatible with CEBAF photo-gun drive lasers) with QE of 0.62%. The QE and ESP for the sample No. 4 as a function of wavelength is shown in Figure 4-10.

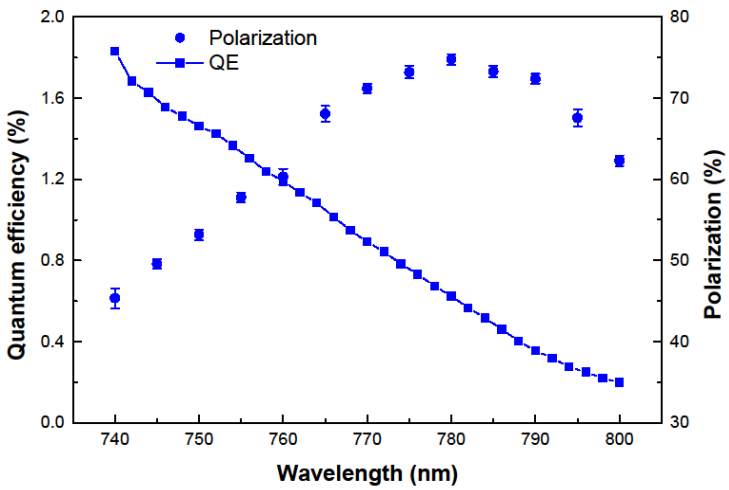

Figure 4-10: The QE and ESP for sample No.4: $\mathbf{GaAsSb_{0.147}/Al_{0.38}GaAs}$ (1.2/2.4 nm 30 SL) as a function of wavelength

In summary, the component and thickness of quantum well layer and barrier layer in SL determine the band structure of photocathode, which determines the QE and ESP obtained from the photocathode. The fraction of Sb in a $As_{1-x}Sb_x$ (quantum well layer) has a strong effect on the bandgap, which determines the wavelength (or photon energy) corresponding to the maximum electron spin polarization of photocathode, and the HH-LH splitting energy, which influence on the maximum electron spin

polarization and the wavelength region for the maximum electron spin polarization of photocathode. The fraction of Al in $Al_y a_{1-y}As$ has a slightly effect on the bandgap and the HH-LH splitting energy. Our samples exhibit high ESP over 70% with a best QE of 0.62%, and the splitting energy is smaller than 100 meV. The experimental results are not as good as expected, which can be explained as follows:

1) The band structure simulated by the **k · p** model used in this study is not very accurate, and the bandwidths of light-hole and heavy-hole bands are not considered in this model. Therefore, we cannot learn the separation between light-hole and heavy-hole bands. If the light-hole and heavy-hole bands (as shown in Figure 4-11(a)) are completely separated, the initial polarization of electrons generated by the SSL structure will reach 100%. On the other hand, if the light-hole and heavy-hole bands (as shown in Figure 4-11 (b)) are not completely separated, the initial polarization of electrons generated by the SSL structure is low. The strained layer in GaAs/GaAsP SSL is GaAs, and the strained layer in GaAsSb/AlGaAs SSL is GaAsSb. We speculate that the bandwidth of light-hole and heavy-hole bands of GaAsSb is larger than that of GaAs. Therefore, although the splitting energy between light-hole and heavy-hole bands in GaAsSb/AlGaAs is higher than that in GaAs/GaAsP, but the splitting degree is lower than that in GaAs/GaAsP. Thus, the initial polarization of electrons generated by GaAsSb/AlGaAs SSL is lower than that of GaAs/GaAsP SSL, and the peak range of polarization is relatively smaller. As a result, the polarization of electrons generated by GaAsSb/AlGaAs SSL is not as ideal as expected.

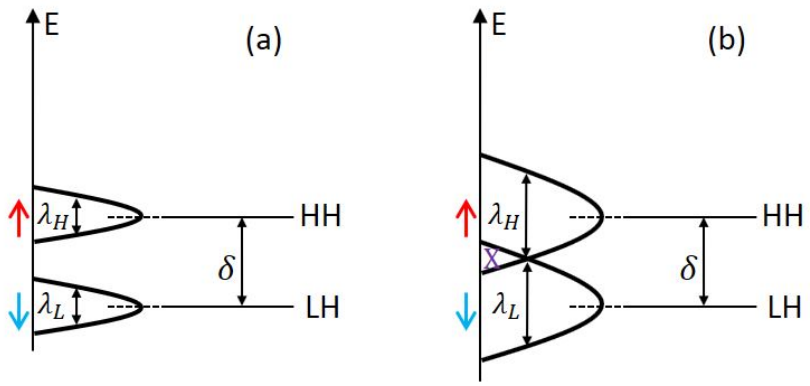

Figure 4-11: The separation of light-hole and heavy-hole bands of the SSL structure. (a) The light-hole and heavy-hole bands are completely separated under the perfect condition that the strain is large and the bandwidths of light-hole and heavy-hole bands are small. (b) The light-hole and heavy-hole bands are not completely separated under the imperfect condition that the strain is small or the bandwidths of light-hole and heavy-hole bands are big.

2) Until now, the manufacture technology of GaAsSb/AlGaAs SSL structure is not mature, and manufactured samples are different from the theoretical design in terms of the parameters such as sample composition and layer thickness. The band structure of SSL is very sensitive to these parameters, especially Sb content in GaAsSb. Therefore, there may be a large deviation between the band structure

of the experimental sample and the theoretical design, resulting in the experimental results are not as good as expected.

According to the above-mentioned reasons and analysis, the future research work about the GaAsSb/AlGaAs SSL photocathode can make further efforts in the following aspects: firstly, optimize the simulation program to obtain more accurate band structure and more important to get the bandwidths of light-hole and heavy-hole bands, which can more accurately evaluate the polarization of electrons generated by the GaAsSb/AlGaAs SSL photocathode. At the same time, other GaAs-based SSL structures can be simulated, in order to obtain more ideal SSL structures that can be used to generate high polarization electrons. On the other hand, optimize the structure and manufacture method for the GaAsSb/AlGaAs SSL photocathodes to obtain higher QE and polarization.

4.3 Generation of high-current polarized electron beam

The CEBAF at JLab was built since 1987 and began to be used for nuclear and high-energy physics experiments in 1995. Until now, the upgraded CEBAF (as shown in Figure 4-12) can provide an electron beam with spin polarization of more than 85%, beam current of up to 200 μA (or charge lifetime of 200 C), beam energy of up to 12 GeV, beam emittance of less than 1mm-mrad, and energy spread ΔE/E of less than 2×10^{-5}. The RF frequency of the accelerating superconducting cavity is 1497 MHz. [153,158,208] The accelerator facility consists of two identical superconducting linear acceleration modules and magnetic transfer devices. The arc-shaped deflection magnetic transmission device enables the electron beam to be passed through the linear acceleration modules and to be accelerated for five times, and finally a polarized electron beam with energy of greater than 12GeV can be obtained.

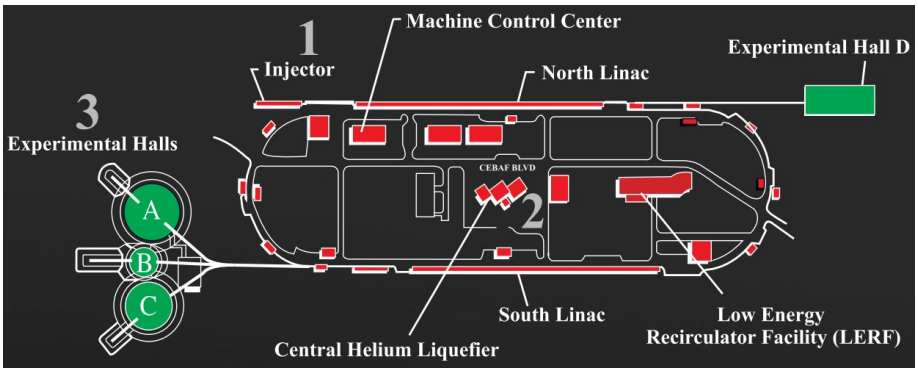

Figure 4-12: The layout of CEBAF at JLab

CEBAF starts with a polarized photogun that is one of the most important subsystems of CEBAF, and the electron beam quality provided by CEBAF depends largely on the characteristics of the photogun. Over the years, in order to meet the different physical experimental requirements, the polarized photogun of CEBAF has undergone several upgrades and modifications. This section will briefly review the development history and present situation of the CEBAF polarized photogun, and

then introduce the preparation of generating high-current polarized electron beam using the Upgraded Injector Test Facility (UITF) at JLab.

4.3.1 The development and present situation of CEBAF polarized photogun

The first CEBAF polarized electron source was a 100 kV DC photogun (as shown in Figure 4-13) that was developed by JLab in collaboration with the university of Illinois. The beam axis of the photogun was vertical. The electron beam emitted by the photocathode was deflected into the horizontal direction by an 72° sector dipole. The electron-spin orientation was controlled by a "Z" style spin manipulator composed of a pair of 107.7° double-focusing electrostatic bends and eight solenoid lenses.

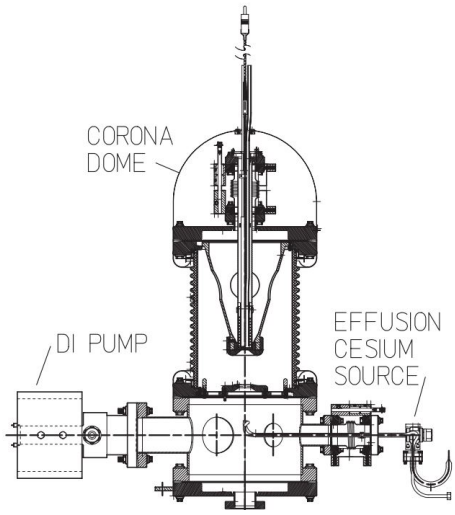

Figure 4-13: The first polarized photogun at JLab

The first polarized photogun used bulk GaAs as photocathode that was pumped by a master-oscillator power amplifier (MOPA) diode laser with optical pulse frequency of 1497 MHz, which produced an electron beam with average beam current of 30 μA (maximum current sup to 140 μA). The measured beam transmission between the photogun and the experimental hall was ~70% at high average current, and the beam losses were in the chopper slits and the two-aperture emittance filter located before the chopper. It was observed that the vacuum pressure in photogun increased dramatically when the average beam current was increased, leading to shorter operating lifetime of photogun and thus the photocathode needs to be reactivated or changed frequently.

In order to eliminate or reduce the impact of the shortcomings of the first photogun during operating at high current operation, JLab developed the second photogun (as shown in Figure 4-14). The Wien filter and solenoid were used to replace the "Z" style spin manipulator to remove the majority of the short focal length elements. [21] The NEG pump was introduced into the photogun to improve the vacuum of electron gun. The 1497 MHz MOPA laser was replaced by a set of three 499 MHz MOPA lasers, thus providing an independent laser for each experimental hall. The BPM (Beam Position Monitor) was added to monitor the electron beam, helping to improve the reproducibility and reduce the setup time of the injector optics. Finally, a process is developed to make only a specific area on the

photocathode surface be activated and emit electrons, thus eliminating photoemission from the large-radius areas of photocathode.

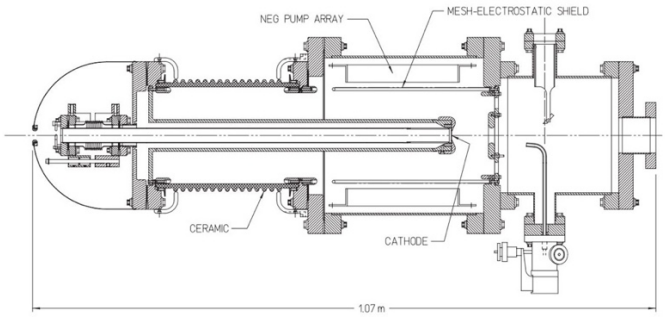

Figure 4-14: The second polarized photogun at JLab

The second polarized photogun began delivery electron beam for CEBAF in February of 1998. A series of physical experiments were supported by this photogun after its installation, the most important of which was the measurement of parity-violation in electron scattering. [209] A bulk GaAs photocathode was used to provide polarized electrons for this parity-violation experiment. Following that experiment, the strained GaAs was introduced to provide electron beam with higher polarization.

The third polarized electron source was modified and upgraded from the second photogun. Its main changes are to remove the few remaining short focal length elements and to make further vacuum improvement. After removing these short focal length elements, the possibility of bending the electron beam from vertical to the horizontal was eliminated. So that, the gun was mounted in the horizontal plane with a 15° bending magnet that deflected the electron beam onto the injector axis. The vacuum was improved by enlarging the diameter of the beam tube between the photogun and the bending magnet chamber and depositing a non-evaporative getter film on the inner wall of these beam tubes. [210] The third polarized electron source, with two horizontally mounted photoguns (as shown in Figure 4-15), began successfully providing the electron beam to CEBAF in 1999.

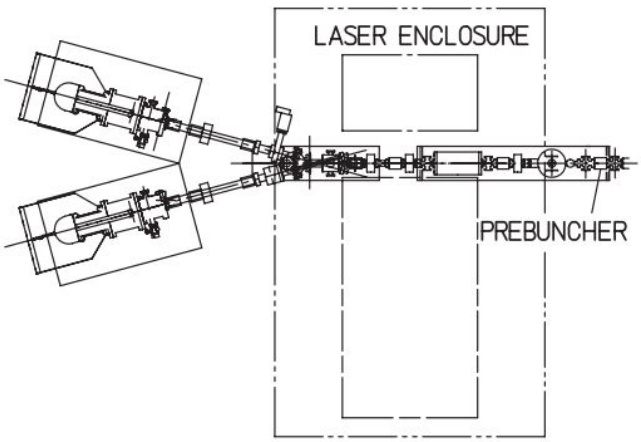

Figure 4-15: The third polarized electron source at JLab

Both bulk GaAs, single strained GaAs and strained superlattice were used for third polarized electron source to generate polarized electron beam, and the quality of polarized electron beam was improved continuously. The strained superlattice photocathode from SVT Associates was in constant use in the third polarized electron source between September, 2005 and April, 2007, which provide beam current up to 200 μA and polarization of 85%. Over this period, this electron source provided the electron charges of ~1000 C using the SSL photocathode. [211]

In order to further improve the vacuum to prolong the operating lifetime of photogun, JLab developed a new load-locked photogun, the fourth polarized electron source (as shown in Figure 4-16), which successfully provided the polarized electron beam to CEBAF in 2007. [212,213] The load-locked photogun consisted of four chambers separated by UHV all-metal vacuum gate valves: a portable "suitcase" chamber, a loading chamber, a photocathode preparation chamber and a high voltage (HV) chamber. The best vacuum was obtained in the HV chamber where the photocathode produces the beam current. Different from the traditional photogun, the installation, preparation and work of the photocathode sample were performed in different chambers, which was conducive to maintaining the vacuum in the HV chamber and reducing the time of changing photocathodes in the HV chamber. The photocathode sample was firstly introduced into the portable "suitcase" chamber (10^{-9} Torr) using a nitrogen filled glove bag and then transported and mated to the loading chamber (10^{-9} Torr). Then the photocathode was introduced into the preparation chamber (10^{-10} Torr) where the photocathode will be activated. Finally, the activated photocathode was quickly inserted into the cathode electrode in the HV chamber (10^{-11} Torr). The gate valve between each chamber was briefly opened during photocathode transportation and closed for the rest time to maintain the vacuum in each chamber. In addition, the photogun can accommodate four photocathode samples at the same time, i.e., four different samples can be introduced into the photogun each time the chamber is opened, which greatly reduced downtime associated with photocathode replacement, thereby enhancing the operating lifetime of the photogun.

The improvement of vacuum of the load-locked photogun is difficult to be measured directly, but the enhanced operating lifetime indicates that the load-locked photogun has better vacuum conditions. The test results shows that the load-locked photogun improved the charge lifetime by a factor between 2 and 3. Using bulk GaAs photocathodes, the load-locked photogun provided charge lifetimes over 2000C with (unpolarized electron) beam current from 1 to 7 mA for large spot (diameter: 1.5 mm) laser (wavelength: 532 nm) illuminating and also provided charge lifetimes over 1000C with (unpolarized electron) beam current less than 1 mA for small spot(diameter: 0.32mm) laser illuminating. Using SSL GaAs photocathodes, the load-locked photogun provided (polarized electron) beam current of 250 μA to 1 mA with charge lifetime of ~200 C for small spot (diameter 0.45 mm) laser (wavelength: 780 nm) illuminating. Although the load-locked photogun performed very well during commissioning, but it performed worse during operating for CEBAF from 2007 to 2009. The gun exhibited only 30 C charge

lifetime with average beam current of 60 μA throughout two years of operation due to the field emission problems.

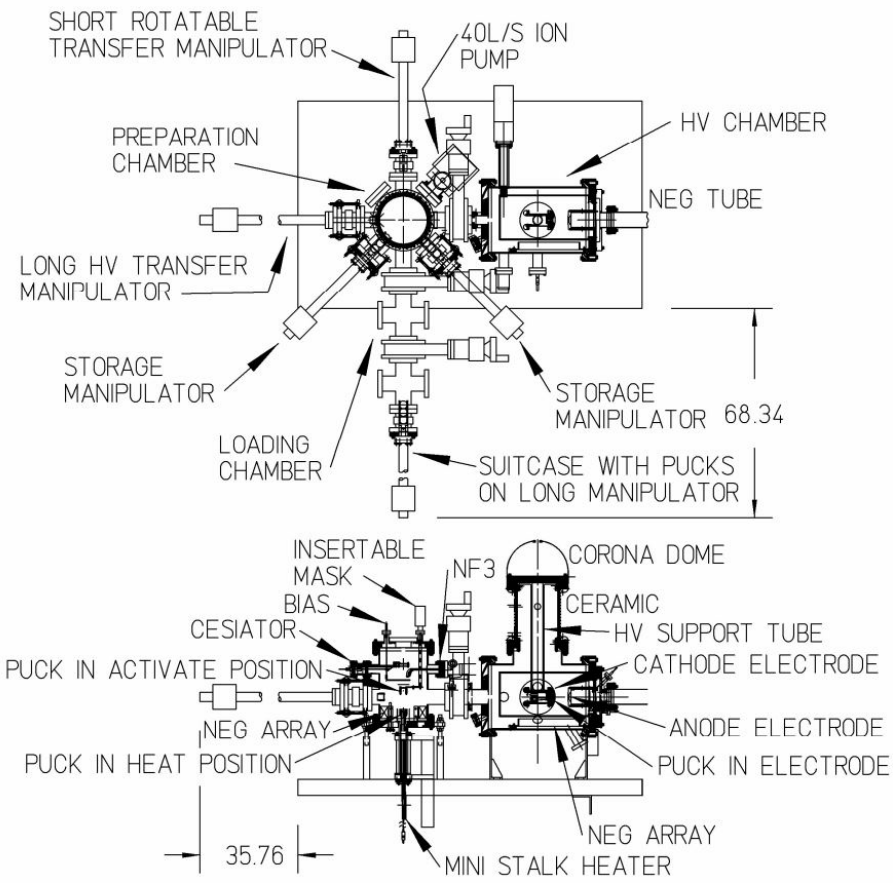

Figure 4-16: The fourth (load-locked) polarized photogun, with (top) plan view of the four vacuum chamber and manipulators and (bottom) side view of the preparation and HV chambers.

In order to overcome the influence of field emission on photogun lifetime, JLab built a load-locked DC high voltage photogun with inverted-geometry ceramic insulator for CEBAF in 2010 (i.e., the fifth polarized electron source). [158] This photogun employed a compact tapered ceramic insulator replacing the conventional large-bore cylindrical ceramic insulator as the support rod for the HV electrode, which extended into the vacuum chamber (as shown in Figure 4-17), which is commonly referred as an "inverted" gun design. [214] The design of the inverted insulator increased the distance between biased and grounded parts of the photogun, thereby reducing the electric field gradient at some locations not related to beam delivery, thus helping to eliminate the field emission. Perhaps more importantly, this design significantly reduced the number of metal parts that were biased at high voltage, so that less metal parts will generate field emission. In addition, the insulator used in this design is a common material used for medical x-ray sources, which is cheaper than the previous insulator that specially designed for electron gun applications.

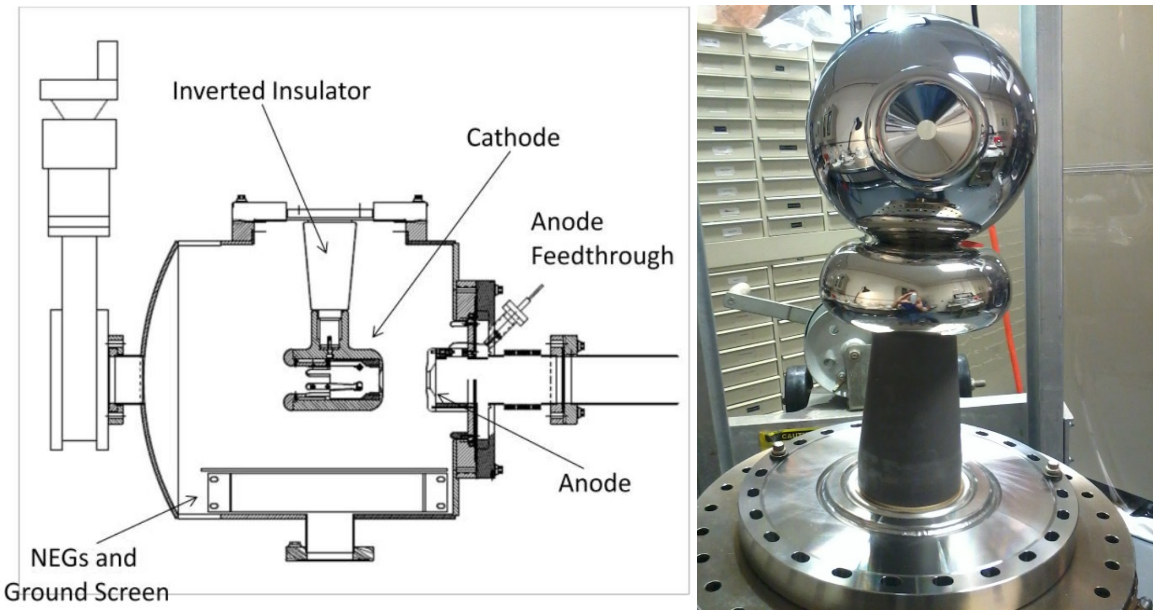

Figure 4-17: (Left) the fifth polarized photogun: load-locked photogun with compact inverted-tapered ceramic insulator; (Right) the picture of "inverted" tapered ceramic insulator and polished cathode electrode.

The fifth polarized photogun started to provide electron beam to CEBAF in 2010 and has been running ever since. The photogun provided an average beam current of ~150 μA, a charge lifetime of ~200 C, and an electron-spin polarization over 85%. Some key characteristic parameters of CEBAF polarized electron source are shown in table 4.5.

Table 4-5: Some key characteristic parameters of CEBAF polarized electron source

	First electron source	Second electron source	Third electron source	Fourth electron source	Fifth electron source
Time	1995-1998	1998 -1999	1999-2007	2007-2010	2010-present
Mounted direction	Vertical	Vertical	Horizontal	Horizontal	Horizontal
Spin manipulator	Z style	Wien filter	Wien filter	Wien filter	Wien filter
Number of short focal length elements	11	3	0	0	0
Pumping speed (H_2)	~0.5 m^3/s	~4 m^3/s	~4 m^3/s	~7.2 m^3/s	~5.6 m^3/s
Lifetime (h)	<1000	Not measured	>22,000	Not measured	Not measured
Charge lifetime (C)	<10	~100	~100	~30	~200
Charge density lifetime (C/cm^2)	~10^4	~10^5	~2×10^5	~3×10^5	~10^6
Spin polarization	~35%	70%-75%	>80%	>85%	>85%
Beam current (μA)	~30	~100	~200	~60	~150

The fifth polarized photogun was test at 100 kV, but it was found that the beam transmission was not good at 100 kV operation in CEBAF, so the biased voltage was raised up to 130 kV to obtain a better beam transmission. [87,158] In order to further improve the beam quality and reduce the effect of ion back-bombardment on the lifetime of photocathode, the photogun with a higher biased voltage was proposed and developed. At present, JLab has built a relatively mature "inverted" polarized photogun with a biased voltage of 200 kV, [87] and planned to install it on CEBAF in this summer to

replace the fifth polarized photogun. At the same time, JLab is also developing a "inverted" polarized photogun with a higher biased voltage of 350 kV. [215]

4.3.2 The preparation works for generation of high-current polarized electron beam

We planned to install the DBR photocathode described in section 4.1 to the developing 200 kV "inverted" polarized photogun (as shown in Figure 4-18) for testing, hoping to get the electron beam with high current and high spin polarization in the accelerator and get the urgent needed parameters for the new polarized accelerators. Since the QE of the DBR photocathode (>6%) is much higher than that of the existing polarized photocathode (~1%), it is expected that the DBR photocathode installed in the photogun will produce electron beam with beam current of mA-scale and obtain a good operating lifetime.

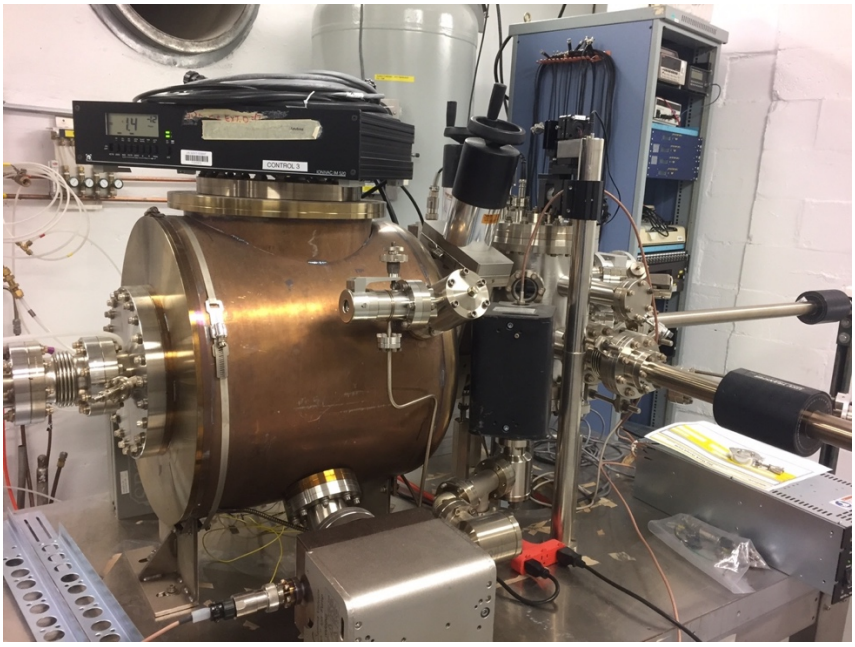

Figure 4-18: The 200 kV “inverted” polarized photogun

The 200 kV "inverted" polarized photogun was installed in Upgraded Injector Test Facility (UITF) at JLab. UITF was proposed in 2014, of which most components have been assembled and installed after three years of development (as shown in Figure 4-19). The polarized photogun can obtain ultra-high vacuum through ion pump and NEG pump. The vacuum in the photogun chamber currently pumped down to 1.4×10^{-12} torr after baking. Such low vacuum is very favorable for the photogun to obtain a long operating lifetime. There are many isolation valves between different components of the UITF and the vacuum of different components are different. For example, the vacuum in photogun chamber is $\sim 10^{-12}$ torr, while the vacuum at the end of the beamline is 10^{-11} torr. The facility was segmentally baked to obtain ultra-high vacuum. Until now, except for the superconducting radio frequency (SRF) cavity at the end of UITF, all other components have been assembled and installed. We plan to finish all preparation works for the UITF and begin to run beam in October of this year. At

that time, DBR photocathode will be installed into the photogun to generate high-energy high-current polarized electron beam and perform beam diagnosis. It is worth pointing out that we also plan to use CEBAF injector for similar high-current test experiments, adopting the same DBR photocathode and using CEBAF beam diagnostic equipment to obtain some important parameters such as spin polarization, quantum efficiency, lifetime and beam emittance. This work is currently in preparation and is expected to be completed by this year.

Figure 4-19: The Upgraded Injector Test Facility with photogun and beamline.

4.4 Summary

In this chapter, we studied two high polarization photocathodes with the purpose of obtaining higher QE and ESP. We studied how to improve the QE of photocathode by adding DBR structure into GaAs/GaAsP SSL photocathode. Simulation results showed that DBR has a high reflectivity only by reasonably setting the thickness and composition of each layer of DBR structure. The reflectivity of aAs $P_{0.35}$/AlAs$P_{0.4}$ (54 nm/64 nm×12) DBR structure used in our photocathode was up to 93.2%. By further adjusting and optimizing the thickness of the buffer layer between the DBR and SSL structures, the incident light with a specific wavelength will be resonant absorbed in the photocathode, and the photon-absorption efficiency and QE can be effectively improved. The photon-absorption efficiency of DBR photocathode studied in this paper was increased to 21%, the QE was increased to 6.4%, and the ESP was 84%. Such QE was much higher than the QE of existing high polarization photocathodes whose maximum value was 1.6%, i.e., the QE of polarization photocathode was improved several times. This result makes it possible for the photogun to generate an electron beam with a high polarization and a high beam current (greater than mA-scale).

This chapter also explored a novel SSL photocathode, GaAsSb/AlGaAs, which provided a new idea for the development of high polarization photocathode. Theoretical studies have shown that GaAsSb/AlGaAs heterogeneous structures have the highest splitting energy between light-hole and

heavy-hole bands among all the existing SSL structures based on GaAs, thus theoretically producing the electrons with highest polarization. In this chapter, we analyzed this photocathode theoretically and tested five photocathode samples with different parameters. The best results were 74.8% of polarization and 0.62% of QE. The experimental results were not ideal, and the reasons are mainly reflected in two aspects: firstly, the theoretical analysis is not accurate and secondly, the sample fabrication process is not mature. However, the results of this study provided a research basis for the subsequent development of high polarization photocathode.

Chapter 5 Conclusion

Based on a detailed review of the fundamental theory, development history and current situation of photocathode used in electron accelerators, this thesis focused on a series of research work on two types of photocathode commonly used in electron accelerators, including bulk GaAs photocathode and SSL GaAs photocathode. Our research works were completed on two vacuum chambers in Center for Injectors and Sources (CIS) at JLab, namely H1 chamber and mini-Mott chamber. H1 chamber was mainly used for the study of ion back-bombardment effect, and other studies were completed in the mini-Mott chamber. Both two chambers are capable of achieving ultra-high vacuum (~10^{-11} torr), where the photocathode is activated by depositing Cs and NF_3 on the surface of photocathode using the standard yo-yo activation technology to achieve satisfactory QE.

In this thesis, DBR structure was successfully used for the first time to enhance the QE of the high polarization photocathode, which increased the existing record value of the QE of the high polarization photocathode by several times. This result provides an important design parameters for many next-generation electron accelerators being proposed and will shorten the development process of mA-scale high polarization electron sources that are urgently needed in the world. In the thesis, the effect of hydrogen ion back-bombardment on the QE of GaAs photocathode with different surface-cleave plane was studied systematically for the first time, which provides an important reference and theory for photogun researchers to understand and further explore the ion back-bombardment effect, and to further improve the operating lifetime of photogun in the future.

The main contents and conclusions of this thesis are summarized as follows:

1. By adding DBR structure into GaAs/GaAsP SSL photocathode, the QE of photocathode was effectively improved. At the wavelength of peak polarization, the DBR photocathode obtained a QE as high as 6.4%, and the corresponding polarization was 84%. For non-DBR photocathode, the QE at the wavelength of peak polarization was 0.89%, and the corresponding polarization was 90%. Compared with the non-DBR photocathode, the QE enhancement of the DBR photocathode was 7.2. The 6.4% of QE described in this thesis is the highest record value for all high polarization photoelectrodes so far, and is much higher than the existing maximum value of 1.6%.

2. The implantation with hydrogen ions into a photocathode served to reduce the QE of the photocathode. After implantation with low-energy (100 eV) hydrogen ions, the QE degradation was modest, and the decreased QE can be recovered by heating the photocathode. However, after implantation with high-energy (10,000 eV) hydrogen ions, the QE was significantly decreased, and the decreased QE could not be fully recovered through heating. These observations suggest that the low-energy hydrogen ions only produced reversible damage (interstitial defect), so the QE degradation can

be fully recovered. The high-energy hydrogen ions not only caused reversible damage, but also caused irreversible damage (vacancy), so the QE degradation can only be partially recovered.

3. The GaAs with surface-cleave plane (110) has the most open space, the strongest ion channeling, the least irreversible damage, and the highest recovery degree of QE. Therefore, the surface-cleave plane (110) is the least sensitive to the ion bombardment and is the best choice for a photogun using bulk GaAs photocathode.

4. A novel SSL photocathode, GaAsSb/AlGaAs, was explored in this thesis. The theoretical analysis showed that the GaAsSb/AlGaAs heterogeneous structure has the largest splitting energy between the light-hole and heavy-hole bands, and thus can produce the highest spin polarization. The best results obtained by the experiments were: 74.8% of polarization and 0.62% of QE. Although the experimental results are not ideal, this study provides a strong research basis for the subsequent development of high polarization photocathode.

5. Commercially bulk GaAs can be used as a photocathode without complex chemical cleaning, and is capable of producing a electron beam with QE up to 20% illuminated by a 532 nm laser in ultra-high vacuum chambers.

6. Temperature and doping concentration are the main factors affecting the spin polarization of GaAs photocathode, which can be described by BAP and DP spin relaxation mechanisms. The spin relaxation mechanism indicates that polarization is higher when the photocathode temperature is lower and the doping concentration is lower. In our experiments, the high-doped (1×10^{19} cm^{-3}) GaAs photocathode exhibited a polarization of ~30% at room temperature, while low-doped (5×10^{17} cm^{-3}) GaAs photocathode exhibited a polarization exceeding the theoretical limit (50%) at low temperature (77 K) with the maximum polarization of ~52%. The polarization of GaAs photocathode is also affected by the activation layer on the photocathode surface. The thicker the activation layer, the lower the photocathode polarization. In addition, the cleave orientation of the crystal has no effect on the photocathode polarization.

Based on this work, a number of interesting experiments can be further performed to help to improve the performance of GaAs photocathodes. Some of these include:

- Study ion back-bombardment using activated and un-activated photocathodes, and a dedicated ion source offering better control of the applied dose, the ion energy, and the ion distribution at the sample.
- Study the temperature and dopant concentration dependence of ESP for the high polarization SSL photocathode.
- Further optimize the structure of DBR photocathode to obtain higher QE and higher ESP that is at least approaching the best value from non-DBR photocathode.

- Furtherly optimize the structure of GaAsSb/AlGaAs SSL photocathode to obtain higher ESP, whose maximum value could be higher than the recorded value of 92% in theoretical.
- Explore other new polarization photocathode materials.

It is hoped that our studies and these experiments mentioned above will improve the development of GaAs-based photocathode and other polarization photocathodes.

Bibliography

[1] Bryant, P. J. "A brief history and review of accelerators." CERN European Organization for Nuclear Research-Reports-CERN, 1-1 (1994)

[2] Lin, F., Bogacz, A., Brindza, P., Camsonne, A., Daly, E., Derbenev, Y.S., Douglas, D., Ent, R., Gaskell, D., Geng, R. and Grames, J., "Progress on the design of the polarized medium-energy electron ion collider at jlab", this proceeding, IPAC15 (2015)

[3] Ptitsyn, Vadim, "eRHIC—Future Electron-Ion Collider at BNL", AIP Conference Proceedings. Eds. Peter D. Barnes, et al. Vol. 842. No. 1. AIP, (2006)

[4] X. R. Chen, "Electron Ion Collider Plan in China", The 7th Workshop on Hadron Physics in China and Opportunities Worldwide, (2015)

[5] E. Gibney, "China plans super collider", Science 511, 394, (2014)

[6] C. Hernandez-Garcia, P.G. O'Shea, and M. L. Stutzman, "Electron sources for accelerators", Physics Today 61, 44 (2008)

[7] R. Xiang, J. Teichert, "Photocathodes for High Brightness Photo Injectors", Physics Procedia, Vol.77: 58 (2015)

[8] N. B. Clayburn, J. L. McCarter, J. M. Dreiling et al.," Search for spin-polarized photoemission from GaAs using light with orbital angular momentum", Physical. Review. B, Vol.87: 035204 (2013)

[9] C. Y. Prescott, W. B. Atwood, R. L. A. Cottrell et al., "Further measurements of parity non-conservation in inelastic electron scattering", Physics Letters B, Vol. 84: 524 (1979)

[10] A. Rosenberg, "Spin-Polarized Electron Induced Asymmetric Reactions in Chiral Molecules", Topics in Current Chemistry, Vol. 298: 279 (2011)

[11] Berger and J. Kessler, "Elastic scattering of polarised electrons from mercury and xenon, Journal of Physics B, vol. 19: 3539 (1986)

[12] W. V. Drachenfels, U. T. Koch, T. M. Muller et al., "A pulsed source for polarized electrons with high repetition rate", Nuclear Instruments and Methods, Vol.140: 47 (1977)

[13] M. J. Alguard, J. E. Clendenin, R. D. Ehrlich et al., "A source of highly polarized electrons at the stanford linear accelerator center", Nuclear Instruments and Methods, Vol.163: 29 (1979)

[14] L. A. Hodge, F. B. Dunning, and G. K. Walters, Rev. Sci. Instrum. 50, 1 (1979)

[15] D. T. Pierce, F. Meier, and P. Zürcher, "Negative electron affinity GaAs: A new source of spin-polarized electrons", Applied Physics Letters, Vol.26: 670 (1975)

[16] C. K. Sinclair, E. L. Garwin, R. H. Miller et al., "A High Intensity Polarized Electron Source for the Stanford Linear Accelerator", AIP Conference Proceedings 35, (1976)

[17] W. Hartmann, D. Conrath, W. Gasteyer et al., "A source of polarized electrons based on photoemission of GaAsP", Nuclear Instruments and Methods in Physics Research Section A, Vol.286: 1 (1990)

[18] G. D. Cates, V.W. Hughes, R. Michaels et al., "The bates polarized electron source", Nuclear Instruments and Methods in Physics Research Section A, Vol.278: 293 (1989)

[19] M. J. J. van den Putte, C.W. De Jager, S. G. Konstantinov, V.Ya. Korchagin, F. B. Kroes, E. P. van Leeuwen, B. L. Militsyn, N. H. Papadakis, S. G. Popov, G.V. Serdobintsev, et al., "The polarized electron source at NIKHEF", AIP Conference Proceedings 421, 260 (1998)

[20] M. Eberhardt, J. Wittschen, M. Gowin et al., "The 50 keV Source of Polarized Electrons at ELSA: Past and Future", Proceedings of the 17th International Spin Physics Symposium, (2007)

[21] J. M. Grames, C. K. Sinclair, J. Mitchell, E. Chudakov, H. Fenker, A. Freyberger, D. W. Higinbotham, M. Poelker, M. Steigerwald, M. Tiefenback, et al., "Unique electron polarimeter

analyzing power comparison and precision spin-based energy measurement", Phys. Rev. ST Accel. Beams 7, 042802 (2004)

[22] K. Aulenbacher et al., SLAC Report No. 432, (1993) [23]

[23] J. Grames, R. Suleiman, P. A. Adderley, J. Clark, J. Hansknecht, D. Machie, M. Poelker, and M. L. Stutzman, "Charge and fluence lifetime measurements of a dc high voltage GaAs photogun at high average current", Phys. Rev. ST Accel. Beams 14, 043501 (2011)

[24] T. Saka, T. Kato, T. Nakanishi, M. Tsubata, K. Kishino, H. Horinaka, Y. Kamiya, S. Okumi, C. Takahashi, Y. Tanimoto, et al., "New-type photocathode for polarized electron source with Distributed Bragg Reflector", Jpn. J. Appl. Phys. 32, 1837 (1993)

[25] S. Zhang, M. L. Stutzman, M. Poelker, Y. Chen, and A. Moy, in Proceedings of the IPAC2015, Richmond, USA (2015)

[26] T. Omori, Y.Kurihara, T.Nakanishi, H. Aoyagi, T. Baba, T. Furuya, K. Itoga, M. Mizuta, S. Nakamura, Y. Takeuchi, M. Tsubata, and Yoshika, "Large enhancement of polarization observed by extracted electrons from the AlGaAs-GaAs superlattice", Phys. Rev. Lett. 67, 3294 (1991)

[27] T. Omori, Y. Kurihara, Y. Takeuchi, M. Yoshioka, T. Nakanishi, S. Okumi, M. Tsubata, M. Tawada, K. Togawa, Y. Tanimoto, C. Takahashi, T. Baba, and M. Mizuta, "Highly polarized electron source using InGaAs-GaAs strained-layer superlattice", Jpn. J. Appl. Phys. 33, 5676 (1994)

[28] T. Maruyama, D. A. Luh, A. Brachmann, J. E. Clendenin, E. L. Garwin, S. Harvey, J. Jiang, R. E. Kirby, C. Y. Prescott, R. Prepost, and A. M. Moy, "Systematic study of polarized electron emission from strained GaAs/GaAsP superlattice photocathodes" Appl. Phys. Lett. 85, 2640 (2004)

[29] A. V. Subashiev, L. G. Gerchikov, Y. A. Mamaev, Y. P. Yashin, J. S. Roberts, D.-A. Luh, T. Maruyama, and J. E. Clendenin, "Strain-compensated AlInGaAs–GaAsP superlattices for highly polarized electron emission", Appl. Phys. Lett. 86, 171911 (2005)

[30] T. Nishitani, T. Nakanishi, et, al., "Highly polarized electrons from GaAs–GaAsP and InGaAs–AlGaAs strained-layer superlattice photocathodes", J. Appl. Phys. 97, 094907 (2005)

[31] Yu. A. Mamaev, L. G. Gerchikov, Yu. P. Yashin, D. A. Vasiliev, V. V. Kuzmichev, V. M. Ustinov, A. E. Zhukov, V. S. Mikhrin, and A. P. Vasiliev, "Optimized photocathode for spin-polarized electron sources", Appl. Phys, Lett. 93, 081114 (2008)

[32] W. B. Herrmannsfeldt, "Low emittance thermionic electron gun", SLAC-PUB-4843 (1989)

[33] Nishimori, Nobuyuki; Nagai, Ryoji; Hajima, Ryoichi; Shizuma, Toshiyuki; Minehara, Eisuke, "A Thermionic electron gun system for the JAERI superconducting FEL", Proceedings of 7th European Particle Accelerator Conference (EPAC 2000)

[34] K. Togawa, T. Shintake, H. Baba, T. Inagaki, K. Onoe, T. Tanaka, "Low emittance 500 kV thermionic electron gun", Proceedings of LINAC 2004

[35] H. P. Bluem, D. Dowell, A. M. M. Todd and L. M. Young, "High brightness thermionic electron gun performance", Proceedings of ERL 2011

[36] S. H. Gold, A. Ting, V. Jabotinski, B. Zhou, and P. Sprangle, "Development of a high average current rf linac thermionic injector", Phys. Rev. ST Accel. Beams 16, 083401 (2013)

[37] C. R. Crowell, "The Richardson constant for thermionic emission in Schottky barrier diodes", Solid-State electronics, 8 (4), 395 (1965)

[38] Michael Borland, "A high-brightness thermionic microwave electron gun", Ph. D. Thesis, SLAC, Stanford University, (1991)

[39] Jean-Marc Bonard, Mirko Croci, Christian Klinke, Ralph Kurt, Olivier Noury, and Nicolas Weiss, "Carbon nanotube films as electron field emitters", Carbon 40, 1715 (2002)

[40] A.V. Crewe, D. N. Eggenbbrger, J. Wall, L. M. Welter, "Electron gun using a field emission source", Rev. Sci. Instrum. 39, 576 (1968)

[41] Hitoshi Nakahara, Shunsuke Ichikawa, Tomoya Ochiai, Yoshikazu Kusano, and Yahachi Saito, "Carbon Nanotube Electron Source for Field Emission Scanning Electron Microscopy", J. Surf. Sci. Nanotech. 9, 400 (2011)

[42] R. Ganter, R.J. Bakker, M. Dehler, J. Gobrecht, C. Gough, E. Kirk, S.C. Leemann, K. Li, M. Paraliev, M. Pedrozzi, et al., "High current electron emission from microscopic tips", Proceedings of FEL 2006, THCAU04, 781

[43] R. Ganter, R.J. Bakker, R. Betemps, M. Dehler, T. Gerber, J. Gobrecht, C. Gough, M. Johnson, E. Kirk, G. Knopp, et al., "Nanoseconds field emitted current pulses from ZrC needles and field emitter arrays", J. Vac. Sci. Tech. B 24, 974(2006)

[44] Peter Hommelhoff, Yvan Sortais, Anoush Aghajani-Talesh, and Mark A. Kasevich, "Field Emission Tip as a Nanometer Source of Free Electron Femtosecond Pulses", Phys. Rev. Lett. 96, 077401 (2006)

[45] David Bernard Williams, C. Barry Carter, "Transmission Electron Microscopy: A Textbook for Materials Science. Diffraction. II", (Springer Science & Business Media, 1996) p.77

[46] W. E. Spicer and A. Herrera–Gómez, "Modern Theory and Applications of Photocathodes", SLAC–PUB 6306 (1993), presented at the 1993 SPIE International Symposium on Imaging and Instrumentation, San Diego

[47] P. Mine, "Photoemissive materials and their application to gaseous detectors", Nucl. Instr. and Meth. In Phys. Res. A 343, 99 (1994)

[48] L. Cultrera, "Advances in photocathodes for accelerators", Proceeding of IPAC 2014, MOZB02, p.48

[49] Bruce Dunham, John Barley, Adam Bartnik, Ivan Bazarov, Luca Cultrera, John Dobbins, Georg Hoffstaetter, Brent Johnson, Roger Kaplan, Siddharth Karkare, et, al., "Record high-average current from a high-brightness photoinjector", Appl. Phys. Lett. 102, 034105 (2013)

[50] H. Chaloupka, H. Heinrich, M. Jeck, A. Michalke, H. Piel, C. K. Sinclai, F. Ebeling, T. Weiland, U. Klein, and H. Vogel, "A proposed superconducting photoemission source of high brightness", Proceeding of the Fourth Workshop on RF Superconductivity, 1989

[51] L. Cultrera, S. Karkare, B. Lillard, A. Bartnik, I. Bazarov, B. Dunham, W. Schaff, and K. Smolenski, "Growth and characterization of rugged sodium potassium antimonide photocathodes for high brilliance photoinjector", Appl. Phys. Lett. 103, 103504 (2013)

[52] C. N. Berglund, W. E. Spicer, "Photoemisstion studies of copper and silver: experiment", Phys. Rev. 136, A1044, (1964)

[53] D.H. Dowell, I. Bazarov, B. Dunham, K. Harkay, C. Hernandez-Garcia, R. Legg, H. Padmore, T. Rao, J. Smedley, and W. Wan, "Cathode R&D for future light source", Nucl. Instr. and Meth. A. 622, 685 (2010)

[54] K. L. Jensen, D.W. Feldman, N. A. Moody, and P. G. O'Shea, "A photoemission model for low work function coated meatal surfaces and its experimental validation", J. Appl. Phys. 99, 124905 (2006).

[55] H. Montgomery, "Jefferson Lab: A Long Decade of Physics", J. Phys.: Conf. Ser. 299 (2011) 011001

[56] H. Raether, "Surface plasmons on smooth and rough surfaces and on gratings", (Sprinder- Verlag, New York, 1988)

[57] E. N. Economou, "Surface plasmons in thin films", Phys. Rev. 182, 539 (1969)

[58] J. Le Perchec, P. Quemerais, A. Barbara, and T. Lopez-Rıos, "Why metallic surfaces with grooves a few nanometers deep and wide may strongly absorb visible light", Phys. Rev. Lett. 100, 066408 (2008)

[59] A. Polyakov, C. Senft, K.F. Thompson, J. Feng, S. Cabrini, P. J. Schuck, H. A. Padmore, S. J. Peppernick and W. P. Hess, "Plasmon-enhanced photocathode for high brightness and high repetition rate X-ray sources", Phys. Rev. Lett. 076802 (2013)

[60] S.V. Baryshev, S. Antipov, A.D. Kanareykin, M.R. Savina, A.V. Zinovev, and E. Thimsen, "Metal plasmonic nanostructures functionalized by atomic layer deposition of mgo for photocathode applications", Proceedings of IPAC2014, MOPRI058, 739

[61] R. K. Li, H. To, G. Andonian, J. Feng, A. Polyakov, C.M. Scoby, K. Thompson, W. Wan, H. A. Padmore, and P. Musumeci, "Surface-plasmon resonance-enhanced multiphoton emission of high-brightness electron beams from a nanostructured copper cathode", Phys. Rev. Lett. 110, 074801 (2013)

[62] J. J. Uebbing and L. W. James, "Behavior of Cesium Oxide as a Low Work-Function Coating", J. Appl. Phys. 41, 4505 (1970)

[63] Weidong He, Subramanian Vilayurganapathy, Alan G. Joly, Tim C. Droubay, Scott A. Chambers, Juan R. Maldonado, and Wayne P. Hess, "Comparison of CsBr and KBr covered Cu photocathodes: Effects of laser irradiation and work function changes", Appl. Phys. Lett. 102, 071604 (2013)

[64] Lingmei Kong, Alan G. Joly, Timothy C. Droubay, Yu Gong, andWayne P. Hess, "Enhanced quantum efficiency from hybrid cesium halide/copper photocathodes", Appl. Phys. Lett. 104, 171106 (2014)

[65] Timothy C. Droubay, Scott A. Chambers, Alan G. Joly, Wayne P. Hess, Karoly Németh, Katherine C. Harkay, and Linda Spentzouris, "Metal-Insulator Photocathode Heterojunction for Directed Electron Emission", Phys. Rev. Lett. 112, 067601 (2014)

[66] L. Cultrera, I. Bazarov, J. Conway, B. Dunham, Y. Hwang, Y. Li, X. Liu, T. Moore, R. Merluzzi, K. Smolenski, S. Karkare, J. Maxson, and W. Schaff, "Photocathode R&D at Cornell University", Proceedings of IPAC2012, 2137 (2012)

[67] W. E. Spicer, "Photoemissive, photoconductive, and optical absorption studies of alkali-antimony compounds", Phys. Rev. 112, 114 (1958)

[68] Takayoshi Kimoto, Yoshihiro Arai, and Xiaobing Ren, "Lifetime test of photoemission from Cs3Sb photocathode coated with W or Cr film", Applied Surface Science 284, 657 (2013)

[69] Hyo-Soo Jeong, Kris Keller and Brad Culkin, "Electron emission properties of Cs3Sb photocathode emitters in a panel device", J. Vac. Sci. Technol. B 33, 031214 (2015)

[70] I. Martini, E. Chevallay, S. Doebert, V.N. Fedosseev, C. Hessler, M. Martyanov, "Studies of Cs3Sb cathodes for the Clic drive beam photoinjector option", Proceedings of IPAC2013, MOPFI058, 413 (2013)

[71] E. Wang, D. Kayran, M.G. McIntyre, D. Weiss, T. Rao, J. Smedley, W. Xu, I. Ben-Zvi, S. Belomestnykh, M. Ruiz-Oses, and H. Xie, "Fabrication of alkali antimonide photocathode for SRF gun", Proceedings of IPAC2014, MOPRI059, 742 (2014)

[72] C. Ghosh and B. P. Varma Optoelectronics, "Preparation and study of properties of a few alkali antimonide photocathodes", J. Appl. Phys. 49, 4549 (1978)

[73] M. Kuriki, H. Iijima, K. Miyoshi, N. Yamamoto, "A lifetime study of CsK2Sb cathode", Proceedings of IPAC2013, MOPFI013, 309 (2013)

[74] B. Erjavec, "Activation of the Na2KSb photocathode with Cs and O2 at lowered temperatures", Applied surface science 103, 343 (1996)

[75] Zikri Yusof, Eric Wisniewski, and Linda Spentzouris, "Development of cesium telluride photocathodes for awa accelerator upgrade", Proceedings of IPAC2012, TUPPD071, 1569 (2012)

[76] S. Schreiber, S. Lederer, I. Hansen, H. H. Sahling, P. Michelato, L. Monaco, and D. Sertore, "Photocathodes at FLASH", Proceedings of IPAC2012, MOPPP029, 625 (2012)

[77] R. Xiang, A. Arnold, P. Michel, P. Murcek, J. Teichert, P. Lu, and H. Vennekate, "Recent improvement of cs2te photocathodes at HZDR", Proceedings of IPAC2014, MOPRI025, 642 (2014)

[78] Xiaoqian Fu. "Optimizing GaN photocathode structure for higher quantum efficiency", Optik 123, 765-768 (2012)

[79] H. Sonnenberg. InAsP-Cs2O, "a high-efficiency infrared-photocathode", Appl. Phys. Lett. 16, 245 (1970)

[80] W. E. Spicer, "The III-V photocathode: A major detector development", Pub. Astron. Soc. Pacific, 84 (1972)

[81] Wei Liu, Shukui Zhang, Marcy Stutzman, and Matt Poelker, "The effects of ion bombardment on bulk GaAs photocathodes with different surface-cleavage planes", Phys. Rev. Accel. Beams 19, 103402 (2016)

[82] Pierce, D.T. and F. Meier, "Photoemission of spin-polarized electrons from GaAs", Phys. Rev. B 13(12), 5484-5500 (1976)

[83] T. Nakanishi, H Aoyagi, H. Horinaka, Y. Kamiya, T. Kato, S. Nakamura, T. Saka, and M. Tsubata, "Large enhancement of spin polarization observed by photoelectrons from the strained GaAs layer", Phys. Lett. A 158, 345 (1991);

[84] T. Maruyama, E. L. Garwin, R. Prepost, G. H. Zapalac, J. S. Smith, and J. D. Walker, "Observation of strain-enhanced electron-spin polarization in photoemission from InGaAs", Phys. Rev. Lett. 66, 2376 (1991)

[85] T. Maruyama, E. L. Garwin, R. Prepost, and G. H. Zapalac, "Electron-spin polarization in photoemission from strained GaAs Grown on $GaAs_{1-x}P_x$", Phys. Rev. B 46, 4261 (1992);

[86] X. Jin, B. Ozdol, M. Yamamoto, A. Mano, N. Yamamoto, and Y. Takeda, "Effect of crystal quality on performance of spin-polarized photocathode", Appl. Phys. Lett. 105, 203509 (2014)

[87] P. Adderley, J. Clark, J. Grames, J. Hansknecht, M. Poelker, M. Stutzman, R. Suleiman#, K. Surles-Law, Jefferson, J. McCarter, and M. BastaniNejad, "CEBAF 200kV inverted electron gun", Proceedings of 2011 Particle Accelerator Conference, WEODS3, 1501 (2011)

[88] Erdong Wang, Jörg Kewisch, Ilan Ben-Zvi, Andrew Burrill, Trivini Rao, Qiong Wu, Animesh Jain, Ramesh Gupta, and Doug Holmes, "Heat load of a p-doped gaas photocathode in an SRF electron gun", BNL-90778-2010-CP (2010)

[89] T. Nishitani, R. Hajima, H. Iijima, R. Nagai, M. Sawamura, N. Kikuzawa, N. Nishimori, E. Minehara, M. Tabuchi, Y. Noritake, H. Hayashitani, and Y. Takeda, "JAEA photocathode dc-gun for an ERL injector", Proceedings of FEL 2006, TUPPH007, 319 (2006)

[90] K. Aulenbacher, Ch. Nachtigall, H.G. Andresen, J. Bermuth, Th. Dombo, P. Drescher, H. Euteneuer, H. Fischer, D.v. Harrach, P. Hartmann, "The MAMI source of polarized electrons", Nucl. Instr. and Meth. in Phys. Res. A 391, 498 (1997)

[91] R. L. Bell, "Negative Electron Affinity Devices", Clarendon Press, Oxford (1973)

[92] J.S. Blakemore, "Semiconducting and other major properties of gallium arsenide", J. Appl. Phys. 53(10), R123 (1982).

[93] V.V. Bakin, et al., "Semiconductor surfaces with negative electron affinity", J. Surf. Sci. Nanotech. 5, 80 (2007).

[94] H. Lund, R. Nilsen, etc. Solar Cells, http://org.ntnu.no/solarcells/, (2008)

[95] B. V. Zeghbroeck, "Principles of semiconductor devices", http://ecee.colorado.edu/~bart/book/book/contents.htm, (2011)

[96] "Electronic archive—new semiconductor materials: Characteristics and properties", ioffe institute, http://www.ioffe.ru/SVA/NSM/

[97] J. J. Scheer and J. van Laar, "GaAs-Cs: a new type of photoemitter", Solid-State Commun. 3,189 (1965)

[98] J. van Laar and J. J. Scheer, "Photoemission of semiconductors", Philips Tech. Rev., 29, 5466 (1968)

[99] Pablo J. Saez, "Polarization and charge limit studies of strained GaAs photocathodes", Ph. D. thesis, Stanford University, SLAC-R-501 UC-414 (1997)

[100] Narong Chanlek, "Quantum efficiency lifetime studies using the photocathode preparation experimental facility developed for the ALICE accelerator", Ph.D. thesis, University of Manchester (2011)

[101] J. Zou, B. Chang, Z. Yang, "Theoretical calculation of quantum yield or exponential-doping GaAs photocathodes", Acta Phys. Sinica, Vol.56, No.5 (2007)

[102] L. W. James, G. A. Antypas, J. Edgecumbe, R. L. Moon, and R. L. Bell, "Dependence on Crystalline Face of the Band Bending in Cs2O-Activated GaAs", J. Appl. Phys. 42, 4976 (1971)

[103] J. Kessler, Polarized Electrons, Springer–Verlag, Berlin (1985)

[104] V. I. Safarov and A. N. Titkov, "Optical Spin Orientation. Application to the Study of Photoelectron Kinetics", Physica 117B & 118B, 497, (1983)

[105] H. -J. Drouhin, C. Hermann, and G. Lampel, "Photoemission from activated gallium arsenide: I. Very-high-resolution energy distribution curves", Phys. Rev. B 31, 3859 (1985)

[106] C. K. Sinclair, "Report on the May 1983 workshop at polarized electron source SLAC", proceedings of the 6th International Symposium on High Energy Spin Physics [J. Phys. Colloq. 46 C2-669] (1985)

[107] F. Ciccacci, and G. Chiaia, "Comparative study of the preparation of negative electron affinity GaAs photocathodes with O2 and with NF3", J. Vac. Sci. Technol. A 9, 2991 (1991)

[108] Z. Liu, Y. sun, S. Peterson, and P. Pianetta, "Photoemission study of Cs-NF3 activated GaAs(100) negative electron affinity photocathodes", Appl. Phys. Lett. 92, 241107 (2008)

[109] Brian S. Henderson, "Study of Negative Electron Affinity GaAs Photocathodes", Department of Physics and Astronomy, Rice University, Houston, TX (2009)

[110] M. Dixon, "Activation studies of negative electron affinity Gallium Arsenide photocathodes", Department of physics and Astronomy, Carleton College, Northfield Minnesota (2011)

[111] K. Uchida, M. Kuriki, Y. Seimiya, R. Kaku, K. Miyoshi, N. Yamamoto, "A study on robustness of NEA-GaAs photocathode", Proceedings of IPAC2014, Dresden, Germany, MOPRI032 (2014)

[112] Masao Kuriki, Yuji Seimiya, Kazuhide Uchida, and Shigeru Kashiwagi, "GaAs photocathode activation with CsTe thin film", Proceedings of IPAC2015, Richmond, VA, USA, TUPWA062 (2015)

[113] J.I. Pankov, "Optical processes in semiconductors", Academic Press, New York (1975)

[114] D. E. Aspnes, S. M. Kelso, R. A. Logan, and R. Bhat, "Optical properties of $Al_x a_{1-x}As$", J. Appl. Phys. 60, 754 (1986)

[115] M. D. Sturge, "Optical Absorption of Gallium Arsenide between 0.6 and 2.75 eV", Phys. Rev. 127, 768 (1962)

[116] Edward D. Palik, "Handbook of Optical Constants of Solids volume 1", (Academic Press, Orlando, 1985) p. 438.

[117] Udo Weigel, "Cold intense electrons beam from gallium arsenide photocathodes", Ph.D. thesis, University of Heidelberg (2003)

[118] J. Clendenin and G.A. Mullhollan, "High quantum yield, low emittance electron sources", SLAC-PUB-7760 (1998)

[119] L. S. Cardman, "Polarized electron sources for the 1990's", Nucl. Phys. A 546, 317 (1992)

[120] S. H. Pan, H. Shen, Z. Hang, F. H. Pollak, W. Zhuang, Q. Xu, A. P. Roth, R. A., Masut, C. Lacelle, and D. Morris, "Photoreflectance study of narrow-well strained-layer $In_xGa_{1-x}As/GaAs$ coupled multiple-quantum-well structures", Phys. Rev. B 38, 3375 (1988)

[121] R. J. Elliot, "Theory of the Effect of Spin-Orbit Coupling on Magnetic Resonance in Some Semiconductors", Phys. Rev. 96, 266 (1954)

[122] Y. Yafet, Solid State Physics, edited by F. Seitz and D. Turnbull (Academic, New York, 1963), Vol. 14, pp. 1-98

[123] M. I. D'yakonov and V. I. Perel, "Spin Orientation of Electrons Associated with the Interband Absorption of Light in Semiconductors", Zh. Eksp. Teor. Fiz. 60, 1954 (1971) [Sov. Phys. JETP 33, 1053 (1971)]

[124] G. L. Bir, A. G. Aronov, and G. E. Pikus, "Spin relaxation of electrons due to scattering by holes", Zh. Eksp. Teor. Fiz. 69, 1382 (1975) [Sov. Phys. JETP 42, 705 (1975)]

[125] Guy Fishman, and Georges Lampel, "Spin relaxation of photoelectrons in p-type gallium arsenide", Phys. Rev. B 16, 820 (1977)

[126] F. Meier, B. P. Zakharchenya, "Optical orientation", (North-Holland Physics, Netherlands, 1984) pp.108-129

[127] I. Zutic, J. Fabian, and S. Das Sarma, "Spintronics: Fundamentals and applications", Rev. Mod. Phys. 76, 323 (2004)

[128] N. F. Mott, "The Scattering of fast electrons by atomic nuclei", Proc. R. Soc. Lond. A 124, 425 (1929)

[129] T. J. Gay, and F. B. dunning, "Mott electron polarimetry", Rev. Sci. Instrum. 63, 1635 (1992)

[130] L. A. Hodge, T. J. Moravec, F. B. Dunning, and G. K. Walters, "Mott electron spin polarization analysis system of novel design", Rev. Sci. Instrum. 50, 5 (1979)

[131] T. J. Gay, M. A. Khakoo, J. A. Brand, J. E. Furst, W. V. Meyer, and W. M. K. P. WijayaratnaF. B. Dunning, "Extrapolation procedures in Mott electron polarimetry", Rev. Sci. Instrum. 63, 114 (1992)

[132] D. M. Campbell, C. Hermann, G. Lampel, and R. Owen, "A compact cylindrical Mott electron polarimeter operating with accelerating voltage in the range 20-100 kV", J. Phys. E. 18. 664 (1985).

[133] G. D. Fletcher, T. J. Gay, and M. S. Lubell, "New insights into Mott-scattering electron polarimetry", Phys. Rev. A 34, 911 (1986).

[134] A. Gellrich, K. Jost, and J. Kessler, "Elimination of instrumental asymmetries in electron polarization analysis", Rev. Sci. Instrum. 61, 3399 (1990)

[135] A. Gellrich and J. Kessler, "Precision measurement of the Sherman asymmetry function for electron scattering from gold", Phys. Rev. A 43, 204 (1991)

[136] H. Hopster and D. L. Abraham, "New method for accurate calibration of an electron-spin polarimeter", Rev. Sci. Instrum. 59, 49 (1988)

[137] M. Uhrig, A. Beck, J. Goeke, F. Eschen, M. Sohn, G. F. Hanne, K. Jost, and J. Kessler, "Calibration of a Mott detector using circularly polarized impact radiation from helium", Rev. Sci. Instrum. 60, 872 (1989)

[138] D. M. Oro, W. H. Butler, F.-C. Tang, G. K. Walters, and F. B. Dunning, "New method for accurate calibration of an electron-spin polarimeter", Rev. Sci. Instrum. 62, 667 (1991)

[139] C.K. Sinclair, B. M. Poelker, and J. S. Price, "Atomic hydrogen cleaning of semiconductor photocathodes", Particle Accelerator conference, 1997. Proceedings of the 1997, vol.3, page. 2864-2866

[140] T. Maruyama, D.-A. Luh, A. Brachmann, J. E. Clendenin, E. L. Garwin, S. Harvey, R. E. Kirby, C. Y. Prescott, and R. Prepost, “Atomic hydrogen cleaning of polarized GaAs photocathodes”, Appl. Phys. Lett. 82, 4184 (2003)

[141] W.E. Spicer, “Negative affinity 3-5 photocathodes: Their physics and technology”, Appl. Phys. 12, 115 (1977).

[142] W.E. Spicer and R.L. Bell, “The III-V photocathode: A major detector development”, Pub. Astron. Soc. 84 110 (1972)

[143] Erdong Wang, “High quantum efficiency photocathode for use in superconducting RF gun”, Ph. D. thesis, Peking University (2012)

[144] N Chanlek, J D Herbert, R M Jones, L B Jones, K J Middleman and B L Militsyn, “The degradation of quantum efficiency in negative electron affinity GaAs photocathodes under gas exposure”, J. Phys. D: Appl. Phys. 47, 055110 (2014)

[145] N. Chanlek, R.M. Jones, J.D. Herbert, L.B. Jones, K.J. Middleman and B. L. Militsyn, “Gallium Arsenide preparation and QE lifetime studies using the ALICE photocathode preparation facility”, IPAC2010, TUPEC018 (2010)

[146] P. Sen, D. S. Pickard, J. E. Schneider, M. A. McCord, and R. F. Pease, “Lifetime and reliability results for a negative electron affinity photocathode in a demountable vacuum system”, J. Vac. Sci. Technol. B 16, 3380 (1998)

[147] J. Zhang, B. Chang, X. Fu, Y. Du, B. Li, and J. Zou, “Influence of cesium on the stability of a GaAs photocathode”, Chin. Phys. B 20, 087902 (2011)

[148] G. A. Mulhollan and J. C. Bierman, “Enhanced chemical immunity for negative electron affinity GaAs photoemitters”, J. Vac. Sci. Technol. A 26, 1195 (2008)

[149] Y. Sun, R. E. Kirby, T. Maruyama, G. A. Mulhollan, J. C. Bierman, and P. Pianetta, “The surface activation layer of GaAs negative electron affinity photocathode activated by Cs, Li, and NF3”, Appl. Phys. Lett. 95, 174109 (2009)

[150] H. M. Al-Khateeb, B. G. Birdsey, T. C. Bowen, A. S. Green, M. E. Johnston, and T. J. Gay, “A simplified GaAs polarized electron source”, Rev. Sci. Instrum. 70, 3882 (1999)

[151] T. G. Anderson, B. G. Birdsey, S. M. Woeher, M. A. Rosenberry, and T. J. Gay, “A theoretical study of the effects of insulators on electron transport through electrostatic tube lenses”, Rev. Sci. Instrum. 72, 2923 (2001)

[152] J. McCarter, “Photocathode research for electron accelerators”, Ph. D. thesis, University of Virginia (2014)

[153] C. K. Sinclair, P. A. Adderley, B. M. Dunham, J. C. Hansknecht, P. Hartmann, M. Poelker, J. S. Price, P. M. Rutt, W. J. Schneider, and M. Steigerwald, “Development of a high average current polarized electron source with long cathode operational lifetime”, Phys. Rev. ST Accel. Beams 10, 023501 (2007)

[154] See for example, Proceedings of the 21st International Symposium on Spin Physics (SPIN 2014), Beijing, China, October 20-24, 2014, edited by Haiyan Gao and Bo-Qiang Ma, published in Int. J. Mod. Phys. Conf. Ser., Volume 40 (2016)

[155] M. Kuwahara, S. Kusunoki, Y. Nambo, K. Saitoh, X.G. Jin, T. Ujihara, H. Asano, Y. Takeda, N. Tanaka, “Coherence of a spin-polarized electron beam emitted from a semiconductor photocathode in a transmission electron microscope”, Appl. Phys. Lett., 105, 193101 (2014)

[156] B. Dunham, A. Bartnik, et al., "Record high-average current from a high-brightness photoinjector", Appl. Phys. Lett. 102, 034105 (2013)

[157] C.K. Sinclair, “A 500 kV photoemission electron gun for the CEBAF FEL”, Nucl. Instr. Meth. A., 318, 410 (1992)

[158] P. A. Adderley, J. Clark, et al., “Load-locked dc high voltage GaAs photogun with an inverted-geometry ceramic insulator”, Phys. Rev. ST Accel. Beams, 13, 010101 (2010)

[159] K. A. Elamrawi, and H. E. Elsayed-Ali, “GaAs photocathode cleaning by atomic hydrogen from a plasma source”, J. Phys. D: Appl. Phys. 32, 251-256 (1999)

[160] M. Baylac, P. Adderley, J. Brittian, J. Clark, T. Day, J. Grames, J. Hansknecht, M. Poelker, M. Stutzman, A.S. Terekhov and A.T. Wu, "The Effects of Atomic Hydrogen and Deuterium Exposure on High Polarization GaAs Photocathodes", Phys. Rev. ST Accel. Beams 8, 123501 (2005)

[161] M. T. Robinson, O. S. Oen, "The Channeling of Energetic Atoms in Crystal Lattices", Appl. Phys. Lett. **2**, 30 (1963)

[162] K. Nordlund, "Molecular dynamics simulation of ion ranges in the 1–100 keV energy range", Computational Materials Science 3, 448 (1995)

[163] M. Reiser, “Theory and Design of Charged Particle Beams”, (John Wiley & Sons, Inc., New York, 1994).

[164] A. Turnbull and G. B. Evans, “Photoemission from GaAs-Cs-O”, J. Phys. D, 155, 160 (1968)

[165] Robert W. Hamm and Marianne E. Hamm, “Industrial Accelerators and Their Applications”, (World Scientific, 2012)

[166] J. Biersack, J.P. Ziegler, and M.D. Ziegler, (1985); http://www.srim.org.

[167] S. Zollner, and D. Zarr, “Optical constants of GaAs from 0.73 to 6.60 eV for dielectric film thickness metrology in compound semiconductor manufacturing”, Compound Semiconductor, IEEE International Symposium on, 2000

[168] L. W. Aukerman, M. F. Millea, and M. McColl, “Diffusion lengths of electrons and holes in GaAs”, J. Appl. Phys. 38, 685 (1967)

[169] J. Wilms, and W. E. Spicer, “Quantum efficiency and radiative lifetime in p-type gallium arsenide”, J. APPl. Phys. 36, 2815 (1965)

[170] W. W. MacAlpine and R.O. Schildknecht, “Coaxial resonators with helical inner conductor”, Proceedings of the IRE 47, 2099 (1959)

[171] CST Studio Suite, https://www.cst.com/

[172] eRHIC Zeroth Order Design Report, edited by M. Farkhondeh (MIT-Bates) and V. Ptitsyn (BNL), https://www.bnl.gov/cad/eRhic/eRHIC_ZDR.asp

[173] R. Alley, H. Aoyagi, J. Clendenin, J. Frisch, C. Garden, E. Hoyt, R. Kirby, L. Klaisner,A.Kulikov,R.Miller et al., Nucl. Instrum. Methods, A365, 1 (1995)

[174] E. C. Aschenauer, M. D. Baker, A. Bazilevsky, K. Boyle, S. Belomestnykh, I. Ben-Zvi, S. Brooks, C. Brutus, T. Burton, S. Fazio, et al., “eRHIC design study: An electron-ion collider at BNL”, arXiv: 1409. 1633

[175] D. Abbott, P. Adderley, A. Adeyemi, P. Aguilera, M. Ali, H. Areti, M. Baylac, J. Benesch, G. Bosson, B. Cade, et al., Phys. Rev. Lett. 116,214801 (2016)

[176] A. G. Aronov, G. E. Pikus, and A. N. Titkov, Sov. Phys. JETP 57, 680 (1983)

[177] K. Zerrouati, F. Fabre, G. Bacquet, J. Bandet, J. Frandon, G. Lampel and D. Paget, Phys. Rev. B 37, 1334 (1988)

[178] J. H. Jiang and M. W. Wu, Phys. Rev. B 79, 125206 (2009)

[179] T. Maruyama, R. Prepost, E. L. Garwin, C. K. Sinclair, B. Dunham, and S. Kalem, Appl. Phys. Lett. 55, 1686 (1989)

[180] S. Adachi, “Refractive indices of III-V compounds: Key properties of InGaAsP relevant to device design”, J. Appl. Phys. 53, 5863 (1982)

[181] S. Adachi, "GaAs, AlAs, and AlxGa1-xAs: Material parameters for use in research and device applications", J. Appl. Phys. 58, R1 (1985)

[182] A. D. Rakic, and M. L. Majewski, "Modeling the optical dielectric function of GaAs and AlAs: Extension of Adachi's model", J. Appl. Phys. 80, 5909 (1996)

[183] S. Ozaki and S. Adachi, "Spectroscopic ellipsometry and thermoreflectance of GaAs", J. Appl. Phys. 78, 3380 (1995)

[184] Aleksandra B. Djurišić, Aleksandar D. Rakić, Paul C. K. Kwok, E. Herbert Li, Marian L. Majewski, and Jovan M. Elazar, "Modeling the optical constants of AlxGa1-xAs alloys", J. Appl. Phys. 86, 445 (1999)

[185] M. Sotoodeh, A. H. Khalid, and A. A. Rezazadeh, "Empirical low-field mobility model for III–V compounds applicable in device simulation codes", J. Appl. Phys. 87, 2890 (2000)

[186] M. Woods, J. Clendenin, J. Frisch, A. Kulikov, P. Saez, D. Schultz, J. Turner, K. Witte, and M. Zolotorev, J. Appl. Phys. 73, 8531 (1993)

[187] M. Erbudak and B. Reihl, Appl. Phys. Lett. 33, 584 (1978)

[188] P. Hartmann, "Aufbau einer gepulsten Quelle polarisierter Elektronen", Dissertation, Shaker Verlag, Aachen, 1998

[189] Bandwidth Semiconductor, LLC, 25 Sagamore Park Drive, Hudson, NH 03051, http://www.bandwidthsemi.com

[190] G. D. Cates, V. W. Hughes, R. Michaels, H. R. Schaefer, T. J. Gay, M. S. Lubell, R. Wilson, G.W. Dodson, K. A. Dow, S. B. Kowalski, et *al.*, "The Bates polarized electron source", *Nucl. Instrum. Meth. A* 278, pp. 293-317, (1989)

[191] E. Tsentalovich, D. Barkhuff, J. Chen, G. Dodson, M. Farkhondeh, W. Franklin, E. Ihloff, F. Kaertner, C. Tschalaer, B. Yang, T. Zwart, "Development of a polarized electron source for the MIT-Bates Linear Accelerator Center", *Nucl. Instrum. Meth. A* 582, 413 (2007)

[192] M. J. J. van den Putte, C. W. De Jager, S. G. Konstantinov, V. Ya. Korchagin, F. B.Kroes, E. P. vanLeeuwen, B. L. Militsyn, N. H. Papadakis, S. G. Popov, G. V. Serdobintsev, *et al.*, "The polarized electron source at NIKHEF", in AIP Conf. Proc. 421, 260 (1997)

[193] W. Hillert, M. Govin, and B. Neff, "The 50 keV inverted source of polarized electrons at ELSA", in AIP Conf. Proc. 570, 961 (2000)

[194] X. Jin, A. Mano, F. Ichihashi, N. Yamamoto, and Y. Takeda, "High-Performance Spin-Polarized Photocathodes Using a GaAs/GaAsP Strain-Compensated Superlattice", Appl. Phys. Express 6, 015801 (2013)

[195] S. Zhang, S. V. Benson, and C. H-Garcia, "Observation and measurement of temperature rise and distribution on GaAs photo-cathode wafer with a 532 nm drive laser and a thermal imaging camera", Nucl. Instrum. Meth. A. 631, 22 (2011)

[196] M. Levinshtein, S. Rumyantsev, M. Shur, "Handbook series on semiconductor parameters", (World Scientific, 1996)

[197] J. C. Grobli, D. Oberli, and F. Meier, "Polarization resonances of optically spin-oriented photoelectrons emitted from strained semiconductor photocathodes", Phys. Rev. Lett. 74, 2106 (1995)

[198] L. G. Gerchikov, K. Aulenbacher, J. E. Clendenin, V. V. Kuz'michev, Y. A. Mamaev, T. Maruyama, V. S. Mikhrin, J. S. Roberts, V. M. Ustinov, D. A. Vasilev, A. P. Vasiliev, Y. P. Yashin, and A. E. Zhukov, "Highly Effective Polarized Electron Sources Based on Strained Semiconductor Superlattice with Distributed Bragg Reflector", AIP Conf. Proc. 980, 124 (2008)

[199] S. Adachi, "Properties of semiconductor alloys: group-IV, III-V and II-VI Semiconductors", (Wiley, 2009) P.238

[200] I. Vurgaftman, J. R. Meyer, and L. R. Ram-Mohan, “Band parameters for III-V compound semiconductors and their alloys”, J. Appl. Phys. 89, 5815 (2001)

[201] H. A. Macleod, “Thin-film optical filters”, 4th edition, (CRC Press,2010)

[202] P. Peumans, A. Yakimov, and S. R. Forrest, “Small molecular weight organic thin-film photodetectors and solar cells”, J. Appl. Phys. 93, 3693 (2003)

[203] B.W. Liang and C.W. Tu, “A kinetic model for As and P incorporation behaviors in GaAsP grown by gas-source molecular beam epitaxy”, J. Appl. Phys. 74, 255 (1993)

[204] Stephanie Tomasulo, John Simon, Paul J. Simmonds, Jonathan Biagiotti, and Minjoo L. Lee, “Molecular beam epitaxy of metamorphic $In_yGa_{1-y}P$ solar cells on mixed anion $GaAs_xP_{1-x}$/GaAs graded buffers”, J. Vac. Sci. Technol. B 29, 03C118 (2011)

[205] G. E. Pikus and G. L. Bir, Fiz. Tverd. Tela 1, 154 (1959) [Sov. Phys. Solid State 1, 136 (1959)]

[206] Shun Lien Chuang, “Efficient band-structure calculations of strained quantum wells”, Phys. Rev. B 43, 9649 (1991)

[207] Lucio Claudio Andreani, Alfredo Pasquarello, and Franco Bassani, “Hole subbands in strained GaAs-$Ga_{1-x}Al_xAs$ quantum wells: Exact solution of the effective-mass equation”, Phys. Rev. B 36, 5887 (1987)

[208] C. W. Leemann, D. R. Douglas, and G. A. Krafft, “The Continous Electron Beam Accelerator Facility: CEBAF at the Jefferson Laboratory”, Annu. Nucl. Part. Sci. 51, 413 (2001)

[209] K. A. Aniol, D. S. Armstrong, M. Baylac, E.Burtin, J. Calarco, G. D. Cates, C. Cavata, J. -P. Chen, E. Chudakov, D.Dale, et. al., “Measurement of the neutral weak form factors of the proton”, Phys. Rev. Lett. 82, 1096 (1999)

[210] C. Benvenuti, P. Chiggiato, F. Cicoira, and Y, L’Aminot, “Nonevaporable getter films for ultrahigh vacuum applications”, J. Vac. Sci. Technol. A 16, 148 (1998)

[211] M. Poelker, P. Adderley, J. Brittian, J. Clark, J. Grames, J. Hansknecht, J. McCarter, M. L. Stutzman, R. Suleiman, and K. Surles-Law, “Status of high polarization DC high voltage GaAs photoelectron gun”, in Proceeding of PAC 07, Albuquerque, New Mexico, USA, 2007 (IEEE PAC, 3756-3760 (2007))

[212] J. Grames, M. Poelker, P. Adderley, J. Brittian, J. Clark, J. Hansknecht, D. Machi, M. L. Stutuzman, and K. Surles-Law, “Measurement of photocathode operational lifetime at beam currents up to 10 mA using an improved high voltage GaAs photogun”, AIP Conference Proceeding. Eds. Kenichi. Imai. And Tetsuya Murakami. 915,1 (2007)

[213] J. Grames, P. Adderley, J. Brittian, J. Clark, J. Hansknecht, D. Machi, M. Poelker, M. L. Stutuzman, R. Suleiman, and K. Surles-Law, “Lifetime measurement of high polarization strained superlattice GaAs at current >1 mA using a new 100 kV load lock photogun”, in Proceeding of PAC07, Albuquerque, New Mexico, USA, 2007 (IEEE PAC, 3130-3132 (2007))

[214] M. Beridenbach, M. Foss, J. Hodgson, A. Kulikov, A. Odian, G. Putallaz, H. Rogers, R. Schindler, K. Skarpaas, and M. Zolotorev, “An Inverted-geometry high voltage polarized electron gun with UHV load lock”, Nucl. Instr. And Meth. In Phys. Res. A 350, 1 (1994)

[215] C. Hernandez-Garcia, M. Poelker, and J. Hansknecht, “High Voltage Studies of Inverted-geometry Ceramic Insulators for a 350 kV DC Polarized Electron Gun”, IEEE Transactions on Dielectrics and Electrical Insulation 23, 418 (2016)